Characterization of Cr_2O_3 catalysts for Cl/F exchange reactions

Dissertation

zur Erlangung des akademischen Grades
doctor rerum naturalium
(Dr. rer. nat.)
im Fach Chemie
eingereicht an der

Mathematisch-Naturwissenschaftlichen Fakultät I
der Humboldt-Universität zu Berlin
von

MSc Chemical Engineer Ercan Ünveren
geboren am 24. Oktober 1973 in Saarbrücken

Präsident der Humboldt-Universität zu Berlin
Prof. Dr. Jürgen Mlynek

Dekan der Mathematisch-Naturwissenschaftlichen Fakultät I
Prof. Dr. Michael W. Linscheid

Gutachter:

1. Prof. Dr. Erhard Kemnitz

2. Dr. Wolfgang E. S. Unger

3. Prof. Dr. Klaus Rademann

Tag der mündlichen Prüfung: 23. April 2004

Abstract

The Cr_2O_3 is one of the most important catalysts in the chlorine/fluorine (Cl/F) exchange reactions for the production of chlorofluorocarbon (CFC) alternatives. It is established as an excellent heterogeneous catalyst for fluorination reactions.

The dismutation of CCl_2F_2 was used to probe the effect of halogenation of chromia on Cl/F exchange reactions in order to find out the difference between the inactive and active catalysts. The heterogeneous reactions were performed in a continuous flow Ni reactor and also under simulated reaction conditions in a reactor where after the reaction the X-ray photoelectron spectroscopy (XPS) and the X-ray excited Auger electron spectroscopy (XAES) analyses could be followed directly without air contact, under so called “in-situ” conditions.

In order to be able to apply the Cr(III) 2p XPS analysis in the proper manner the spectroscopic features of the chromium(III) compounds of O, F and Cl were re-investigated. Latest generation of XPS spectrometers, which are able to analyze non-conductive powders with ultimate energy resolution, were used to reveal multiplet splitting features and satellite emission in the Cr 2p spectra. The energy positions of the multiplets were determined by total electron yield (TEY)- X-ray absorption near edge structure (XANES) spectroscopy. Using both high resolution XPS and XANES spectra a peak-fit analysis, which is also applicable for normally resolved Cr 2p XPS spectrum, was proposed. In order to overcome the known background problem by drawing the background in the broad Cr 2p window including the high binding energy satellite, a modified Shirley background, which is a combination of a linear and Shirley function, was used. Moreover, the spectroscopic features of the Cr(III) 3s XPS spectrum, which is relatively simpler than the Cr 2p one, were also surveyed. An alternative chemical analysis was proposed by using chemical state plots for Cr 3s.

Both ex- and in-situ ESCA show that as soon as Cr_2O_3 is conducted to CCl_2F_2 at 390 $^\circ C$ fluorination as well as chlorination takes place at the catalyst surface. When the XPS surface composition reaches approximately 4 atom% fluorination and 6 atom% chlorination, maximum catalytic activity is obtained. Applying longer reaction times do not change significantly the obtained surface composition of the activated chromia. The fluorination and chlorination of chromia was further investigated by various HF and HCl treatments as well.

The activated chromia samples and reference samples with well known chemical structure were also characterized by XANES, time of flight - static secondary ion mass spectroscopy (ToF-SSIMS), scanning electron microscopy (SEM), fluorine solid state NMR, pyridine-FTIR, wet chemical (F and Cl) analysis, X-ray powder diffraction (XRD) and surface area (BET) analysis.

The results for the references Cr_2O_3, $Cr(OH)_3$, CrF_2OH, $CrF_3.H_2O$, $\alpha - CrF_3$, $\beta - CrF_3$ and $CrCl_3$ and activated Cr_2O_3 samples were compared. The applied characterization methods suggest that the formation of chromium oxide chloride fluoride species, e.g. chromium oxide halides, at the surface is sufficient to provide catalytic activity. The presence of any CrF_3 and/or $CrCl_3$ phases on the activated chromia samples were not detected.

Contents

List of Figures

List of Tables

1 Introduction

1.1 Background

At the beginning of 1970s the photolysis of fully halogenated chlorofluorocarbons (CFCs) in the stratosphere and their role in ozone depletion started to be of great global concern. Lovelock [3] showed that the very stable CFCs were accumulating in the atmosphere by using electron capture techniques capable of detecting parts per trillion. Molina and Rowland [4], [5] introduced the relationship between ozone depletion and CFCs. They proposed that Cl atoms catalyze the decomposition of stratospheric O_3 by the mechanism

$$
\begin{gathered}
CCl_2F_2 + UV \rightarrow Cl + CClF_2 \\
Cl + O_3 \rightarrow ClO + O_2 \\
ClO + O \rightarrow Cl + O_2
\end{gathered}
$$

The net reaction is $O_3 + O \rightarrow 2O_2$. Depletion of ozone is undesirable, since it would increase the ultraviolet radiation reaching us, thereby increasing the incidence of skin cancer and cataracts, reducing crop yields, and altering the climate [6]. The general agreement was that emissions of CFCs to the atmosphere have to be minimized. Therefore, the Montreal Protocol, an international United Nations agreement, was signed in September, 1987 calling for developing science and a 50 % cut in the amount of CFCs produced by the year 1998. However, due to new findings which were announced by the National Aeronautics and Space Administrations (NASA) Ozone Trends Panel the Protocol was further strengthened in June 1990. First it was called for a total phase out by developed countries by the year 2000, and then a 1992 international treaty provided for nearly all of chlorofluorocarbon production to be phased out by the year 1996. However, the long life of chlorofluorocarbons in the atmosphere means that major stratospheric ozone depletion will continue for the next 50 to 75 years.

Because of their inertness, chemical stability, and low toxicity they were used in a wide variety of applications. The largest use of these compounds was in the area of refrigeration as working fluids in refrigerators and air conditioners. A close second was in the area of foaming agents as blowing agents for producing insulating foams. Another application area was of cleaning agents used as solvents for cleaning and de-greasing of metals and cleaning of sophisticated medical instrumentation and electronic components.

As a consequence of the Montreal and the consecutive Protocols the CFC manufacturers were straightforward to devise economically viable synthesis of molecules that would have the desirable properties of CFCs without the ozone depletion potential.

These characteristics include short atmospheric life times, low toxicity, ozone compatibility, low global warming potential, thermal and chemical stability, equivalent physical properties, and amenability to realistic processes. A short atmospheric lifetime ensures that the molecule is degraded in the troposphere, leaving little chance for entry into the stratosphere. One kind of such compounds are hydrochlorofluorocarbons. The presence of hydrogen in the molecule allows for abstraction of this hydrogen by hydroxyl radicals and further degradation in the troposphere. To eliminate the possibility of even small quantities entering the stratosphere and starting a chlorine atom initiated ozone destruction cycle, the ideal replacement would be hydrofluorocarbons containing no chlorine. It was recognized also that the market for the CFC alternatives would be significantly smaller than for CFCs. Since the application areas of foaming agents and cleaning agents would be fulfilled in completely different ways. Therefore, attention has been focused on refrigerants, the market leader being 1,1,1,2-tetrafluoroethane, CH_2FCF_3 (HFC-134a) which is an alternative to the widely used dichlorodifluoromethane, CCl_2F_2 (CFC-12).

Until the requirement to replace CFCs with the alternatives, large scale commercial synthesis had concentrated mostly on fully halogenated derivatives. Although there was a considerable body of published literature on the synthesis of fully halogenated molecules, information on catalytic processes of hydrogen containing substitutes was significantly scant. The basic step in several of these syntheses is the exchange of chlorine for fluorine, producing an equimolar amount of HCl. This exchange is quite slow in the absence of a catalyst. In 1891, Swartz [7] showed that liquid phase contact of chlorocarbon with SbF_3 produced a fluorinated compound.

$$SbF_3 + CCl_3- \rightarrow SbCl_3 + CF_3-$$

In this case he found that an activated trichloromethyl group was converted to the trifluoromethyl group. The SbF_3, which was partially converted to the trichloride or mixed chlorofluorides, was converted back to SbF_3 in a separate step by treatment with anhydrous hydrogen fluoride.

In 1928, Midgley and Henne [8] reacted CCl_4 with pentavalent antimony chlorofluoride to produce CCl_2F_2 and they showed that CFCs are the right class of compounds to be used as refrigerants instead of SO_2 and NH_3, which are flammable and are opposed to be used for that purpose.

$$SbCl_5 + 3HF \rightarrow SbCl_3F_3 + 3HCl$$
$$SbCl_2F_3 + 2CCl_4 \rightarrow SbCl_5 + CCl_3F + CCl_2F_2$$

In addition to the liquid phase processes, vapor phase halogen exchange processes were also developed. Because of usually higher operating temperatures in these heterogeneous reactions, compounds having a greater degree of fluorination were synthesized.

The need for substitution of hydrogen in the molecule has led to the development of a wide variety of catalysts and processes that are selective in this respect. Starting materials for such processes have included hydrocarbons, halohydrocarbons, olefins and haloolefins. The general processes are HF addition to olefins, halogen exchange, isomerization, disproportionation (dismutation), chlorofluorination, elimination, hydrohalogenation, dehydrohalogenation and hydrogenolysis [9].

1.2 Catalytic Synthesis of CFC Alternatives

1.2.1 Synthesis of 1,1,1,2-tetrafluoroethane, CH_2FCF_3 (HFC-134a)

There are many possible routes to CH_2FCF_3, more complicated than the synthesis of double carbon CFCs. Three of the most attractive routes are (i) hydrofluorination of $CCl_2 = CHCl$ followed by a series of F for Cl replacement steps; (ii) after chlorination of $CCl_2 = CCl_2$, a series of F for Cl and isomerization steps leading to CF_3CCl_2F followed by its hydrogenolysis; and (iii) hydrofluorination of $CCl_2 = CCl_2$, a series of F for Cl replacement steps leading to $CHClFCF_3$ followed by its hydrogenolysis. The reactions are considered below in detail.

from trichloroethylene, $CCl_2 = CHCl$ (TCE) A one step reaction of trichloroethylene with hydrogen fluoride to HFC-134a is not possible due to limitations to the thermodynamic equilibrium in the last step that is the conversion of HCFC-133a with HF to HFC-134a. Hence, the overall process is divided into two steps. The first step is the addition of HF to the double bond followed by two successive halogen exchanges to afford HCFC-133a.

$$\begin{gathered} CCl_2 = CHCl + HF \rightarrow CH_2ClCCl_2F \\ CH_2ClCCl_2F + HF \rightarrow CH_2ClCClF_2 \\ CH_2ClCClF_2 + HF \rightarrow CH_3CF_3 \end{gathered}$$

Both homogeneous and heterogeneous processes are known for this chemistry. The applicability of several catalysts, some of which are SbX_5, BF_3, TaF_5, NbF_5, and $MoCl_5$, has been reported for homogeneous reactions. A major limitation of using antimony pentahalide catalysis for this synthesis is the inherent instability of the pentahalide. Chrome based systems have conventionally employed in heterogeneous reactions for the synthesis of HFCF-133a. Chromium oxide and trivalent chrome salts supported on active carbon or alumina have been applied for the heterogeneous catalytic reaction. These catalysts are usually pre-treated with anhydrous HF at elevated temperatures prior to introduction of the organic feed.

The second step, which is the conversion of HCFC-133a to HFC-134a, is difficult due to equilibrium considerations [10]. Brunet et al. [11] investigated the activity which depends on the conditions of catalyst pre-treatment and that there is a relationship between the catalytic activity and the number of reversibly oxidized sites on the solid surface. The adsorption of HCFC-133a on to the catalyst surface as a precursor for breaking the C-Cl bonds is an essential requirement for its fluorination to obtain HFC-134a. In order to shift the thermodynamic equilibrium in the desired direction, higher temperatures and a large excess of HF are required [12]. High equilibrium conversions and selectivity to the desired HFC-134a were reported by applying chromium oxide as a catalyst operating at 350-400 $°C$ [13].

$$CH_3CF_3 + HF \rightarrow CH_2FCF_3 + HCl$$

Chrome based systems deactivate rather rapidly, especially at higher operating temperatures because of coke formation which is caused by the loss of HF from either the starting material or product giving olefins. However, Manzer [14] reported improved catalysts based on aluminium fluoride or fluorinated alumina, which have a longer catalyst life.

from tetrachloroethylene, $CCl_2 = CCl_2$ **(PCE)**

$$CCl_2 = CCl_2 + Cl_2 \rightarrow CCl_3CCl_3$$
$$CCl_3CCl_3 + 3HF \rightarrow CCl_2FCClF_2 + 3HCl$$
$$CCl_2FCClF_2 + HF \rightarrow CClF_2CClF_2 + HCl$$
$$CCl_2FCClF_2 \rightarrow CCl_3CF_3$$
$$CClF_2CClF_2 \rightarrow CF_3CCl_2F$$

Another route to HFC-134a is through the chlorination of PCE to hexachloroethane, which then undergoes successive halogen exchange reactions to afford fully halogenated species containing three or four fluorines. Both antimony-based homogeneous reactions and chrome-based heterogeneous processes lead to products CFC-113 and CFC-114. Then with isomerization of these molecules CFC-113a and CFC-114a are obtained. Further reaction of CFC-113a with HF produces CFC-114a. A useful expedient is the isomerization of CFC-114 to CFC-114a, since CFC-114 can be produced in one step, starting from PCE. A catalyst that will produce CFC-114a directly is very desirable because extra processing steps can be avoided. Aluminium fluoride is such an effective catalyst [15].

Replacement of the chlorines in CFC-114a through catalytic hydrogenolysis produces HFC-134a.

$$CF_3CCl_2F + 2H_2 \rightarrow CH_2FCF_3 + 2HCl$$

Palladium supported on carbon was used as a catalyst. In the case of CFC-114 hydrogenolysis affords HFC-134 as a major product [16]. The applicability of palladium supported on charcoal or alumina for the hydrogenolysis of CFC-114a to HFC-134a was also reported [17]. Another possibility is the conversion of CFC-113 to HFC-134a in two step process. The formation of a highly reactive olefin in the first step of the process requires stable catalysts that are not deactivated by polymerization on the surface. The preservation of the double bond for the second step of the process is also necessary. Since usual hydrogenolysis catalysts might saturate the double bond. For the purpose of the second step various heterogeneous catalysts were reported. One of them is the chromium based catalyst. Halasz [18] investigated the effect of oxide-fluorides of chromium in the addition reaction of HF to trifluoroethylene at mild temperatures.

$$CCl_2FCClF_2 + \frac{3}{2}H_2 \rightarrow CF_2 = CHF + 3HCl$$
$$CF_2 = CHF + HF \rightarrow CH_2FCF_3$$

Similar to the hydrogenolysis of CFC-114a, the hydrogenolysis of CFC-114 affords CHF_2CHF_2 (HFC-134). The isomerization of HCF-134 to HCF-134a proceeds over aluminium fluoride [19], over chrome based or supported systems [20], as well as chlorofluorides of alumina [21]. Kemnitz et al. [22] studied this isomerization reaction in the presence of a chromia catalyst conditioned exclusively with chlorine free fluorocarbons in order to avoid all the possible side reactions. In the presence of chlorofluorocarbons HCl as well as HF would be formed and strongly adsorbed on to the surface. In contrast to HF, HCl gives rise to a very complex system of side reactions. As a raw material for isomerization, HFC-134 can also be made by the hydrogenation of tetrafluoroethylene. Palladium on carbon is quite effective for this hydrogenation [23].

1.2.2 Synthesis of 1,1,1-trifluoro-2,2-dichloroethane, $CHCl_2CF_3$ (HCFC-123)

Much like HFC-134a, several catalytic routes to HCFC-123 have been investigated.

from tetrachloroethylene, $CCl_2 = CCl_2$ (PCE)

$$CCl_2 = CCl_2 + HF \rightarrow CHCl_2CCl_2F$$
$$CHCl_2CCl_2F + HF \rightarrow CHCl_2CClF_2 + HCl$$
$$CHCl_2CClF_2 + HF \rightarrow CHCl_2CF_3 + HCl$$

Synthesis of HCFC-123 involves the initial addition of HF to PCE, followed by two halogen exchange reactions. Manzer showed that highly fluorinated alumina containing added metal salts are an efficient catalyst system for the heterogeneous process [24]. During the reaction some HCFC-123 tends to react further to give more fluorinated products, such as HCFC-124 and HCFC-125. In contrast to fluorinated aluminas, chromium (III) oxide as well as chrome supported on alumina and other many useful catalyst systems were reported for this chemistry [25][26][27].

from chlorination of CH_3CF_3 (HCFC-133a) From TCE obtained HCFC-133a can be converted to HCFC-123 by chlorination. This is a substitution reaction of Cl for H. It is necessary to operate this process at relatively low conversion in order to prevent the formation of CFC-113a by overchlorination.

$$CH_3CF_3 + HCl \rightarrow CHCl_2CF_3 + H_2$$
$$CHCl_2CF_3 + HCl \rightarrow CCl_3CF_3 + H_2$$

from CCl_3CF_3 (CFC-113a) Like the hydrogenolysis of CFC-114a, the treatment of CFC-113a with hydrogen in the presence of suitable catalysts should produce HCFC-123. A selective catalyst is required. A very active catalyst might overhydrogenolysis CFC-113a to HCFC-133a or further to CH_3CF_3 (HFC-143a).

1.2.3 Synthesis of 1,1,1,2-tetrafluorochloroethane, $CHClFCF_3$ (HCFC-124)

The synthesis of HCFC-124 is not much different than the synthesis of HCFC-123. Fluorination of HCFC-123 leads to HCFC-124. Moreover, pentahaloethane $C_2HCl_xF_{(5-x)}$ or fluorinated olefin such as chlorotrifluorethylene $CClF = CF_2$ can be used instead of PCE as a starting material. Again, chrome based systems are quite effective for this HF addition. Overfluorination results in HFC-125. Selective hydrogenolysis of CFC-114a was also reported. Generally the hydrogenolysis of CFC-114a produces HFC-134a as a major product and HCFC-124 as a by-product, but selective catalytic systems were developed that replace just a single chlorine, resulting in HCFC-124 as the major product.

1.2.4 Synthesis of pentafluoroethane, CHF_2CF_3 (HCFC-125)

The previous discussed methods and catalytic systems are also applicable for the synthesis of HFC-125. If one starts with PCE, after the initial HF addition the end point will be HFC-125. Active catalysts seem to contain chrome in some form. Pre-treatment of such catalysts were reported to modify the activity. HFC-125 can also be synthesized from the hydrogenolysis of CF_3CClF_2 CFC-115.

1.2.5 Synthesis of 1,1-difluoroethane, CH_3FCHF_2 (HFC-152a)

from acetylene, $CH = CH$ 1,1-Difluoroethane can directly be synthesized by the addition of HF to acetylene. Several catalytic processes are available

$$HC \equiv CH + 2HF \rightarrow CH_3FCHF_2$$

for the synthesis of this molecule. A highly selective route to HFC-152a involves the homogeneous catalysis reaction by BF_3 [28]. AlF_3, which has been used as a catalyst in halogen exchange reactions, also function as an efficient HF addition catalyst. The product can be shifted to vinyl fluoride by operating at a higher temperature [29].

from vinyl chloride, $CH_2 = CHCl$ Since vinyl chloride is relatively cheaper than acetylene, it is preferred in the synthesis of HFC-152a. In the liquid phase

$$CH_2 = CHCl + 3HF \rightarrow CH_3FCHF_2 + HCl$$

processes $SnCl_4$ is reported as a very good selective catalyst [30]. In vapor phase processes fluorinated alumina or aluminium fluoride has been widely used. The conventional chromium based systems have also been used with success.

from dichloroethanes Both symmetrical and unsymmetrical dichloroethanes have been used as starting materials for HFC-152a. Catalyst employed include salts of antimony, such as $SbCl_5$ or SbF_5 [31]. Also chromium oxide produces HFC-152a from 1,2-dichloroethane [32].

1.2.6 Synthesis of 1,1-dichloro-1-fluoroethane, CH_3CCl_2F (HCFC-141b)

Two ways were proposed for the synthesis of HCFC-141b. In the first route HF reacts with vinylidene chloride in the presence of a catalyst. Aluminium fluoride was reported as a suitable catalyst for this process.

1.2.7 Synthesis of difluoromethane, CH_2F_2 (HFC-32)

Difluoromethane received some attention as a low boiling point refrigerant. It can be directly synthesized from dichloromethane CH_2Cl_2 by halogen exchange. In 1937, Henne [33] reported that the reaction of SbF_3 with CH_2Cl_2 afforded HFC-32. This is a stoichiometric reaction necessitating reconversion of the antimony halide. In heterogeneous reactions the use of aluminium fluoride or mixtures of chromium fluoride and aluminium fluoride was suggested.

1.3 Fundamentals of heterogeneous fluorination catalysts

The non-oxidative substitution of chlorine by activated fluorine (as F^-) is an important process in the production of CFCs and their alternatives. In these reactions, a C-Cl bond is replaced by a C-F bond using an appropriate fluorinating agent such as HF. In the different kind of chlorine/fluorine exchange reactions metal(III) oxides, especially chromia and alumina, are frequently used as heterogeneous catalysts. These reactions are (i) fluorination reactions of halocarbons with gaseous HF, (ii) dismutation reactions, especially mono-carbon CFCs and HCFCs and (iii) isomerization reactions, especially of di-carbon halocarbons. As a consequence of the Montreal and the consecutive Protocols replacing CFCs by their alternatives increased the interest for fundamental research on the action of heterogeneous fluorination catalysts and on the mechanism of halogen exchange reactions at the catalyst surface.

1.3.1 Chromium and aluminium oxides

Chromia is an excellent heterogeneous catalyst for fluorination reactions. It presents enhanced catalytic activity and improved selectivity in comparison with alumina. Chromia belongs to the group of n-type semi-conducting ceramics occurring with the structure of the corundum type (cf. Fig. 1) in which the cations occupy distorted octahedral sites coordinated by six O ligands. The (0001) surfaces have been extensively investigated [34]. The results obtained from ion scattering spectroscopic measurements [35] and the LEED-I/V analysis [35], [36] show only the half of the expected Cr atoms present on the surface due to reconstruction and they are almost completely imbedded in the oxygen layer. However, under ordinary conditions, uncalcined, newly prepared chromia contains large quantities of water and hydroxyl groups which saturate the metal sites that remain at the surface. Consequently, activation of chromia involves a dehydration of the surface, resulting in coordinatively unsaturated Cr(III) which can act as active sites. These hydroxyl groups play a key role in the necessary activation step of chromia to be used as a fluorination catalyst. A metal oxide catalyst requires activation for a certain time either in HF and/or a CFC/HFC gas stream until it becomes catalytically active [37]. Thus, chromia catalysts used for halogen exchange require an activation procedure in order to achieve final activity [22]. Although chemical analysis indicates significant uptake of halogen by the solid, X-ray diffraction commonly does not provide any evidence for changing of the bulk composition [22], [38], [39], [40], [41].

Coulson et al. [42] studied the dismutation of $CHClF_2$ over chromium(III) oxide based catalysts. They found that Cr_2O_3 in the presence of $CHClF_2$ undergoes two separate surface transformations before becoming catalytically active toward dismutation. The first transformation involves a reductive deoxygenation of high-valent surface Cr species resulting in the formation of CO_2 and other oxidized products. This reduced surface then reacts with $CHClF_2$ to form CO and a halogenated, catalytically active surface. It is concluded that the catalysis occurs on coordinative unsaturated Cr^{3+} active sites which are halogenated. Kemnitz et al. [22] studied also the dismutation of $CHClF_2$ CHF_2Cl and CCl_2F_2 over Cr_2O_3. Under isothermal conditions the catalyst precursor requires a certain time of activation during its interaction with the HCFC or CFC gas phase. Within only a few minutes, fundamental changes in the properties of the solid surface occur and it becomes catalytically active, resulting in a rapid establishment of the dismutation equilibrium. The increase of the catalytic activity is accompanied by a rapidly increasing liberation of HCl followed by a decrease in HCl concentration in the effluent. The process of HCl evolution is complete at nearly the same time as the catalyst reaches its full activity. Other gaseous fluoroalkanes exhibit similar behaviour, however the time required obtaining full catalytic activity and the extent of HCl evolution depend on the fluoroalkane used. Although there is no indication for the formation of any chromium halides from XRD measurements, chemical analysis indicates the uptake of fluorine and chlorine by the solid, some few percent of fluoride and up to 0.4 % chloride. Evidently halogenation of chromia, at least at the surface, is required for it to be catalytically active for fluorine/ chlorine exchange reactions. Reaction between surface OH groups and a fluoroalkane molecule leads to destruction of the latter and the formation of hydrogen halides and CO_2 or CO. This was demonstrated for the heterogeneously catalyzed hydrolysis reaction of CFCs on γ -alumina and chromia surfaces [43]. As long as OH groups or adsorbed water molecules are present to act as Brønsted sites on the surface, a heterogeneous reaction between gaseous CFCs/HFCs and these Brønsted acid centers occurs, resulting in destruction of the halocarbon followed by fluorination of the solid surface.

Mechanistically different but resulting in a similar change of the surface, is the behaviour of di-carbon hydrohalocarbons. A halogen exchange is possible both on the basis of olefins and alkanes [12], [44], [45], [46]. The parallel occurrence of dehydrohalogenation and hydrohalogenation (elimination and addition) reactions lead to the same products. Dehydrohalogenation is repressed in the presence of HF, so that the chlorine-fluorine exchange becomes predominant. Therefore, dehydrofluorination is an important reaction when a hydrofluorocarbon is allowed to react in the presence of an unfluorinated chromia.

Since X-ray diffraction analysis is not helpful in detecting solid phases or species formed at the surface which may be catalytically active, other techniques were used to obtain information relating to the active surface sites of fluorinated chromia. Although using the tracer ^{18}F it is possible to differentiate among three different surface fluoride species [47], these studies do not enable the nature of the solid phases formed during the activation process to be determined with certainty. Therefore, XPS studies have been performed in several studies [22], [42], [48] in order to follow the changes of the oxide surface arising from fluorination. Up to 10 % surface fluoride was detected employing gaseous HF and about 8 %, using CHF_3 as the fluorinating agent. Surprisingly, the Cr $2p_{3/2}$ binding energy did not exhibit any significant changes as a result of surface fluorination. However, from the value for the F 1s binding energy, ca 684.2 eV, strong evidence for the formation of fluorinated chromia species, was obtained [42]. Later, more extensive XPS measurements on chromia, fluorinated chromia, and chromium fluoride phases clearly demonstrated that these values are not characteristic of completely fluorinated chromia samples but are indicative of partly fluorinated chromia surfaces [22]. It is still uncertain whether there are domains of pure chromium fluoride at the surface of treated samples or larger areas of chromium oxide-fluoride or oxide-halide species [49].

1.3.2 Chromium and aluminium fluorides

Catalytically active sites for Cl/F exchange reactions are Lewis acidic in nature. Considering that fluorine is more electronegative than oxygen and is able to form a similar variety of different structures in its compounds which are often in the similar way chemically inert and thermally stable. One should expect even higher Lewis acidity in metal fluorides than in the respective metal oxides. Relatively less attention has been paid to the catalytic potential of metal fluorides in heterogeneously catalyzed reactions. Several studies have demonstrated that there is strong evidence that aluminium oxide-fluoride phases are catalytically active in halogen exchange reactions and that further fluorination results in the formation of aluminium fluoride phases which are highly active catalysts. The situation for chromium is rather different.

Both metals form a series of MF_3 modifications which are isotypic to each other. In general, in these MF_3 compounds, the coordination number of the cation is 6, and the structural arrangement can be described in terms of a three dimensional array of corner-sharing octahedra.

Only the rhombohedral $\alpha - MF_3$ modification is thermodynamically stable, and occurs with the VF_3-type-structure [50] (cf. 2). The anionic arrangement can be described as a compact stacking perpendicular to the ternary axis. The cations are located at the corners and at the center of the rhombohedron. All the other MF_3 phases are meta-stable. The $\beta - MF_3$ phases adapt a hexagonal tungsten bronze structure (HTB) (cf. 2) having nano-porous openings defined by corner sharing rings of six [MF_6] octahedra which run along the c axis. New modifications of aluminium fluoride, designated as η-, θ- and κ- AlF_3, have been synthesized and structurally characterized [51], [52], [53], [54], [55]. Their structures are very similar to the HTB structure. Furthermore, both aluminium and chromium, form isotypic hydroxide-fluorides, $MF_x(OH)_{3-x}$ (0.4 ≤ x ≤ 2.07) [56] occurring in the pyrochlore structure (cf. 2). This is more open than the HTB-structure because slightly distorted hexagonal channels are located along all six plane diagonals of the cubic cell [57].

Many investigations have shown that $Al(F,OH)_3$, $\alpha - AlF_3$ and $\beta - AlF_3$ are formed as a result of the reaction of alumina with fluoroalkanes. Consequently, these fluoride phases have been synthesized and their catalytic behaviour and surface properties investigated. Among pyrochlore $Al(F,OH)_3$, $\alpha - AlF_3$ and $\beta - AlF_3$ only the latter one exhibits immediate catalytic activity in mono-carbon haloalkane dismutations. As γ -alumina, also $Al(F,OH)_3$ requires an activation before it becomes catalytically active whereas pure $\alpha - AlF_3$ does not exhibit any catalytic activity, neither after a prolonged treatment with fluorocarbons nor at higher temperatures up to 873 K. Even employing a larger amount of $\alpha - AlF_3$, to obtain the same absolute surface area, did not result in a significantly enhanced catalytic activity. Only after introducing crystal disorder, e.g. by partial hydrolysis, a slight activity was observed [58].

The catalytic behaviour of the solid fluoride phases is consistent with their behaviour in Temperature Programmed Desorption (TPD) and pyridine FTIR photoacoustic measurements. Calcined $\beta - AlF_3$ already exhibits full catalytic activity without any activation. Characteristic for this phase is the appearance of two distinct regions of high concentrations of acid sites at the surface, one in the temperature region around 423 K representing weak acidity and one around 623 K representing strong acid surface sites. In contrast, $\alpha - AlF_3$ does not exhibit any potential for pyridine adsorption, thus showing that there are no acid sites at its surface.

All metastable AlF_3 phases have nano-porous openings defined by corner-shared rings of six [AlF_6] octahedra. Whereas the $\beta - AlF_3$ phase has these channels aligned along the c-direction of the crystal, forming straight channels, the $\eta - AlF_3$ phase has adjacent rings tilted with respect to each other, producing an undulating channel along the ab-plane. The structure of the new tetragonal phase, $\theta - AlF_3$ [51] contains different rings formed from 5, 4, and 3 [AlF_6] octahcdra. The 5-rings form an undulating 3-D interconnected channel system around tetrahedral clusters of four [AlF_6] octahedra. The microporous nature of this new phase is similar to that of the $\beta - AlF_3$ and $\eta - AlF_3$ phases. The new $\kappa - AlF_3$ phase, prepared by thermal decomposition of $\beta - NH_4AlF_4$ [52], [53] has channels running through the crystal comprising 5, 4, and 3 rings of corner shared [AlF_6] octahedra. The catalytic activation studies of these new phases in the fluorination of $CHCl_3$ and CCl_3CF_3 [54] shows that open network structures of AlF_3 exhibit catalytic activity. Since the catalytic process occurs at the surface of these solids and taking into account the catalytic inactivity of the compact $\alpha - AlF_3$ phase, it can be concluded that the particular surface structure arising from the bulk [$\mathrm{AlF_6}$] octahedra arrangement and the availability of the active centers, but not the size of the surface area, are of crucial importance for the catalytic process.

Due to the structural similarities of aluminium and chromium fluorides, one should expect similarities in their surface properties and catalytic behaviour. Thus, the well characterized pure chromium fluoride phases have been investigated in a similar way as described above for the aluminium systems [22], [58]. From these results, $Cr(F,OH)_3$, $\alpha - CrF_3$ and $\beta - CrF_3$ follow approximately the behaviour described already for the aluminium system. However, there are several differences which have to be considered in more detail. In contrast to $\alpha - AlF_3$, which is synthesized by sublimation as a perfect crystal, the isotypic pure $\alpha - CrF_3$ exhibits non-negligible catalytic activity most probably due to crystal disorder. The thermodynamic situation for the competitive formation of metal fluorides and metal chlorides is fundamentally different for the aluminium and chromium systems. The small value of ΔG for the formation of CrF_3 is probably the reason why chromia becomes only partly fluorinated, whereas alumina in contact with gaseous fluoroalkanes forms a compact aluminium fluoride layer under the same conditions. Stable chromium(III) oxide-fluorides could be formed under the conditions discussed here but they are not well characterized at the present time.

1.3.3 Structural differences between $\alpha - MF_3$ and $\beta - MF_3$ related phases

The feature that AlF_3, and the framework open structures of the other AlF_3 phases have in common is that aluminium is octahedrally co-ordinated by six fluoride anions. However, the kind of linkage of these [$\mathrm{AlF_6}$] octahedra differs fundamentally. In rhombohedral $\alpha - AlF_3$ the cations are located at the corners and at the center of the rhombohedron [57]. Figure 2 shows the [$\mathrm{AlF_6}$] octahedra network in this structure. In contrast, $\beta - AlF_3$ adopts the hexagonal tungsten bronze (HTB) structure [59] which is presented also in Figure 2, where the [$\mathrm{AlF_6}$] octahedra form hexagonal channels along the c-axis. Owing to this open structure, the density of $\beta - AlF_3$ is significantly lower than that of $\alpha - AlF_3$. In $\beta - AlF_3$ the channel diameter is only about 2.46 Å, which is too small for incorporating haloalkane molecules. Moreover, only fluoride anions form the inner surface of these channels which cannot therefore act as Lewis acid sites. The same is true for η-, θ- and κ- AlF_3 phases. On this basis, a simple model has been proposed combining the experimental data of the observed acidity and the catalytic activity of both phases [22]. According to this model, the activity differences between $\alpha - AlF_3$ and $\beta - AlF_3$ related phases arise from differences of the surface structures arising from differences in their bulk structures. Thus, the surface derived from $\alpha - AlF_3$ is covered completely with large basic fluoride

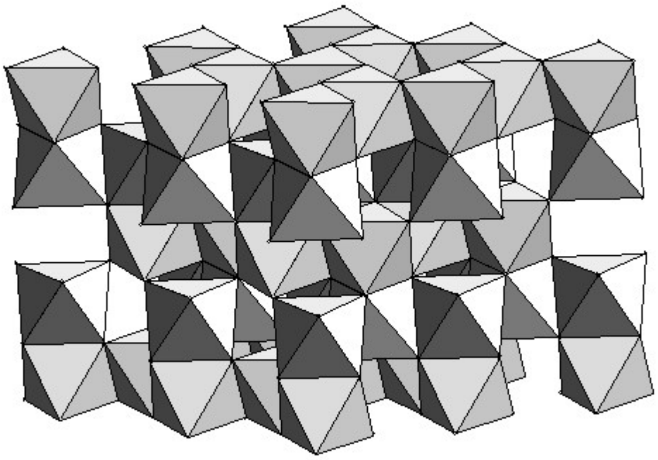

Figure 1: Structure of Cr_2O_3, corundum

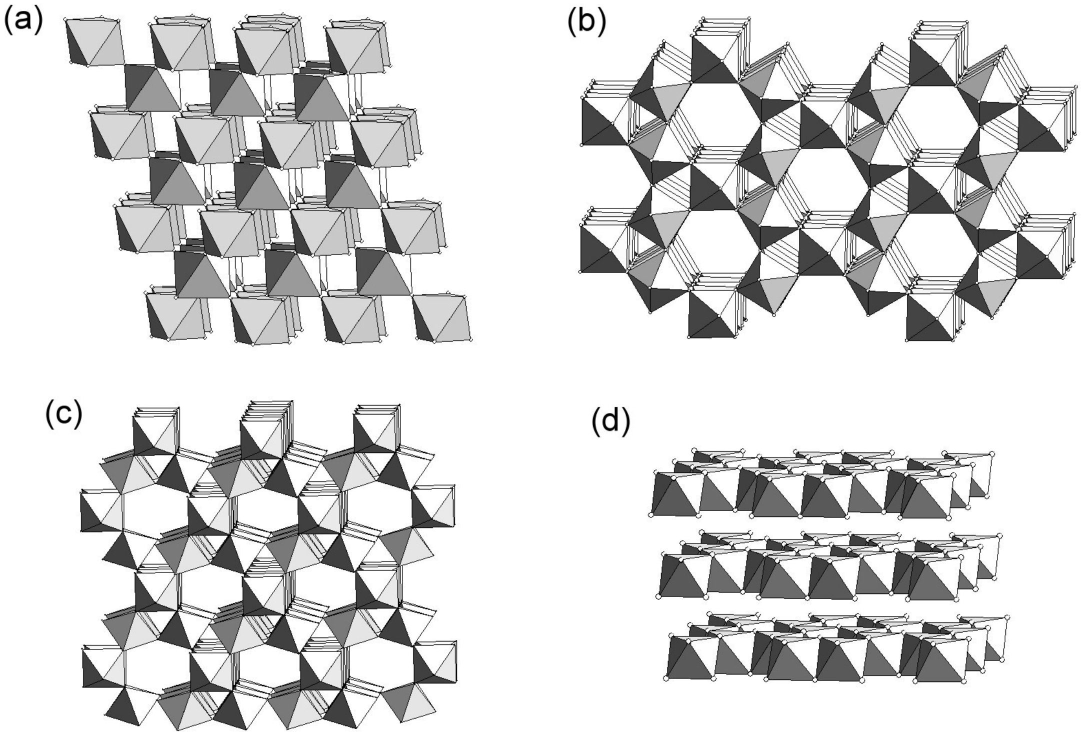

Figure 2: Structure of (a) $\alpha - CrF_3$, (b) $\beta - CrF_3$, (c) CrF_2OH (pyrochlore) and (d) $CrCl_3$

anions, irrespective of its indices. In contrast, cleavage of the HTB-structure related AlF_3 phases along the directions of channels results in a buckled surface structure with exposed metal atoms which are coordinatively unsaturated and are sterically accessible by fluoroalkanes thus explaining the observed Lewis acidity and catalytic activity of $\beta - AlF_3$ related phases.

At first sight, the catalytic behaviour and the surface properties of pyrochlore $Al(F,OH)_3$ does not fit this model since the pyrochlore structure is a more open one than the HTB- AlF_3 structure. However, since aluminium hydroxide-fluoride is susceptible to thermal decomposition, it is in fact no longer pyrochlore $Al(F,OH)_3$ under the temperature conditions employed for the catalytic reactions. Thus, the behaviour of this phase in heterogeneous catalytic halogen exchange can be explained by the presence of amorphous alumina which determines the surface characteristics at the initial stage. Consequently, this phase acts in a manner similar to alumina and not until the surface becomes completely fluorinated does it reach its full catalytic activity [49].

The structure of $CrCl_3$ is also shown in Figure 2. $CrCl_3$ is known as catalytically in active.

The aim of this work: Although chromium(III) oxide is one of the most important catalysts in the CFC alternatives production, the catalyst surface has not been completely investigated during these reactions. Most of the reaction types in the synthesis of CFC alternatives are basically Cl/F exchange reactions. In order to study the chromia catalyst surface in detail, as a probe reaction the catalytic dismutation of CCl_2F_2, which is also a Cl/F exchange reaction, is chosen. The main interest is which kind of modifications take place on the catalyst surface during conditioning and formation processes. Are there separate phases or species formed like on Al_2O_3 catalyst samples activated by dismutation reactions of CCl_2F_2 or are there rather oxide-fluorides or oxide-halides to be expected? This will be investigated by samples which are activated in a continuous flow Ni reactor and also under simulated reaction conditions in a reactor after where the XPS analysis can be done without air contact, providing so called “in-situ” conditions. In addition, powder XRD, wet chemical (F and Cl) analysis, surface area (BET) analysis, pyridine-FTIR spectra, XANES, SEM, ToF-SIMS and NMR will be applied for further catalyst characterization in order to determine the bulk and mainly the surface properties of the samples.

Another task of this work is to find a way to handle the complex features of the Cr 2p X-ray photoelectron spectrum in order to be able to make a correct interpretation for chemical analysis. Once this is achieved, an analysis procedure should be developed and this method will be used by the interpretation in ESCA.

Finally, it is the aim of this work to provide a better understanding on the basis of deeper inside in the conviction of the catalytically active fluorinated chromia phase or species as a result of activation of chromia by gaseous fluorine containing reactants.

2 Basics of the Methods

2.1 X-ray Photoelectron Spectroscopy (XPS)

2.1.1 Principle of Technique

X-ray photoelectron spectroscopy (XPS) was developed in the mid-1960s by Siegbahn and his research group at the University of Uppsala, Sweden. The technique was first known by the acronym ESCA, Electron Spectroscopy for Chemical Analysis. The advent of commercial manufacturing of surface analysis equipment in the early 1970s enabled the placement of equipment in laboratories throughout the world. In 1981, Siegbahn was awarded the Nobel Prize for Physics for his work on XPS.

Surface analysis by XPS involves irradiating a solid in vacuo with soft X-rays and analyzing the emitted electrons by their kinetic energy. The spectrum is obtained as a plot of the number of the detected electrons per energy interval versus their kinetic energy. Each element, except H, has a unique spectrum. The spectrum of a physical mixture of elements is approximately the sum of the peaks of the individual constituents. Since the mean free path of electrons in solids is very small (cf. Fig. 3), the detected electrons originate from only the top few atomic layers, making XPS a unique surface sensitive technique for chemical analysis. Quantitative data can be obtained from peak areas, and identification of chemical states often can be made from exact measurement of peak positions on the binding energy scale, as well as from certain spectral features.

As an X-ray source Mg K α (1253.6 eV) or Al K α (1486.6 eV) photons are usually used. These photons have limited penetrating power in a solid in the order of 1-10 micrometers. They interact with atoms, causing electrons to be emitted by the photoelectric effect. The emitted electrons have kinetic energies measured in the XPS experiment given by:

$$KE = h\nu - BE - \phi_s \tag{1}$$

where $h\nu$ is the energy of the photon, BE is the binding energy of the atomic orbital from which the electron originates, and ϕ_s is the spectrometer work function [60].

The binding energy may be regarded as the energy difference between the initial state before photoionization and the final state after the photoelectron has left the atom. There is a different probability or ionization cross-section for each final state. The Fermi level (E_F) by definition corresponds to zero binding energy. However, in the case of an insulator the occupied valence band is separated from the empty conduction band, whilst in the case of a metal these bands overlap and the uppermost occupied state at 0 K is termed the E_F. It should be noted that E_F is not the true zero point of the electron energy scale, although BEs are often referenced to this point. The true zero is the vacuum level (E_v) and, to a first approximation, $E_F - E_v = \phi$, where ϕ is the work function of the material.

Because the core levels of each element have unique binding energies, XPS can be used to identify and determine the concentration of the elements in the surface. Variations in the elemental binding energies, in other words the chemical shifts, arise from differences in the chemical potential (V, Madelung potential) and polarizability of compounds. These chemical shifts can be used to identify the chemical state of the elements in materials being analyzed.

There are two relaxation processes, the Auger decay and the fluorescent decay which follow the photoionization. In addition to photoelectrons emitted in the photoelectric process, Auger electrons are emitted because of nonradiative relaxation of the core hole remaining after photoemission. This Auger electron emission occurs roughly 10^{-14} seconds after the photoelectric event [61]. The competing emission of a fluorescent X-ray photon depends on the atomic number. For K shell ionization, the probability of relaxation by Auger emission is favoured overwhelmingly over that of X-ray fluorescence for core levels with binding energies below about 2 keV. In the Auger process, an outer electron falls into the inner orbital vacancy, and another electron is simultaneously emitted, carrying off the excess energy. The kinetic energy of the Auger electron equals to the difference between the energy of the initial ion and the doubly charged final ion, and is independent of the mode of initial ionization. Thus, photoionization normally leads to two kinds of emitted electrons which are photoelectrons and Auger electrons. The sum of the kinetic energies of the electrons emitted cannot exceed the energy of the ionizing photons [61].

Probabilities of electron interaction with matter further exceed those of the photons. Therefore, the path length of the photons is of the order of micrometers, while the inelastic mean free path of the electrons is of the order of tens of angstroms. Thus, while ionization occurs to depth of a few micrometers, only those electrons that originate within tens of angstroms below the solid surface can leave the surface. These electrons which leave the surface without energy loss produce the peaks in the spectra and are the most useful ones. On the other hand, the electrons which leave the surface with energy loss construct the background in the spectra.

Photoelectron peaks As s levels have no spin-orbit splitting, the p, d and f levels have spin-orbit splitting of which the intensity ratios are 1:2 for p levels, 2:3 for d levels and 3:4 for f levels.

The most intense photoelectron peaks are typically the narrowest peaks observed in the spectra. Peak width is a convolution of (i) the natural line width which is determined by the lifetime of the hole resulting from the photoionization process,

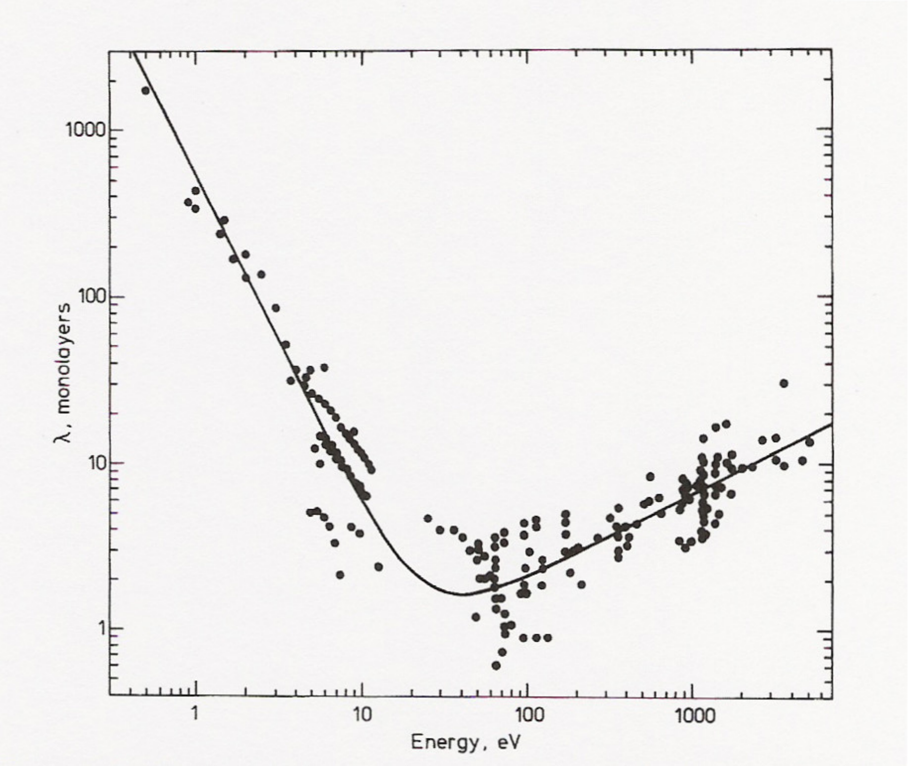

Figure 3: The dependence of inelastic mean free path on electron energy [1]

(ii) the width of the exciting X-ray line and (iii) the instrumental contribution to the observed line width.
Moreover, solid state effects cause line broadening as well. Spectral peak broadening may also be observed for insulating materials due to static charging effects which is a problem commonly experienced in the interpretation of an XPS spectrum. Static charging arises as a consequence of the build up of a positive charge at the surface of nonconductive specimens when the atoms loose electrons in the photoemission process. This positive charge produces a retarding field in front of the specimen such that the photoelectrons have a kinetic energy lower than that predicted by the Equation 1.

Auger peaks These are groups of peaks in rather complex patterns. Since Auger peaks have kinetic energies which are independent of the energy of the ionizing radiation, they appear on a binding energy plot to be in different positions when ionizing photons of different energies are used. Core type Auger transitions with final vacancies deeper than the valance levels usually have one intense line similar to the most intense photoelectron line.

2.1.2 Chemical Shift

One of the most valuable properties of core level photoelectron spectroscopy is the "chemical shift". The chemical shift implies that the detailed core level binding energy for an atom of a certain element depends on the first coordination sphere of the probed atom. Therefore, chemical shifts can be used to extract important and basic information about the system under study. It is the basis of many of the powerful applications of core level electron spectroscopy.

It has long been recognized that the XPS of solids do not directly measure local ground state charge environments, because relaxations or secondary excitations are always associated with core hole production, it is generally difficult to determine the precise correspondence between XPS and ground state properties.

The core level binding energy is defined as the total energy difference between the ionized (N-1 electron) final state system and the initial (N electron) system. In this way chemical shift of binding energy (ΔBE) between two systems A and B can be expressed as

$$\begin{aligned}\Delta BE &= [E_{f,A}(N-1) - E_{i,A}(N)] - [E_{f,B}(N-1) - E_{i,B}(N)] \\ &= [E_{f,A}(N-1) - E_{f,B}(N-1)] - [E_{i,A}(N) - E_{i,B}(N)] \qquad (2)\end{aligned}$$

The shift is thus determined by two total energy differences, one relating to the initial states (i) and one relating to the final states (f) [62].

Often chemical shifts are treated in a different way which leads to a completely different meaning of the terms initial and final state effects. This is related to the often used separation of the core level binding energy into a set of contributions which correspond to different levels of approximation. The ionization energy is then given by a sum of terms.

$$\Delta BE = \Delta E_H + \Delta E_{relax} + \Delta E_{corr} \qquad (3)$$

where the first term is the Koopman's level shift which is referred to as the initial state shifts. The second term is defined as the final state shifts. The correlation energy contribution is usually small but should not be neglected.

The first term is the orbital energy or the frozen orbital ionization energy. This would be the ionization energy according to Koopman's theorem if all other electrons were unaffected by the ionization. The next term, the relaxation energy, is due to the relaxation or screening by the other electrons in the system as the core electron is removed. There is first of all an atomic contribution to the relaxation energy due to the contraction of the atomic orbitals. In a molecular or solid system there is in addition a flow of charge towards the core hole site called extra atomic relaxation. In fact, in extended systems the ionization often leads to a final state in which the core hole site is more or less completely neutralized by a valence electron. In molecular systems, this level of approximation is usually implemented by performing independent self consistent field (SCF) calculations according to Hartree-Fock for the initial and final states. The third energy term in this decomposition is the correlation energy contribution. The correlation energy may give both a positive or a negative contribution to the ionization energy. Hence, the chemical shifts can be expressed as the sum of the corresponding three terms.

From another point of view, the simple electrostatic considerations according to Gauss' theorem lead to the conclusion that the energy required to remove a core electron from an atom should increase with increasing positive net atomic charge and decrease with increasing negative net atomic charge. However, the potential energy of a core electron is not only affected by the valence charge q but is also affected by the charges of all the other atoms in the compound. This contribution is related to the Madelung potential or the electrostatic self potential V. Moreover, in the final state of the photoemission process an atom is left with a core hole and this positive charge will polarize the surrounding atoms and the valence electrons. There will be an electronic relaxation energy that will lower the binding energy values. This relaxation energy can be divided into two parts: an atomic contribution and an extra atomic contribution. The atomic contribution, R^a, depends on the atomic number and the core orbital involved in the photoemission process. It is due to the contraction of the outer electronic charges toward the core hole. The extra-atomic contribution, R^{ea}, is the relaxation energy associated with the rest of the system that is with the flow of electron density from the surroundings toward the core ionized atom [63]. According to the point charge potential approximation

$$BE = BE_{atom} + V + kq - R^{ea} + qR^a \tag{4}$$

where BE_{atom} is the binding energy of the core electron in the free atom. $V = \Sigma_j(q_j/R_j)$ is the Madelung potential, q_j are the charges of all the other atoms and R_j are their distances from the core ionized atom. k is the change in core potential resulting from a removal of a valence electron. R^{ea} is the extra atomic relaxation energy and qR^a is the atomic relaxation energy lost ($q > 0$) or gained ($0 < q$) by the ion in the compound with respect to the free atom. Therefore, the chemical shift according to the Gauss' theorem can be expressed as

$$\Delta BE = \Delta V + \Delta kq - \Delta R^{ea} + \Delta qR^a. \tag{5}$$

2.1.3 Intra and Extra Atomic Relaxations

The electron system in the remaining atomic shells relax as the photoelectron leaves, providing stabilization energy for the ion. This stabilization energy is called atomic relaxation or rearrangement energy.

In the presence of a core hole, unfilled orbitals associated with the ion are pulled down to higher binding energy levels relative to the eigenlevels of the atom in its ground state environment. One of these pulled down levels could become populated to locally charge compensate the core hole. This compensation process represents a partial deexcitation of the system and the kinetic energy of the outgoing electron will correspondingly decrease in the apparent binding energy of the XPS line. Thus, if both the unrelaxed hole and the screened hole could be observed, then the screened condition would appear in XPS at the low binding energy side, with the unrelaxed hole at the higher binding energy. This is intra atomic relaxation or local screening, when there is no involving of electrons from neighbouring atoms. The intra atomic relaxation energy is appropriate to an isolated atom. On the other hand, in a molecule or in a solid, where additional screening electrons are available from the environment of the ionized atom then the deexcitation energy is called extra atomic relaxation energy or nonlocal screening energy or polarization energy.

These unfilled orbitals are pulled down to higher binding energy levels in the presence of a core hole. Like in a transition metal insulator the unfilled 3d levels and extended 4s-p orbitals overlap the ligand 2p orbitals. Both the cation 4s-p's and the ligand 2p's are substantially extended spatially so that these levels strongly overlap, both in energy and in space. This strong orbital overlap provides favourable conditions for the partial population of the cation s-p screening orbitals from the distributed ligand 2p's in response to the sudden creation of a photohole resulting a polarization condition. Although partial charge compensation might be accomplished by this nonlocal s-p occupancy, the fully relaxed ion is realized with occupation of a local screening orbital that is predominately 3d in character. Electrons in the nonlocal screening orbitals may reside in those states for times well in excess of 10^{-16} seconds which is a typical photoemission lifetime as determined by observed XPS line widths [2]. Thus, both final state conditions are likely to be sufficiently metastable so that both will produce sharp features in the XPS spectrum. The low binding energy main line correlates to the relaxed hole whereas the satellite at the high binding energy side correlates to the unrelaxed hole. These satellites are generally called shake-up peaks. This is a result of extra atomic relaxation in transition metal insulators.

2.1.4 Auger Parameter

Photoelectron lines and X-ray excited Auger lines often exhibit differences in chemical shifts which are a function of the chemical environment of the atom. Since the chemical shifts of photoelectrons and Auger electrons are different, the difference between their kinetic energies constitutes a special spectral property, and its numerical property is unique for each chemical state. In its simplest term, the Auger

parameter is the kinetic energy of an Auger electron minus the kinetic energy of a photoelectron [64]. The Auger parameter concept was based on the following ideas:
(1) There is a constant difference between the kinetic energies of a photoelectron and an Auger electron.
(2) Charge corrections to the individual peak measurements are unnecessary because they simply cancel during the estimation of the Auger parameter.
(3) Work function corrections are also unnecessary, and vacuum level data can be compared to Fermi level data directly.
For a transition from an isolated atom to a chemical state, the shift in kinetic energy of the photoelectron is

$$\Delta KE_{PE} = -\Delta\varepsilon_e + R_e^{ea}(K^+) \tag{6}$$

and the kinetic energy shift of the Auger electron is

$$\Delta KE_{Auger} = -\Delta\varepsilon_e + 3R_e^{ea}(K^+) \tag{7}$$

where $\Delta\varepsilon_e$ is the energy change in initial states, R_e^{ae} is the extra atomic relaxation or polarization energy for single hole (K^+) atom. Subtraction of the photoelectron kinetic energy from the Auger kinetic energy results in the change in the Auger parameter

$$\Delta(\alpha_{a\to e}) = 2R_e^{ea}(K^+) \tag{8}$$

for a single hole state and

$$\Delta(\alpha_{a\to e}) = 1/2R_e^{ea}(L^+L^+) \tag{9}$$

for a double hole state. Since the change in Auger parameter is equal to twice the change in extra atomic relaxation energy, it is also a direct measure of the electronic interaction with the surrounding atoms.
In 1977 Gaarenstroom and Winograd [65] evolved the idea of the modified Auger parameter, $\alpha + h\nu$, using Wagners [66] definition of the Auger parameter

$$\alpha = KE_{Auger} - KE_{PE} \tag{10}$$

and since $KE_{PE} = h\nu - BE_{PE}$

$$\alpha' = \alpha + h\nu = KE_{Auger} + BE_{PE} \tag{11}$$

The Auger parameter data can be presented together with the binding energy of a photoelectron and kinetic energy of an Auger peak in the form of two-dimensional chemical state plots (cf. Fig. 4). In this graph, the kinetic energies of Auger electrons are on the ordinate and the binding energies of the photoelectrons in decreasing order on the abscissa. Each chemical state then occupies a unique position on the two dimensional grid. An Auger parameter grid is also drawn as a family of parallel lines with a slope of +1. All points on any one of these lines have the same value of the Auger parameter. No notation of the photon energy is required and the information can be utilized with ESCA data obtained using any X-ray source [67].

2.1.5 Qualitative Analysis

The qualitative analysis is important in order to determine the different chemical states of an element. For this reason curve fitting softwares are used. A highly resolved ESCA spectrum can be synthesized by summing a series of functions representing individual peaks in order to produce a final sum function that closely represents the experimental spectrum. The peak function is generally designed to be a function of appropriate peak variables such as position, intensity, width, function type and peak tail characteristics. The peak fit is based on the non-linear least squares curve-fitting [68].

A number of types of function have been used for this purpose, the most common being Gaussian or mixed Gaussian/Lorentzian function. The later one is found to be most effective in practice:

$$f(x) = \frac{\text{peak height}}{[1 + M(x - x_0)^2/\beta^2]exp((1 - M)[ln2(x - x_0)^2]/\beta^2)} \tag{12}$$

where x_0 is the peak center and β is a parameter that is nearly half of the full width at half maximum (FWHM). The actual FWHM is calculated from β using an iterative method. M is the mixing ratio and takes the value 1 for a pure Lorentzian peak and 0 for a pure Gaussian peak.

The shape of the spectrum background or baseline is affected by inelastic energy loss processes, secondary electrons and nearby peaks. A reasonable approximation is essential for a qualitative and quantitative analysis of XPS data especially if several components interfere in one spectrum.

Although in some cases the Shirley model [69] fails, it is an accepted and widely used approximation for the inelastic background of core level peaks of buried species, which suffered significantly from inelastic losses of the emitted photoelectrons. The calculation of the baseline is an iterative procedure.

As an example the results of the peak fit analysis using Equation (12) and Shirley background for a halogenated chromia sample are shown in Figures 4 and 5.

2.1.6 Quantitative Analysis

It is important to determine the relative concentrations of the various elemental constituents of a sample surface, for many XPS investigations. There are methods for quantifying the XPS measurement utilizing peak area and sensitivity factors.

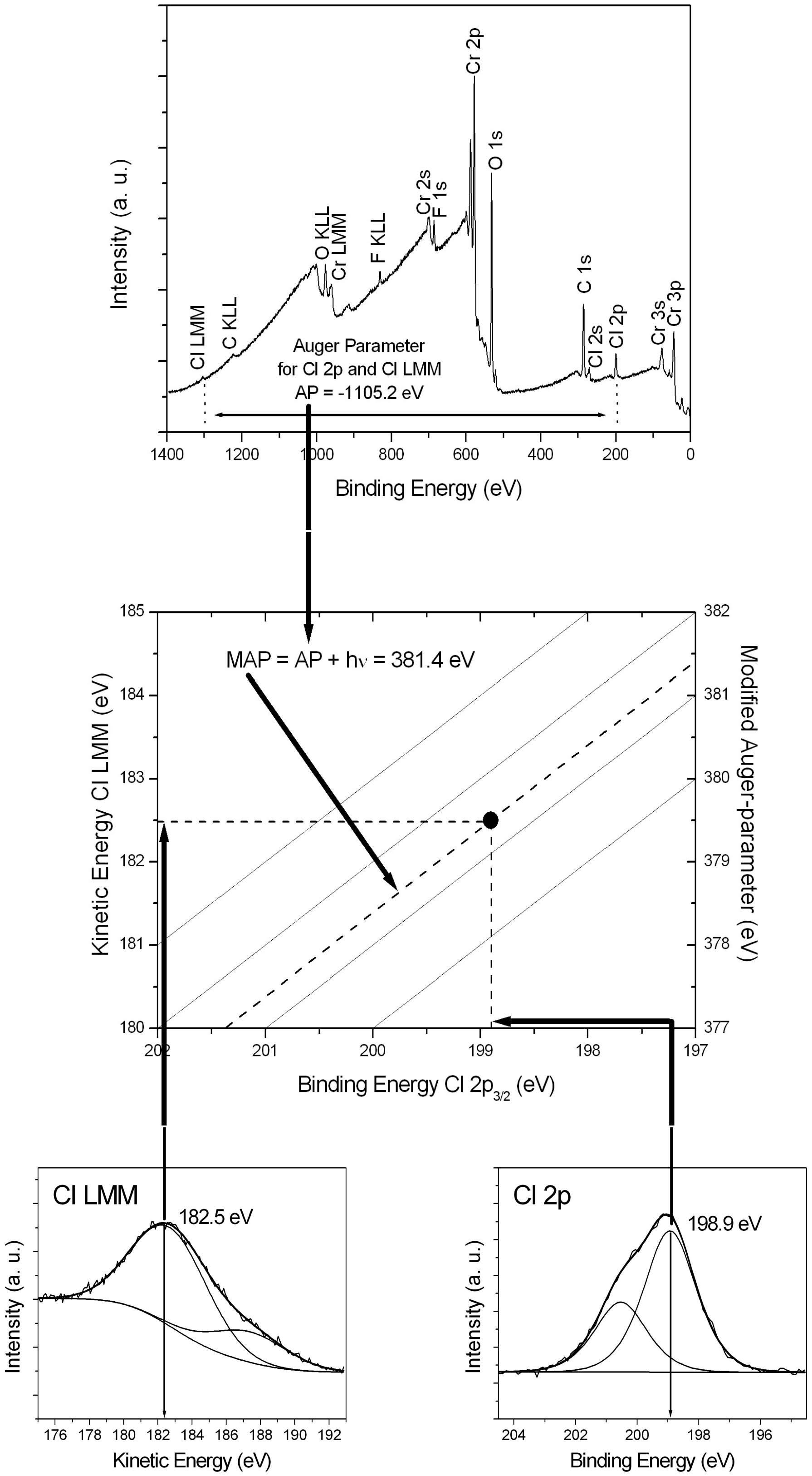

Figure 4: Illustration of how to create a chemical state (Wagner) plot. Wide scan of halogenated chromia (top), chemical state plot for Cl (center), Cl LMM Auger peak and Cl 2p photoelectron peak with fit results (bottom). AP: Auger parameter, MAP: Modified Auger parameter

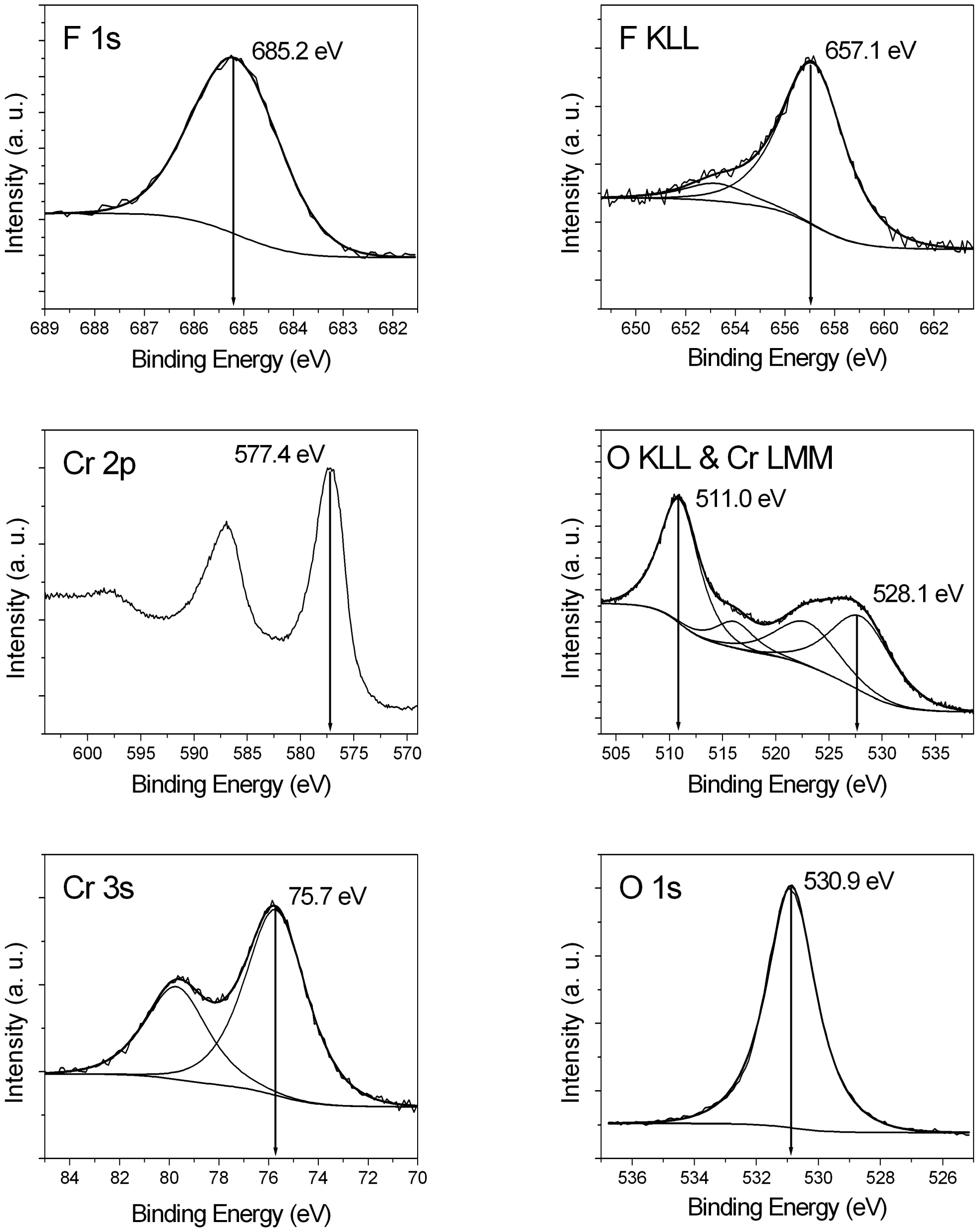

Figure 5: Narrow scans of photoelectron and Auger peaks of halogenated chromia with fit results. For fitting the Cr 2p spectrum see also page 44 in Section 3.3.1.

For transition metal spectra with prominent shake-up peaks, it is best to include the entire 2p region when measuring peak areas.

For a sample that is homogeneous in the analysis volume, the number of photoelectrons per second in a XP spectrum is given by [70]:

$$I = nJ\sigma DTLA\lambda cos\theta \tag{13}$$

where n is the number of atoms of the element per cm^3 of the sample,
J is the X-ray flux in photons/cm^2.sec,
σ is the photoelectric ionization cross-section for the atomic orbital of interest in cm^2,
D is the detection efficiency for each electron transmitted by the electron spectrometer,
T is the analyzer transmission,
L is the angular asymmetry of the intensity of the photoemission from each atom,
A is the area of the sample from which photoelectrons are detected,
λ is the inelastic mean free path of the photoelectrons in the sample,
θ is the angle of emission of the electron from the surface normal,
From Equation (13):

$$n = I/J\sigma DTLA\lambda cos\theta \tag{14}$$

The denominator in Equation (14) can be defined as the atomic sensitivity factor, S. If a peak from each of two elements are considered, then:

$$\frac{n_1}{n_2} = \frac{I_1/S_1}{I_2/S_2} \tag{15}$$

This expression may be used for all homogeneous samples if the ratio S_1/S_2 is matrix independent for all materials. Thus, for any spectrometer, it is possible to develop a set of relative values of S for all of the elements. Multiple sets of values are necessary for instruments with multiple X-ray sources at different angles relative to the analyzer and different X-ray energies.

A general expression for determining the atom fraction of any constituents in a sample, C_x , can be written as an extension of Equation:

$$C_x = \frac{n_x}{\sum n_i} = \frac{I_x/S_x}{\sum I_i/S_i} \tag{16}$$

The use of atomic sensitivity factors in the manner described will normally furnish semiquantitative results with an accuracy of 10-20%.

2.2 X-ray Absorption Spectroscopy (XAS)

X-ray Absorption Spectroscopy (XAS) is the modulation of the X-ray absorption coefficient at energies near and above an X-ray absorption edge. XAS is also referred to as X-ray Absorption Fine Structure (XAFS) and is broken into two regimes: Extended X-ray Absorption Fine Structure (EXAFS) and X-ray Absorption Near Edge Spectroscopy (XANES). The first one provides information about near neighbour distances and coordination number as the later one contains information about formal valence and coordination chemistry.

When a monochromatic X-ray beam is directed through a sample, and as the energy of the X-ray is gradually increased such that it crosses an absorption edge of one of the elements of interest in the sample, the transmitted X-ray light will contain small variations in absorbance, on the high energy side of the absorption edge, that provide information about the structural environment of the atoms surrounding the element whose absorption edge is being examined.

As discussing X-ray absorption, it is primarily concerned with the absorption coefficient, a which gives the probability that X-rays will be absorbed according to Beer's Law:

$$I = I_0 e^{-at} \tag{17}$$

where I_0 is the X-ray intensity incident on the sample, t is the sample thickness, and I is the intensity transmitted through the sample.

The X-ray absorption spectrum can be divided into near edge and extended fine structure. The X-ray absorption near-edge structure (XANES) is extended in the first 30-40 eV behind the absorption edge, while the extended X-ray absorption fine structure (EXAFS) covers the photon energy range from about 40 eV to about 1000 eV behind the absorption edge. The interpretation of XANES spectra is different from EXAFS spectra.

XANES is associated with the excitation process of a core electron to bound and quasi-bound states, where the bound states are located below the ionization threshold (vacuum level) and the quasi-bound states are located above or near the ionization threshold. As an example the XAS of Cr K-edge is shown in Figure 6. The first peak A denotes the pre-edge absorption, the dipole forbidden $1s \rightarrow 3d$ transition. The dipole allowed $1s \rightarrow 4p$ transition is assigned as peak B. The peaks following this one in the near edge region appear due to multiple scattering. The oscillations due to single scattering processes are labeled with D. Like EXAFS, XANES contains information about the electronic state of the X-ray absorbing atom and the local surrounding structure. However, unlike EXAFS, since the excitation process essentially involves multi-electron and multiple scattering interactions, simulation and modeling of XANES spectra is substantially more complicated. Therefore, finger

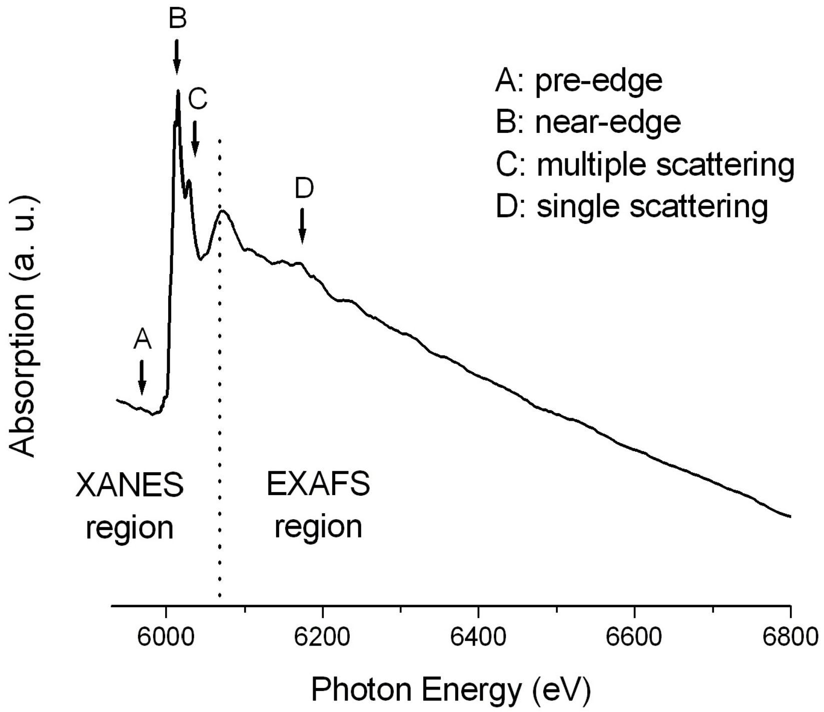

Figure 6: X-ray absorption spectrum of Cr K-edge for Cr_2O_3

print approach is used by the interpretation of spectra.

There are various detection techniques in the XAS experiments. The experimental methods in XAS differ by the used detection technique. Some of them are fluorescence yield (FY), total electron yield (TEY) and transmission mode experiments.

The fluorescent decay of the core hole is used as the basis for the absorption measurement in the FY experiments. The photon created in the fluorescent decay has a mean free path of the same order of magnitude as the incoming X-ray, therefore it is not a surface sensitive technique. It means that there will be saturation effects if the sample is not dilute.

The most abundant yield detection technique is TEY. The energy of the outgoing electrons is not selected and all escaping electrons are counted. The signal is dominated by secondary electrons which are created in the cascade process of the Auger decay electrons. It is a surface sensitive technique. The ease of detection and the large signal make total electron yield a much used technique.

In a transmission experiment the absorption of the sample is measured by monitoring the incoming (I_0) and the transmitted I flux, which are related by the Equation 17. Information obtained from the transmission measurements reflects the local structure of the bulk material.

2.3 The relationship between XPS and XAS

The XPS and TEY-XANES analysis are surface sensitive methods. The XP spectra of transition insulators and their TEY-XANES spectra show some similarities.
Ejection of a core electron from a given orbital in a molecule or atom having a closed shell configuration normally will result in only one final state. However, if there are unpaired valence electrons, more than one final state can occur upon creation of an inner-shell vacancy, because the exchange interaction will effect the spin-up and spin-down core electrons differently. This is denominated as multiplet splitting [71]. The $L_{2,3}$-edges XAS of first row transition elements are characterized by very sharp multiplet features and there are no shake up satellites (cf. Sec. 2.1.3) present. In XPS the X-ray photon is of sufficient energy to excite the photoelectron to a final energy that is well above the ionization threshold. In contrast, the lowest

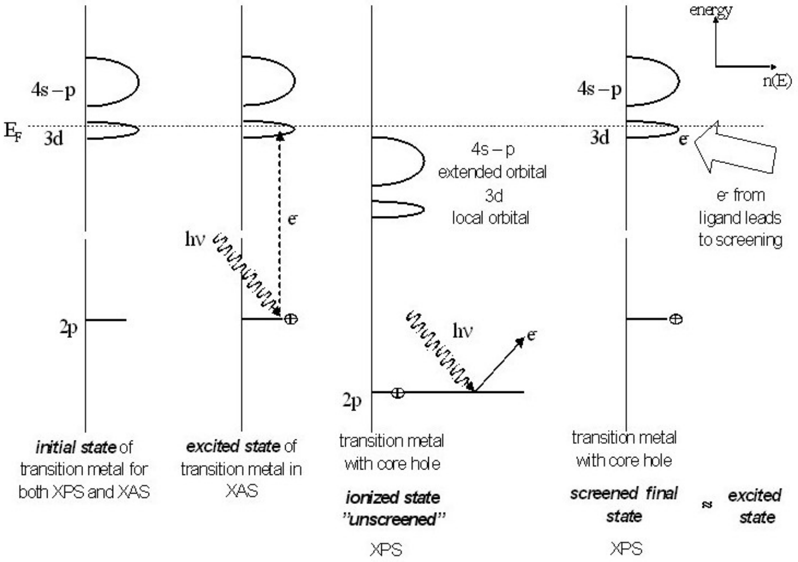

Figure 7: The relationship between XPS and XAS for transition insulators. Adapted from ref. [2].

energy transitions observed in XAS occur at photon energies less than the ionization threshold. These bound state transitions involve final states below the vacuum level. However, despite this difference, the final state multiplets occur at the same relative energies in the two spectroscopies [72] meaning that the metal ion is left in the same final state in both experiments. For example, the Fe(III) $L_{2,3}$-edge XAS transitions in α-Fe_2O_3 can be described as $2p^6 3d^5 \rightarrow 2p^5 3d^6$ (cf. Fig. 7). On the other hand, the photoemission from Fe $2p_{3/2}$ and $2p_{1/2}$ levels creates a core hole leading to a charge transfer from ligands to metal valence band which is a very well known process for transition metal insulators [2]. Therefore, this screened final state of Fe(III) has the $2p^5 3d^6$ configuration. Thus theoretical and practical predictions of the satellite free and sharper XAS multiplet structure can be used as a starting point to simulate the more complex and less well resolved XPS multiplet manifolds in an analysis of highly resolved XP spectra.

.

3 Results and Discussion

3.1 Complexity of Cr 2p X-ray Photoelectron Spectrum

XPS core level p orbitals are often found as a doublet with a doublet splitting energy difference and an intensity ratio of 1:2 due to different energy levels and occupations of the $p_{3/2}$ and $p_{1/2}$ orbitals.

The simplest multiplet splitted spectrum is expected for a core s level. If the ejected electron is from a core s level of a paramagnetic atom, two final states will occur. Discussion of the theoretical basis for multiplet splitting in XPS was first made in the late 60s. Later in mid 70s a comprehensive theoretical treatment were also given for the 2p core levels in transition metal compounds. Gupta and Sen [73] calculated the multiplet structure of core 2p vacancy levels for free ions of 3d transition metals. On the other hand, it is also known for a rather long time that photoelectron spectroscopic measurements of core electron levels in cations of transition series insulators commonly show satellite features on the high binding energy side of the main peaks. These satellites are generally called shake-up peaks to designate an excitation of a valence electron to a higher unfilled level as one system response to the loss of a core electron due to photoemission. However, the process which leads to this satellite structure was later understood. Veal and Paulikas [2] examined the relationship between main peaks and adjacent satellites for 3d series insulators and they based their investigations on a relaxation model of the photoinduced core hole, which is able to explain XPS core level binding energies and energies of the satellites. They also found for the satellites a considerable sensitivity to chemical effects. In the case of the Cr 2p spectrum, the satellite of the Cr $2p_{3/2}$ peak strongly overlaps the Cr $2p_{1/2}$ peak resulting in a virtual three peak spectrum. The problem of how this satellite should be taken into account may be one reason why in most of the published Cr(III) 2p data the satellite structure is not considered. Grohmann et al. [74] proposed a fitting formalism for Cr(III) 2p spectra of various chromium compounds by explicitly considering the satellite structure and using the relaxation model. However, they did not consider the multiplet structure for Cr(III) 2p spectrum.

Considering the multiplet structure of Cr(III) 2p levels is not easy, since Gupta and Sen [73] calculated the multiplet pattern comprising 65 multiplet states for a Cr(III) free ion ignoring the crystal field effects. When the crystal field effects are significant one might expect a different pattern, and therefore the calculated pattern can be inapplicable in spectral analysis.

In addition, there is another problem, which should also be mentioned here, in Cr 2p XP spectral analysis. The Shirley background, which is an estimation for the electrons with inelastic energy loss, does not represent the real physics in the Cr 2p binding energy region. It can not be drawn without crossing the spectrum in a wide energy range window including also the high binding energy satellite.

In the literature a group of researchers based their spectral analysis on multiplet structure but without considering the satellite structure. However, another group of researchers make their spectral analysis by taking into account for the satellite structure using the relaxation model and ignoring the multiplet features.

For a more correct chemical analysis the spectral features of the Cr(III) 2p spectrum should be better understood and a proper fit procedure should be developed or an alternative way of analysis should be proposed.

3.2 Cr 2p X-ray Photoelectron Spectra for Cr(III) compounds of O, F and Cl

The XRD pattern of the Cr_2O_3 reference sample is in good agreement with PDF 38-1479, Eskolaite. That result gives confidence on the identity of the crystalline bulk component of the sample under investigation.

The Cr 2p photoelectron spectrum of Cr_2O_3 taken with the ESCALAB 200X spectrometer shows a significant asymmetry in both the Cr $2p_{3/2}$ and $2p_{1/2}$ peaks. This asymmetry could originate either from a co-existing Cr binding state, which was suspected to be a Cr species bound to OH or adsorbed water, or might be considered as a consequence of multiplet splitting for Cr^{3+} in Cr_2O_3 together with superimposed satellite features. To check this, Cr_2O_3 was dried at 360 $°C$ in vacuo or calcined at 800 $°C$. Relying on literature data, adsorbed water and hydroxide should disappear from the samples' surface by desorption or decomposition when Cr_2O_3 is treated as described [75], [76]. However, no significant changes in the shape of the Cr 2p spectra due to this post-treatments of Cr_2O_3 were found. Alternatively, Cr_2O_3 was also synthesized from CrO_2 (Aldrich) by heating this to 800 $°C$ under Ar flow. The Cr 2p spectrum of this sample shows the same shape and features as the previous ones. The conclusion is that at least the spectra of these samples really represent the spectrum of Cr 2p for Cr_2O_3. Another evidence for this conclusion can be derived from an analysis of the corresponding O 1s spectra. The O 1s peak consists of two sub-peaks, the major one at BE ~530 eV related to the oxide and the other one at BE ~532 eV to the hydroxide [77]. The relative peak areas of the hydroxide according the total O 1s signal are 8.9 % for the untreated Cr_2O_3, 8.1 % for the Cr_2O_3 dried at 360 $°C$ in vacuo, 5.8 % for the one calcined at 800 $°C$ and 2.6 % for the one synthesized from CrO_2 by calcination at 800 $°C$. Although the hydroxide surface concentration substantially decreases, the shape of the Cr 2p peak did not show any change.

Cr_2O_3 was also analyzed with latest generation X-ray photoelectron spectrometers which are able to measure non-conductive powder samples with ultimate energy resolution. The main reason for the enhanced resolution was that these new spectrometers have advanced charge compensation tools and leading edge monochromators. These spectra (cf. Fig. 8) reveal that the Cr 2p$_{3/2}$ peak, showing a low BE shoulder in the ESCALAB spectra given in Fig 9, splits into a number of components. Obviously, these should be due to multiplet splitting.

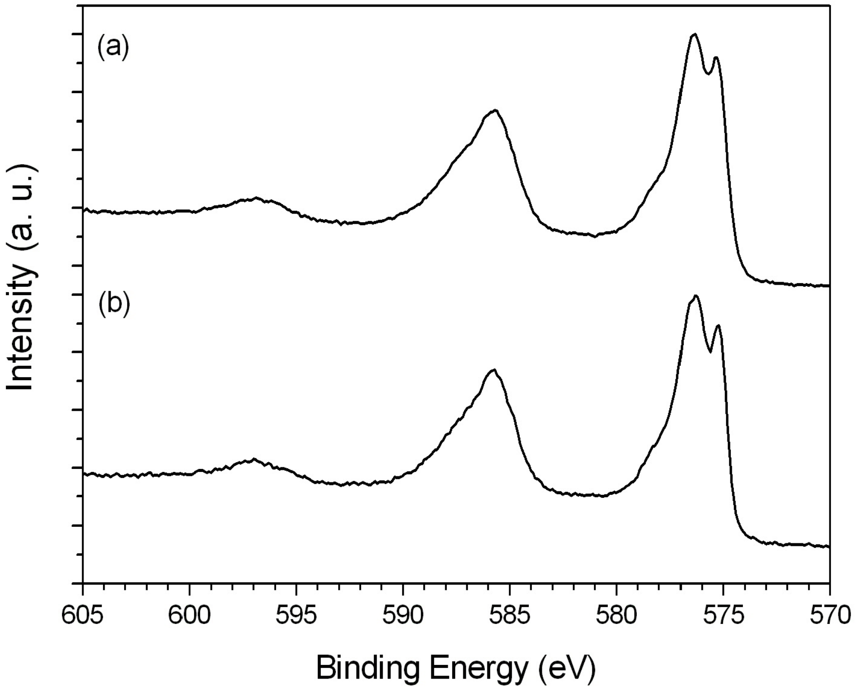

Figure 8: Cr 2p spectra of Cr_2O_3 measured by (a) Thermo VG Scientific ESCALAB 250 and (b) Kratos Axis ULTRA electron spectrometers using monochromatized Al Kα excitation, flood gun and a magnetic lens for charge compensation.

Very similar high energy resolution spectra of Cr 2p$_{3/2}$ were obtained by Chambers and Droubay [78] for a Cr_2O_3 thin film sample grown on a Pt(111) substrate. These were also interpreted to be due to multiplet splitting for Cr^{3+}. Unfortunately, the authors of ref. [78] published only Cr 2p spectra in an energy window from BE 595 eV to 570 eV. Therefore, these spectra cannot be fully compared with the Cr_2O_3 powder sample Cr 2p spectra comprising all satellite features up to BE = 605 eV.

In order to develop a satisfying fit procedure for Cr 2p spectra one has to consider at first a background problem. It is impossible to draw a common Shirley background from 570 to 610 eV without crossing the Cr 2p spectrum between the Cr 2p$_{1/2}$ contribution and its satellite (cf. [74]). The Scienta ESCA-300 software (Version 1.66, SCIENTA AB-Uppsala), the CASA XPS software (Version 2.0, Casa Software Ltd.) and the Unifit software (Version 2003, University of Leipzig) were tried but every software failed here. Thus the Shirley background approximation is

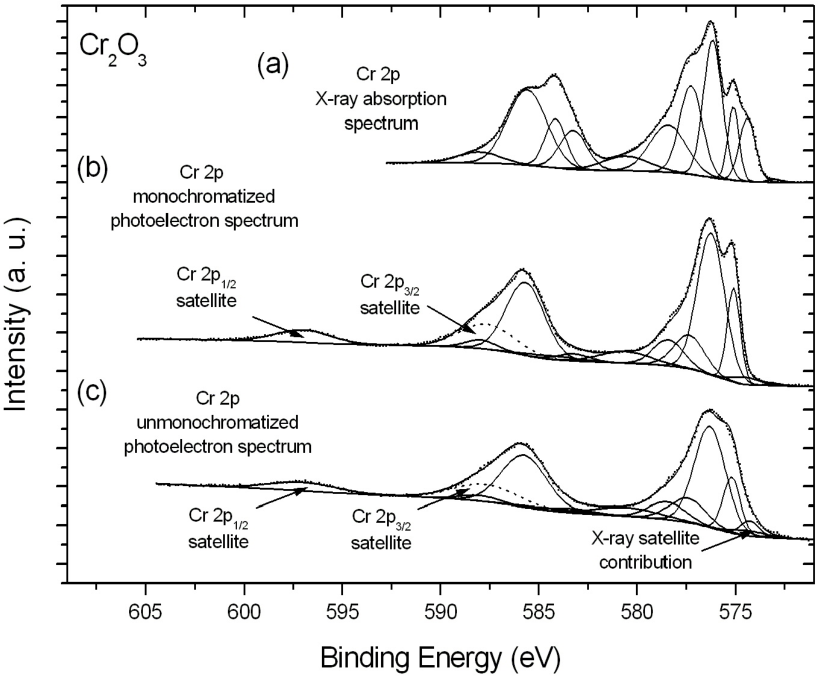

Figure 9: Cr_2O_3 Cr L-edge XANES (a) and Cr 2p XP spectra of Cr_2O_3 obtained with (b) monochromatized and (c) non-monochromatized Al Kα radiation which are fitted considering multiplet splitting as well as satellite structures and a modified Shirley background was used. Spectrum (b) was taken with and spectrum (c) without active charge compensation. Total electron yield XANES was obtained at the HE-SGM monochromator beamline at the synchrotron radiation source BESSY II using 50 μm slits.

not able to model the real physics in that case. A pragmatically modified Shirley background which is capable of setting up a background without crossing the spectrum was found to solve the problem. It consists of a combination of the Shirley background with a linear function. Finally, the Unifit 2003 software was used for the analysis of the spectra.

At the beginning of the investigations it was tried to fit the Cr 2p spectrum of Cr_2O_3 with doublets constrained to the theoretical spin-orbit intensity ratio of 2:1 for the main peaks as well as for the satellite doublet. $2p_{3/2}$ - $2p_{1/2}$ peak separations of all doublets and satellites were also set to be constraints (cf. also [74]). However, severe problems were faced to get a satisfying result. When it becomes convincingly clear from the experiments reported above that the multiplet splitting within Cr 2p spectra must be considered, an appropriate approach is required in order to handle this fact. A starting point was derived from the theoretical work of Gupta and Sen [73] who calculated 65 multiplets for the 2p orbital of the Cr^{3+} free ion. In the XP

Table 1: Results for fitted parameters of the highly and ordinarily resolved Cr 2p XP spectra for Cr_2O_3 shown in Fig. 9, graphs b and c

	Highly resolved spectrum			Ordinarily resolved spectrum		
Peak	BE (eV)	FWHM (eV)	Area (%)	BE (eV)	FWHM (eV)	Area (%)
1	573.00	1.04	0.19	573.05	1.25	0.18
2	574.45	1.71	1.49	574.35	2.07	1.62
3	575.10	0.80	9.31	575.20	1.06	8.85
4	576.25	1.66	29.28	576.30	1.90	28.96
5	577.35	1.85	7.77	577.45	2.19	7.92
6	578.40	1.82	5.85	578.50	2.19	5.82
7	580.60	3.08	4.43	580.50	3.72	4.81
8	583.20	1.91	1.66	583.30	2.54	1.58
9	584.25	2.99	1.35	584.30	3.42	1.34
10	585.70	2.33	21.11	585.75	2.75	21.54
11	587.95	1.86	2.00	588.00	2.25	1.89
Sat.I	587.65	3.33	10.38	587.70	4.02	10.32
Sat.II	597.00	3.33	5.19	597.05	4.02	5.16

Sat.I: Satellite of Cr $2p_{3/2}$ and Sat.II: Satellite of Cr $2p_{1/2}$

spectrum this results in a manifold of contributions. Obviously, XPS is not able to resolve all the individual multiplet components. Also with the highest resolution available, only certain bundles of large numbers of closely spaced multiplets, where these are merging together to spectroscopically distinguishable spectral features of sufficient intensity, were observed. One cannot distinguish unequivocally how Cr $2p_{3/2}$ or $2p_{1/2}$ photoemission contributes to a resolved bundle of multiplets. Therefore neither a theoretical Cr $2p_{3/2}$ to $2p_{1/2}$ intensity ratio nor $2p_{3/2}$-$2p_{1/2}$ component separations can be used as constraints in a fitting procedure to be applied to the XP spectrum. Moreover, it is well known from XANES spectra of L-edges of transition metals that there are severe differences in the spectral shape and also in the intensity of the L_3 and L_2-edges. The L_3:L_2 intensity ratio is found to deviate from 2:1 [79]. It was proposed by Droubay and Chambers [72] for the equivalent case of Fe_2O_3, which is also a trivalent transition metal compound, to use the multiplet related fine structure manifest in the Fe L_3 and L_2 absorption edges to get initial values (binding energy, FWHM and relative intensity) for fitting the XP Fe 2p spectrum. Moreover, it may be derived some advantage from the fact that the XANES Fe L_3 and L_2-edges absorption spectra are free from satellite contributions.

The strategy of Droubay and Chambers [72] was adopted by starting with an analysis of the XANES spectrum of Cr_2O_3. The energy positions of all of the manifest multiplet bundles in the Cr(III) L-edge XANES spectrum were used as initial values for fitting of Cr 2p XP spectra. 11 peaks could be distinguished in the complete Cr(III) L-edge XANES spectrum which are taken to represent bundles formed out of the supposed 65 multiplets of Cr^{3+} [73] (cf. Fig. 9, graph (a)). These peak positions were transferred as starting values with a tolerance of ± 0.05 eV into the set of starting parameters used for analysis of the highly resolved Cr 2p spectrum of Cr_2O_3. As proposed by Droubay and Chambers [72] multiplet heights should be set free to vary in order to compensate for the differences of coupling between the core hole and valence electrons in XPS and XANES. FWHM values were also set free to vary to compensate for different lifetime broadening. The so-called Gaussian-Lorentzian (G/L) mixing ratio in the UNIFIT software was fixed to 0.1 meaning that a 10 % Lorentzian peak contribution to the GL product function was used. One additional doublet with an area ratio 2:1 was added for the satellites in the photoemission spectrum. The result of this fit (cf. Fig. 9, graph (b)) was used to provide starting parameters for fitting the Cr 2p spectrum taken with the ESCALAB 200X using the non-monochromatized Al Kα X-ray radiation. Here, X-ray contributions arising from the K$\alpha_{3,4}$ satellites were also taken into account [80] (cf. Fig. 9, graph (c)). Figure 9 and Table 1 show results of this strategy of fitting [81].

The same strategy of fitting was also applied for the $\alpha - CrF_3$ and $CrCl_3$ (cf. Fig. 10 and 11). Similar results are also reported for the $\beta - CrF_3$, $CrF_3.H_2O$, CrF_2OH and $Cr(OH)_3$ samples [82]. Although in all of these samples the chromium is in Cr^{3+} oxidation state, the multiplet splitting and satellite structures in the Cr 2p XP spectra of these samples show at least slight or even significant differences. The energy positions of the manifest multiplet bundles in these spectra alter with different chemical structure and chemical environment. Therefore, the calculated multiplet structures from the supposed 65 multiplets of Cr^{3+} free ion according to Gupta and Sen [73] might not be applicable for peak fitting of any Cr 2p XP spectrum of a chromium(III) compound. In their estimations they did not consider the crystal field effects which seem to have an effective role for the features of the spectral structure. In order to better indicate this effect, the center of gravity of the most intense point of the Cr $L_{2,3}$-edge XANES spectra of these chromium(III) samples are coincided one under the other so that the other points which are also significantly resolved in the spectra could be compared in the point of view of energy positions. Therefore, four points (A, B, C and D) were marked in the top spectrum in Figure 12 and vertical lines are drawn from these points through. Points B and C are the most intense points of the L_2 and L_3 manifolds and A and D are the second intense points of these manifolds, respectively. The difference energy between B and C is due to doublet separation and decreases in the spectra of F containing Cr(III) compounds, because

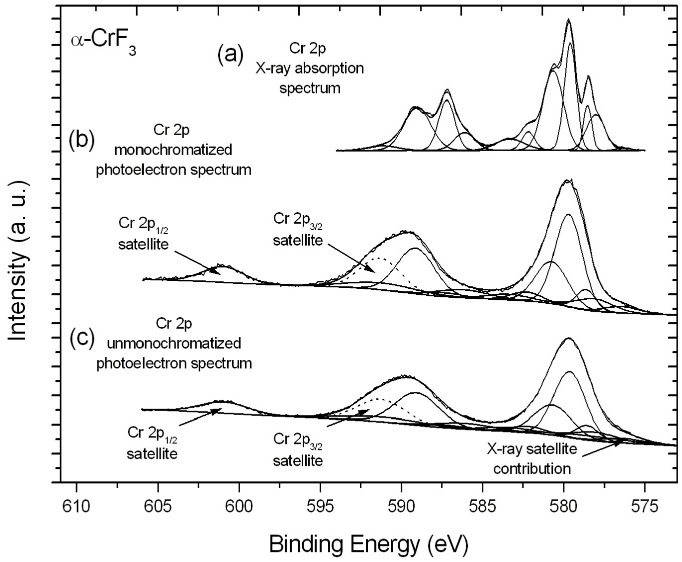

Figure 10: $\alpha - CrF_3$ Cr L-edge TEY XANES (a) and Cr 2p XP spectra of Cr_2O_3 obtained with (b) monochromatized and (c) non-monochromatized Al Kα radiation which are fitted considering multiplet splitting as well as satellite structures and a modified Shirley background was used. Spectrum (b) was taken with and spectrum (c) without active charge compensation.

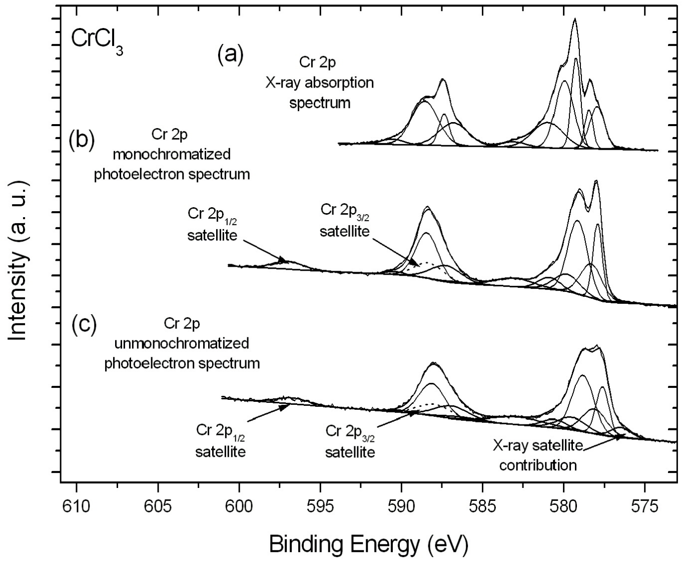

Figure 11: $CrCl_3$ Cr L-edge TEY XANES (a) and Cr 2p XP spectra of Cr_2O_3 obtained with (b) monochromatized and (c) non-monochromatized Al Kα radiation which are fitted considering multiplet splitting as well as satellite structures and a modified Shirley background was used. Spectrum (b) was taken with and spectrum (c) without active charge compensation.

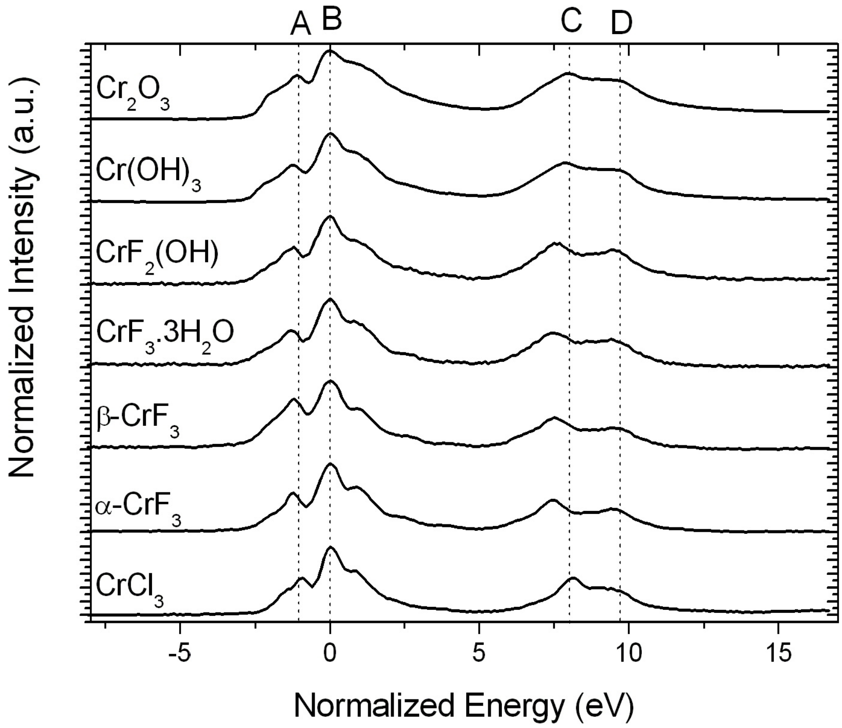

Figure 12: Normalized Cr L-edge XANES for Cr_2O_3, $Cr(OH)_3$, CrF_2OH, $CrF_3.H_2O$, $\alpha - CrF_3$, $\beta - CrF_3$, $CrCl_3$, obtained in TEY mode at the HE-SGM monochromator beamline at the synchrotron radiation source BESSY II using 50 μm slits.

F builds stronger bonds with Cr than O and Cl due to its higher electronegativity. The valence electrons are drawn stronger from F so that the electrons in core levels of Cr are shifted in the direction of nucleus. In the similar manner the splitting between points A and B are larger in the fluorine compounds most probably from the same reasons. As a result, the estimation of Gupta and Sen [73] for Cr 2p of Cr(III) XP spectrum might be a very good approximation if only the crystal field effects are not considerable. Otherwise it is not applicable.

3.3 Activation Studies and ESCA

The activation studies are performed in order to differentiate between the inactive and active species or phases which are formed on the chromia surface by Cl/F exchange reactions. Therefore, the dismutation reaction of CCl_2F_2 at 390 $°C$ in a tubular flow reactor is chosen in order to probe the effect of Cl/F exchange reactions on chromia surface. These reactions are also performed in a simulated reaction conditions and the catalysts are characterized by ESCA "in-situ" conditions to eliminate the effect of air contamination on the catalyst surface. The dismutation reaction of CCl_2F_2 at 300 $°C$ in a tubular flow reactor is undertaken to observe the activation of the catalyst at a lower temperature. In order to understand the fluorination or chlorination of Cr_2O_3, HF or HCl treatments are performed at 390 $°C$. Finally, the effect of pre-fluorination on further chlorination of chromia and in the similar way the effect of pre-chlorination on further fluorination of chromia are investigated. All the dismutation reactions and HF or HCl treatments are performed after the Cr_2O_3 was dried at 400 $°C$ for 2 h.

Various characterization methods are used to find the difference between the inactive and active catalysts. For comparison reasons the reference samples are also characterized with the same methods. The brief introduction is given in Figure 13.

3.3.1 Dismutation of CCl_2F_2 at 390 $°C$ in a tubular flow reactor

The dismutation of CCl_2F_2, which is given by Eqn. 18 and 19, was used to probe the effect of Cl/F exchange reactions on activation of chromia. The intention is to find out how the inactive catalyst changes to an active catalyst.

$$2CCl_2F_2 \rightarrow CCl_3F + CClF_3 \tag{18}$$

$$2CCl_3F \rightarrow CCl_4 + CCl_2F_2 \tag{19}$$

As it is known from the literature chromia requires a formation process before it reaches catalytic activity. The time dependent change of concentrations of the reactant and the dismutation products can be followed by a Gas Chromatograph (GC). During the formation process the haloalkane decomposes by reacting with the adsorbed water and hydroxyl groups which saturate the metal sites at the chromia catalyst surface. Consequently, activation of chromia involves a dehydration of the surface, resulting in coordinatively unsaturated Cr(III) which can act as active site. In addition to the dismutation products $CClF_3$, CCl_3F and CCl_4, there is a formation of degradation products, CO_2, HF and HCl. The concentration of the degradation products decreases as the maximum catalytic activity is reached and the formation process is completed when the chromia catalyst is totally dehydrated.

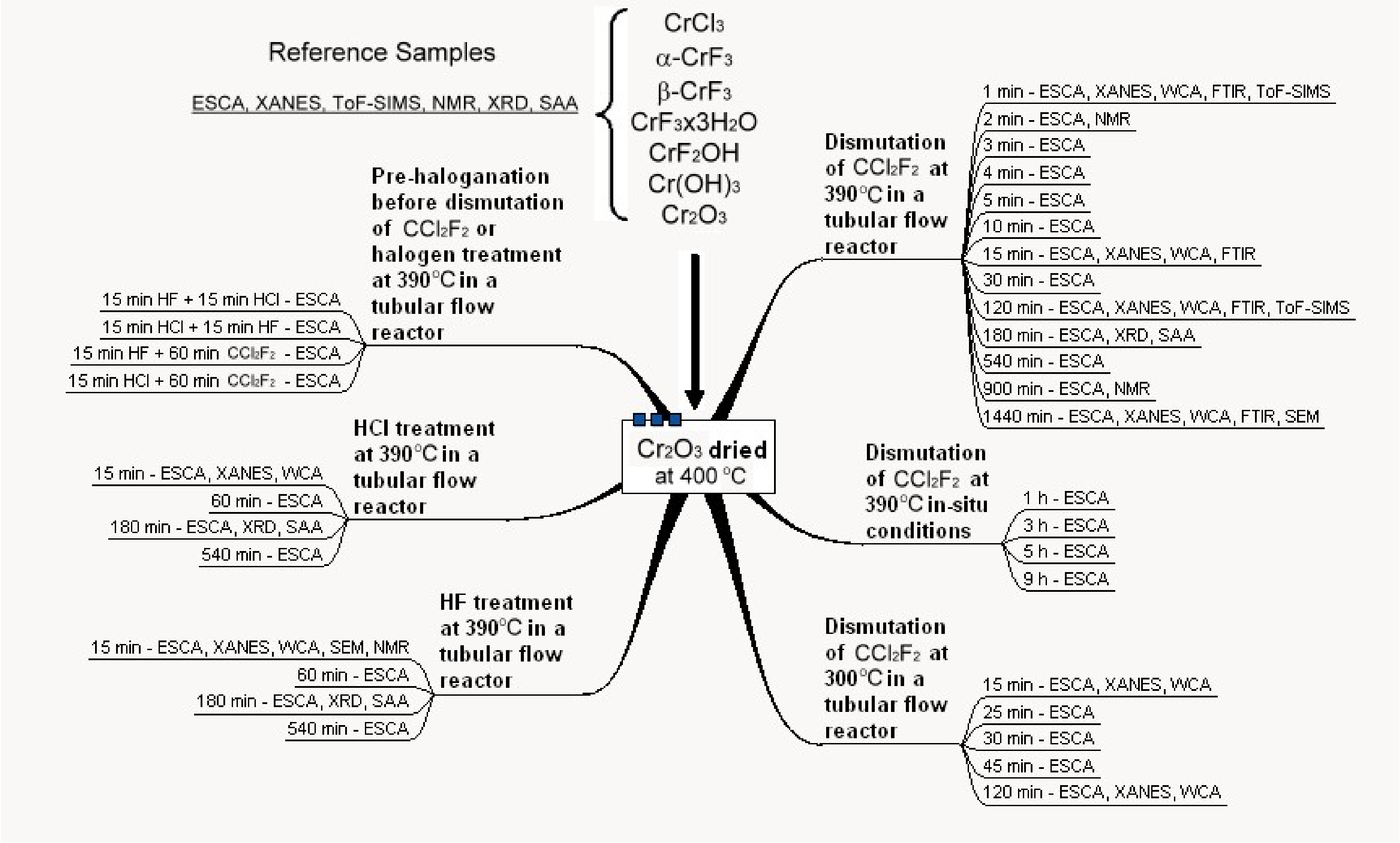

Figure 13: Overview of the samples and methods applied in the study of characterization of chromia for Cl/F exchange reactions

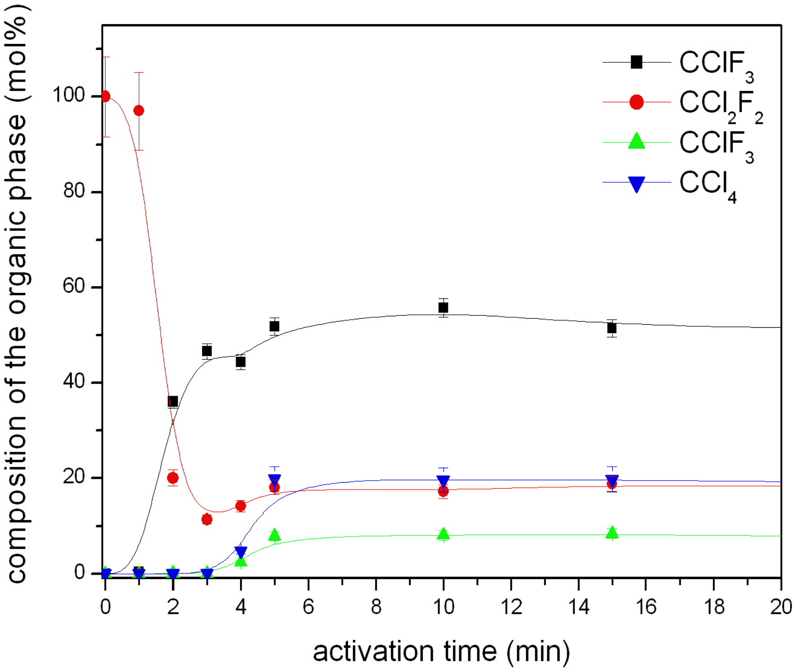

Figure 14: Cr_2O_3 catalyzed dismutation reaction of CCl_2F_2 at 390 $°C$

Before starting the formation process the chromia catalyst is dried at 400 $°C$ in a 10 ml/min N_2 stream for 2 h and then CCl_2F_2 is introduced with a flow rate of 2 ml/min. As can be seen from Figure 14 the activation of the catalyst starts about 1 min after introducing the CCl_2F_2 and within 5 min the maximum catalytic activity is reached at 390 $°C$.

The dismutation ratio (DR) should be one when only a Cl/F exchange reaction takes place among the haloalkane molecules. The Figure 15 shows that the DR deviates from one, meaning some other phenomena accompany the dismutation reaction. Since DR $<$ 1 was found between the 1st and 5th min of the activation time at 390 $°C$, higher fluorinated products and HCl are released at that period. Almost 45 % of the initial feed concentration is decomposed within the first 2 min (cf. Fig. 16). After 5 min of introducing CCl_2F_2, the dismutation reaction reaches its maximum activity (conversion ca. 80%) by completing the formation process.

In order to find out the significant differences between the inactive and active phases a number of catalyst samples are activated with dismutation reaction of CCl_2F_2 at 390 $°C$ for 1, 2, 3, 4, 5, 10, 15, 30, 120, 180, 540, 900 and 1440 min. After each reaction the catalyst samples are transferred into the glove box without exposure to air. They are prepared for the XPS analysis in the glove box and are transferred in an evacuated desiccator to the spectrometer. After placing the samples into the spectrometer within few seconds of air exposure, the chamber is pumped down to

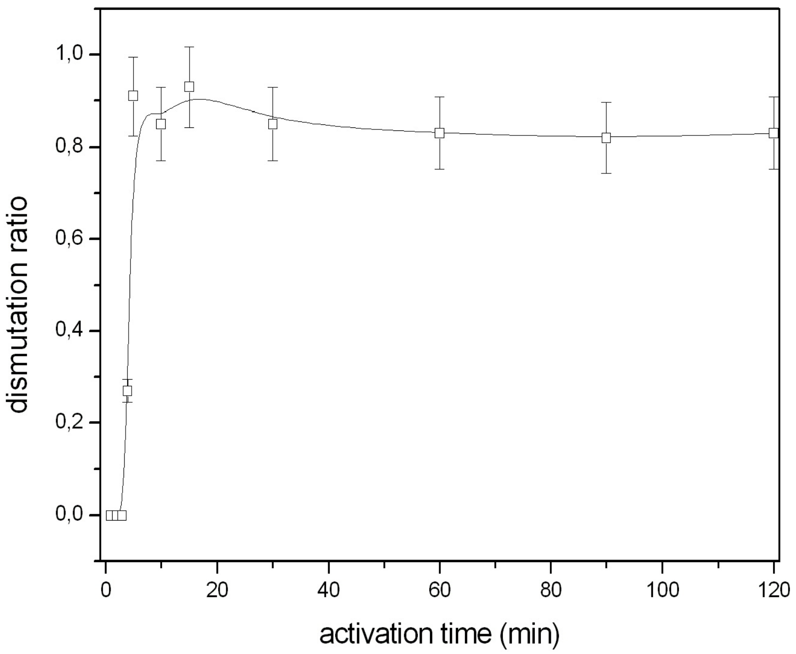

Figure 15: Dismutation Ratio (DR) for Cr_2O_3 catalyzed dismutation reaction of CCl_2F_2 at 390 $°C$

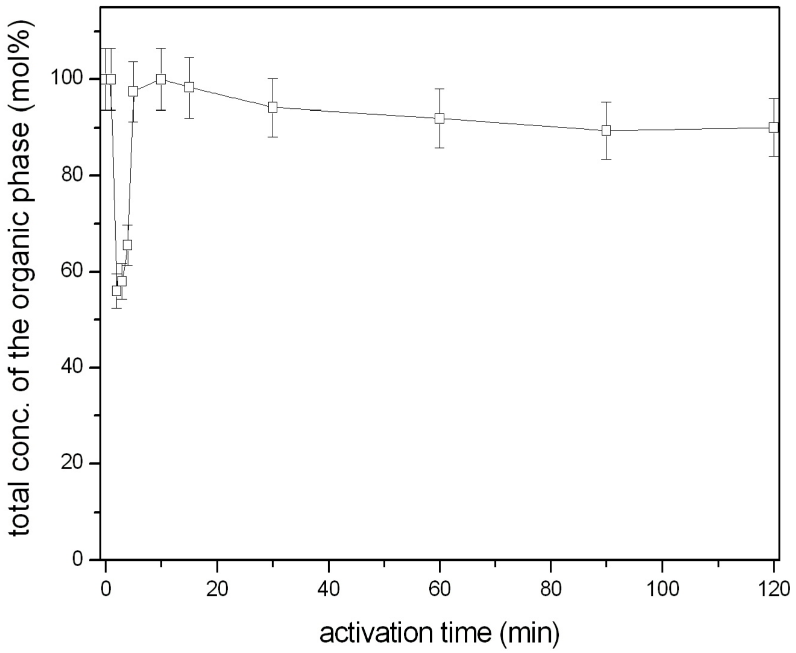

Figure 16: Total concentration of the organic phase ($CClF_3$, CCl_2F_2, CCl_3F, CCl_4) in Cr_2O_3 catalyzed dismutation reaction of CCl_2F_2 at 390 $°C$

Table 2: XPS surface composition (atom%) of Cr_2O_3 catalysts activated with CCl_2F_2 dismutation reaction at 390 $°C$

time (min)	F	Cr	O	Cl	F+Cl	F/Cr	O/Cr	Cl/Cr	F/Cl
1	**1.6**	37.1	59.1	**2.2**	3.7	0.0	1.6	0.1	0.7
2	**1.7**	38.3	55.1	**4.8**	6.6	0.0	1.4	0.1	0.4
3	**3.7**	38.3	52.4	**5.6**	9.3	0.1	1.4	0.1	0.7
4	**3.6**	39.5	50.8	**6.1**	9.7	0.1	1.3	0.2	0.6
5	**3.7**	39.9	50.7	**5.7**	9.4	0.1	1.3	0.1	0.7
10	**4.1**	38.6	51.0	**6.3**	10.5	0.1	1.3	0.2	0.7
15	**4.1**	36.1	53.2	**6.7**	10.7	0.1	1.5	0.2	0.6
30	**4.7**	38.8	51.8	**4.6**	9.4	0.1	1.3	0.1	1.0
120	**5.1**	39.0	49.0	**6.8**	11.9	0.1	1.3	0.2	0.8
180	**5.3**	38.6	49.5	**6.7**	12.0	0.1	1.3	0.2	0.8
540	**5.6**	38.8	49.7	**5.9**	11.5	0.1	1.3	0.2	0.9
900	**5.3**	38.6	49.6	**6.6**	11.9	0.1	1.3	0.2	0.8
1440	**5.1**	38.4	50.3	**6.2**	11.3	0.1	1.3	0.2	0.8

UHV and the analyses are performed under these vacuum conditions.

The 1 min activated catalyst represents the inactive phase and the catalyst samples after 5 min of activation time are catalytically active. The catalysts which are activated between these two activation times are obtained during the formation process. Table 2 shows the XPS surface compositions of these catalyst samples. Relying on these data the formation process starts significantly when the chromia surface is 1.6 atom% fluorinated and 2.2 atom% chlorinated. Chromia requires to be halogenated in order to reach the maximum activity. In other words, ca. 4 atom% fluorination and ca. 6 atom% chlorination on the catalyst surface is necessary. These results are in good agreement with the literature data [22]. However, ones the maximum activity is reached there is not much difference on the surface composition of the catalysts with increasing activation time. Even after 24 h of reaction time, there is only 5.1 atom% fluorination and 6.2 atom% chlorination found on the solid surface. The pre-dried chromia which still possesses OH groups on the surface reacts with CCl_2F_2 leading to the formation process. Since the higher chlorinated dismutation products are less stable than the higher fluorinated ones, they decompose and HCl is released with the other formation products. Therefore, more chlorination is found on the surface than fluorination. The rapid halogenation of the surface takes place until the chromia surface is eliminated from the OH groups and adsorbed water. After that point further halogenation of the solid proceeds very slightly. Although further fluorination does not dominate the chlorination, a relative increase is observed in the long run. These results are different than the ones obtained with activated alumina. Böse et al. [83] reported that 10 atom% fluorination was necessary to reach final catalytic activity. This was the total amount of halogenation in the chromia case.

The Gibbs free energies of the hydrofluorination and hydrochlorination reactions of chromia are almost the same [84] and therefore they are competitive with each other.

$$Cr_2O_3 + 6HF \rightarrow 2CrF_3 + 3H_2O \qquad \Delta G = -68 \quad kJ/mol \tag{20}$$

$$Cr_2O_3 + 6HCl \rightarrow 2CrCl_3 + 3H_2O \qquad \Delta G = -56 \quad kJ/mol \tag{21}$$

In ESCA the common practice is to apply an appropriate fit procedure to the spectrum in order to find out the BE of the photoelectrons of the relevant states (cf. Sec. 2.1.5). Since static charging is taking place for insulating materials, a reliable static charge referencing is required. The C 1s BE for aliphatic carbon (284.8 eV), which is present in solid materials due to contamination, is usually referenced to in the literature [85]. On the other hand, the Au $4f_{7/2}$ BE of metallic solid (84.0 eV) is the static charge referencing as an alternative way [86]. Therefore, well defined and chemically inert 20 nm gold particles are deposited as a nearly statistical distribution on the sample surface avoiding large coagulation effects [86]. In order to be sure that the reference C 1s BE does not change with applied reaction, the charging differences Δ between the C 1s BE referenced charging and the Au $4f_{7/2}$ BE referenced charging should be constant.

For some of the samples the charging differences are estimated by Eqn. 22. The results are tabulated in Table 3. Since the Δ charging does not change significantly for Cr_2O_3, dried Cr_2O_3 and various activated chromia catalysts, the C 1s BE can be used for static charge referencing in this study.

$$\Delta = charging\; C\; 1s - charging\; Au\; 4f_{7/2} \tag{22}$$

The activated chromia samples are halogenated therefore, different chemical states might be expected in the spectra. However, as described in Section 3.1 because of the complicated spectral features of Cr 2p it is cumbersome to follow such a fitting procedure simultaneously for all possible chemical states meaning that to handle with many peaks at the same time. This is not applicable and if it is, the results would not be reliable most probably. Since the chromia is the major compound and the fluorine and chlorine atomic concentrations are not so high, taking the BE of the corresponding maximum point in Cr $2p_{3/2}$ spectrum directly or by applying the fit procedure according to ISO 15472 [87] might be a good solution in order to overcome this difficulty (cf. Fig. 5) . Directly taking the KE at the maximum point of a complicated Auger transition is a known practice in ESCA. On the other

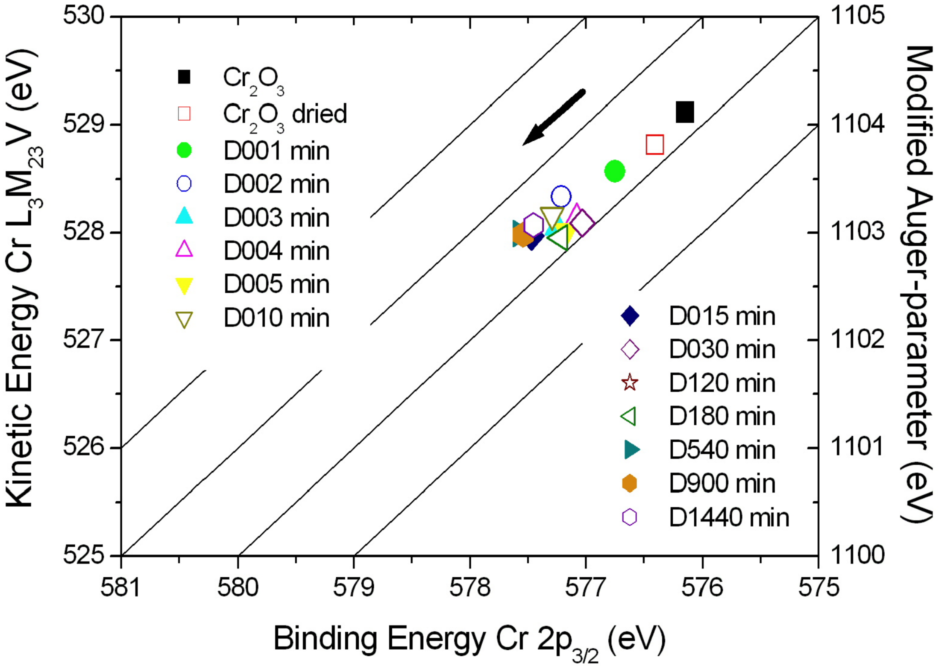

Figure 17: Chemical state plot for Cr 2p$_{3/2}$ of Cr_2O_3 samples activated at 390 °C

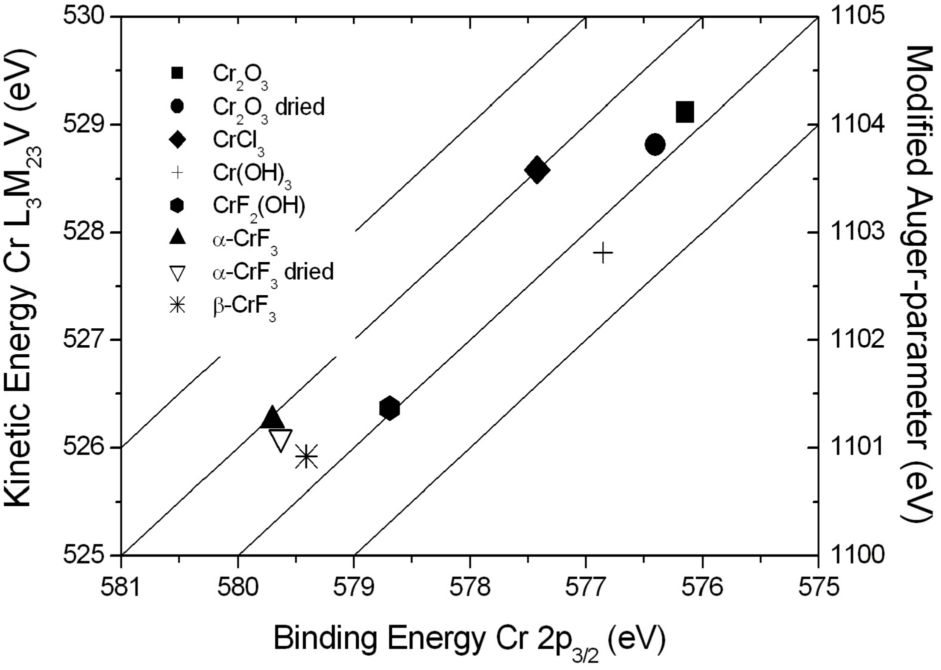

Figure 18: Chemical state plot for Cr 2p$_{3/2}$ of the reference samples

Table 3: Static charging referenced on C 1s (284.8 eV) and Au $4f_{7/2}$ (84.0 eV)

time (min)	charging C 1s	charging Au $4f_{7/2}$	Δ charging
Cr_2O_3	8.60	8.80	-0.20
dried Cr_2O_3	8.30	8.80	-0.50
1 min activated Cr_2O_3	7.90	8.35	-0.45
2 min activated Cr_2O_3	8.30	8.80	-0.50
10 min activated Cr_2O_3	8.00	8.45	-0.45
30 min activated Cr_2O_3	7.70	7.90	-0.20
540 min activated Cr_2O_3	9.30	9.80	-0.50

hand, Cr 3s can be alternatively a good candidate for ESCA, because it has a much simpler spectrum than Cr 2p. Therefore, the chemical states are also determined alternatively from Cr 3s spectrum by applying an appropriate fit procedure in order to verify the validity of the results which are obtained from Cr 2p BEs. Cr 2p BE data are common standard in XPS analysis for chromium.

The results of the relevant photoemission data obtained for the catalyst samples activated at 390 $°C$ with a dismutation reaction of CCl_2F_2 and for the reference samples are presented in chemical state plots (cf. Fig. 17 and 18) according to Wagner and Joshi [64] as explained in Section 2.1.4.

For Cr 2p different chemical states are distinguished. Especially the dried chromia has a higher BE than the untreated one. Thermal dehydroxylation of the fresh chromia increases the BE from 576.15 eV to 576.40 eV. Because of the drying process the hydroxyl groups and adsorbed water which saturate the metal sites are removed resulting in coordinatively unsaturated Cr(III) at the surface. These positively charged chromium atoms are the reason for that shift in BE and also these atoms attract the valence electrons of the neighbour oxygen atoms causing to increase the BE in core levels of the oxygen as well. A shift of 0.40 eV is observed in O 1s line. The O 1s spectrum of fresh chromia has an asymmetry at the high binding energy side. It consists of two sub-peaks with binding energies at 529.85 eV and 532.00 eV which are characteristic for O of metal oxide and OH groups, respectively [77]. The relative peak areas of the hydroxide reduces from 9.1 % to 2.9 % of the total O 1s signal by thermal dehydroxylation. The constant modified Auger parameter α' for Cr $2p_{3/2}$ suggests that the extra atomic relaxation energy is not changing and so the shift in BE can be discussed in terms of initial state effects. For the catalyst sample obtained by the dismutation reaction at 390 $°C$ for 1 min, a further increase in the Cr $2p_{3/2}$ BE by 0.35 eV was observed at constant α'. At this stage the formation process has just begun and the surface is 1.6 atom% fluorinated and 2.2 atom% chlorinated. After 2 min activation time the Cr 2p$_{3/2}$ line shifts further to higher BE by 0.45 eV and until maximum activity, where the surface is 3.7 atom% fluorinated and 5.7 atom% chlorinated, is reached there is no further significant change in the Cr 2p$_{3/2}$ BE. Further slight increases are observed in the Cr 2p$_{3/2}$ BE with increasing reaction time. Maximal 0.3 eV shifts are found in the Cr 2p$_{3/2}$ BE and the surface is 5.1 atom% fluorinated and 6.2 atom% chlorinated up to 24 h reaction times.

The surface undergoes dramatic changes in the first few minutes of the dismutation reaction of CCl_2F_2 at 390 $°C$. The dried chromia still possesses some residual OH groups which are exchanged with F and Cl with the introduction of CCl_2F_2. Since the Cr-F and Cr-Cl bonds are stronger than Cr-O and Cr-OH bonds, an increase at the Cr 2p$_{3/2}$ BE is not unexpected. The difference in the Cr 2p$_{3/2}$ BE of the untreated chromia and the just conditioned catalyst is 1.1 eV. However, the further increase of the Cr 2p$_{3/2}$ BE is only 0.3 eV even after 24 h reaction time. Once the formation process is completed further fluorination and chlorination into the crystal lattice proceeds slowly. The oxygen/halogen exchange increases also the Cr 2p$_{3/2}$ BE, especially due to the replacement of less electronegative oxygen by a more electronegative fluorine. Inspection of the Cr 2p spectra do not revel any significant alteration. There is no indication of either broadening of the spectrum, growth of a shoulder or of another emission line. This indicates that within the detection limits of XPS no nucleation of a separate fluorine and chlorine containing phases in the Cr_2O_3 matrix takes place. In addition, α' for Cr 2p$_{3/2}$ does not change significantly meaning that the extra atomic relaxation energy is not changing and therefore the chemical shifts can be considered in terms of initial state effects. The integration of halogen into the Cr_2O_3 lattice by substituting the oxygen ion increases the positive charge at the chromium metal site. Since fluorine is more electronegative than oxygen. All these catalyst samples are plotted in between the data points of chromia and chromium fluorides in the chemical state plots of Cr 2p$_{3/2}$. They are more on the Cr_2O_3 side and far away from the α- and $\beta - CrF_3$. As a result, oxide-fluoride or oxide-halide species are formed on the catalyst surface.

The same conclusion can also be derived when the satellite of Cr 2p$_{1/2}$ in the Cr 2p XP spectrum is considered. The BEs of these satellites are found to be 596.7, 597.0 and 601.0 eV for $CrCl_3$, Cr_2O_3 and $\alpha - CrF_3$, respectively (cf. Fig. 11, 9 and 10). For the activated Cr_2O_3 samples the BE values of Cr 2p$_{1/2}$ satellites in the Cr 2p spectra are around 598.00 $\mp$ 0.25 eV, which are absolutely different than the Cr 2p$_{1/2}$ satellite BEs of the references. Hence, chromium oxide halide species are expected at the surface.

As given the reasons above, similar chemical state plots of Cr 3s for the activated

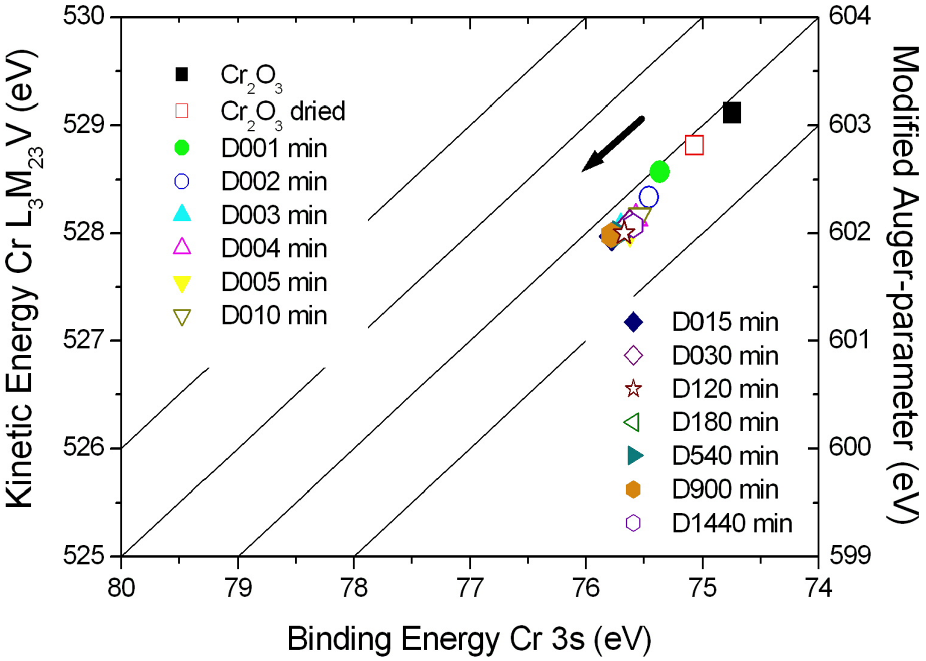

Figure 19: Chemical state plot for Cr 3s of Cr_2O_3 samples activated at 390 °C

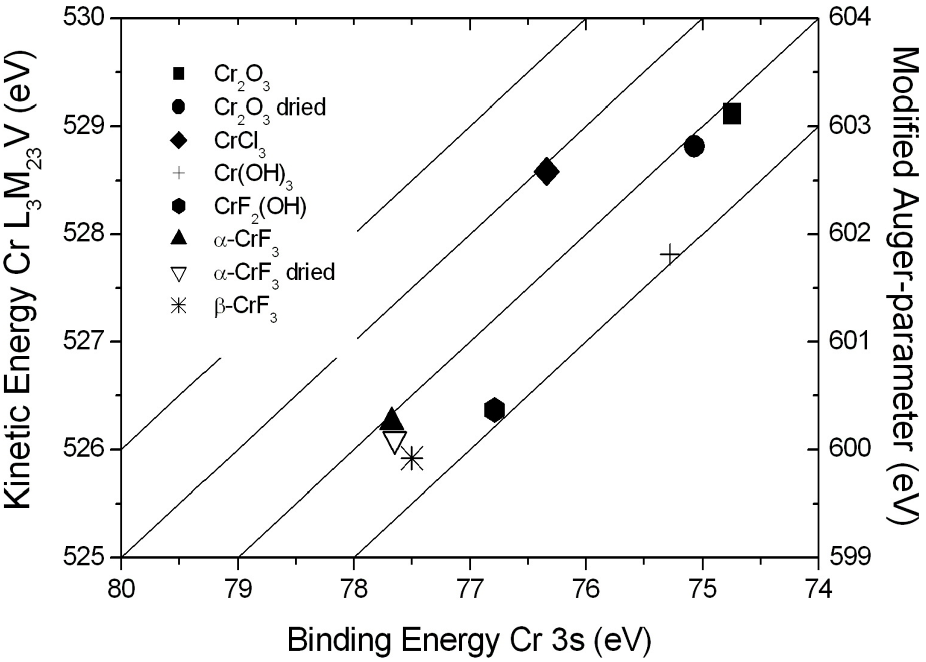

Figure 20: Chemical state plot for Cr 3s of the reference samples

and reference samples are also presented in Figures 19 and 20, respectively. The Cr 3s spectra of the chromium(III) compounds of O, F and Cl show also multiplet splitting due to the interactions between the positively ionized core hole and singly filled d orbitals. However, comparing with Cr 2p spectra they are much simpler and can be fitted using a doublet with intensity ratio of 2:1 and energy separation of 4.0 eV. The reference samples are fitted with these constraints and the BE of the higher intensity multiplet is to be taken for the chemical state plot. In the literature [88] it is reported that the Cr 3s levels for the insulators also display weak satellite features, but these features were so weak that these were not observable and therefore not considered in the spectral chemical analysis at all. For the activated samples one doublet was set with the initial parameters obtained for the Cr 3s level of Cr_2O_3 with intensity ratio of 2:1. Consequently, the Cr 3s binding energies for the Cr-O bond are plotted into the Wagner plots. Figure 19 shows clearly that the Cr 3s BE in this bond increases continuously with thermal dehydroxylation and further halogenation. This causes a higher positive charge at the metal sites, and therefore an increased Lewis acidity (also cf. Fig. 50). These results support the ones extracted from the Cr $2p_{3/2}$ chemical state plots as well.

As a result, the Cl/F exchange reactions taking place on the chromia surface causes the catalyst to be chlorinated as well as fluorinated at the surface. The electron density reduces on the metal side so that the binding energies increase at the core levels of the metal atom.

The inactive catalyst possesses highly negative fluoride ions with F 1s BE of 684.15 eV (cf. Fig. 21). As soon as the catalytic activity starts (within 2 min), the F 1s BE increases to 684.80 eV and with further reaction time the F 1s BE increases gradually. When the catalyst is activated by CCl_2F_2 at 390 $°C$ up to 24 h, F 1s BE reaches to a maximum value of 685.25 eV. Within the first 2 min the catalyst surface undergoes a dramatical change so that the BE energy increases 0.65 eV. The electron density of F relatively reduces. When the dried chromia surface, which still possesses some residual OH groups, comes to contact with the CCl_2F_2 molecule an OH/F exchange reaction takes place. So the surface will be fluorinated. Since these fluoride ions are terminally bound to the chromium sites at the surface, they are highly negative. Probably these F ions do not attend to the Cl/F exchange reaction, but with further activation time F ions start to integrate to the subsurface region. The atomic environment of the integrated F ions will be different than the terminally bound F ions. The electron density will be reduced and so the core level F 1s BE increases. Since after this stage the fluorination of the chromia takes slowly place, the F 1s BE increases slightly. The modified Auger parameters of F 1s are unchanged for the activated samples, therefore, the increase in F 1s BE can be discussed in terms of initial state effects. It is clearly seen that the activated catalysts

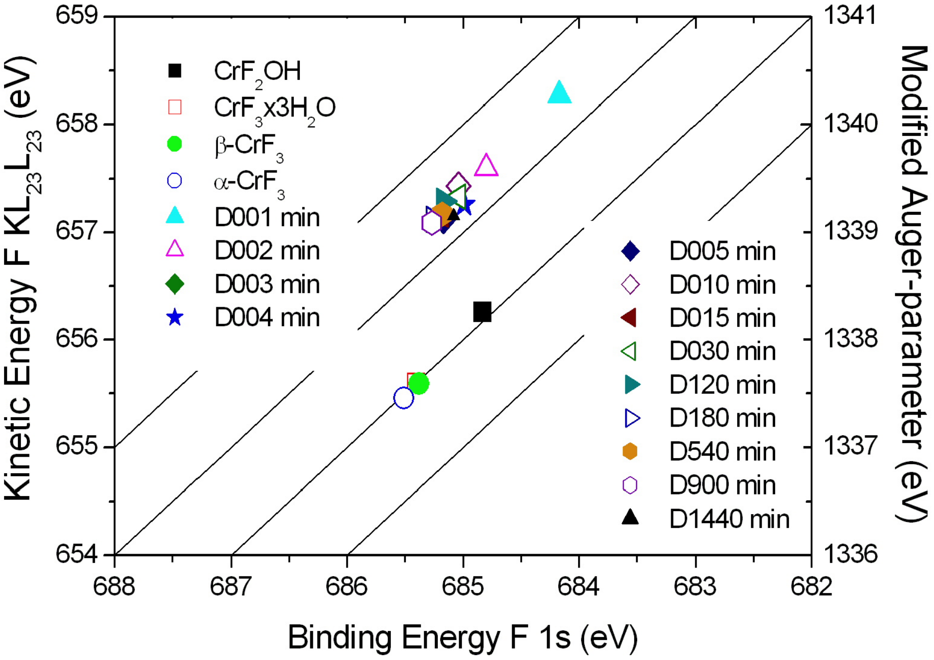

Figure 21: Chemical state plot for F 1s of Cr_2O_3 samples activated at 390 °C

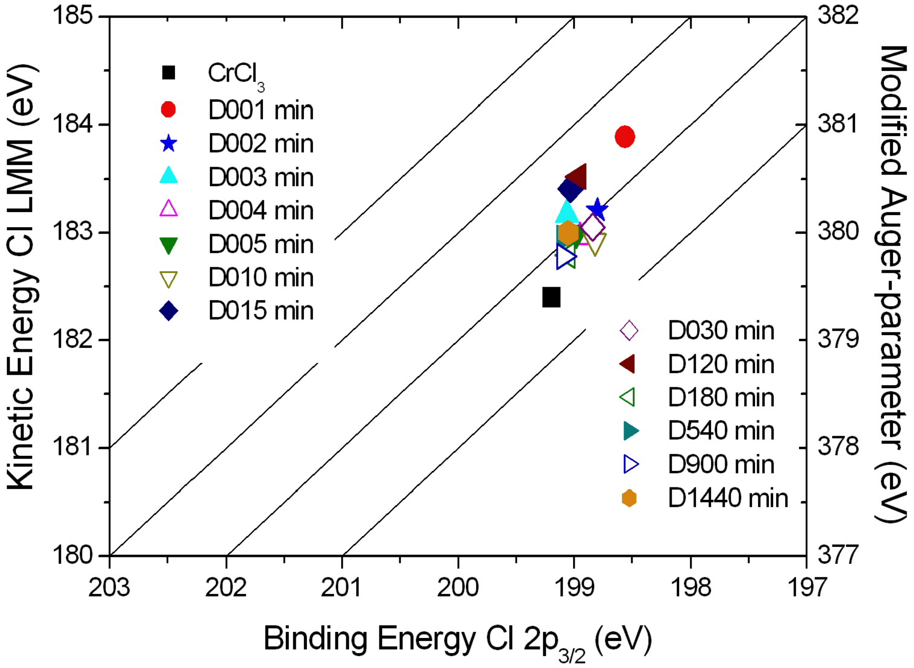

Figure 22: Chemical state plot for Cl 2p$_{3/2}$ of Cr_2O_3 samples activated at 390 °C

are very different than the $\alpha - CrF_3$, $\beta - CrF_3$, CrF_2OH and $CrF_3.H_2O$ reference samples. The active species are different than these phases.
The results presented in the chemical state plot for Cl $2p_{3/2}$ (cf. Fig. 22) can be interpreted in the similar way as was done for F 1s (cf. Fig. 21). The inactive catalyst also possesses terminally bound highly negative chloride ions with Cl $2p_{3/2}$ BE of 198.55 eV. These chloride ions are strongly bound on the surface. The Cl $2p_{3/2}$ BE increases to 198.80 eV after chlorination proceeds to the subsurface region. When the catalyst is activated by CCl_2F_2 at 390 $°C$ for 24 h, Cl $2p_{3/2}$ BE increases further to 199.05 eV. Since the modified Auger parameters of Cl $2p_{3/2}$ shift to lower values, the extra atomic relaxation energy changes and the increase in Cl $2p_{3/2}$ BE can not be discussed in terms of initial state terms. Figure 25 shows that the surface species are not totally converted to $CrCl_3$.
As a result, surface bound fluorine and chlorine suppresses the catalytic activity at the surface by masking otherwise accessible, intrinsic Lewis acid sites. The results suggest that catalytically active, strongly Lewis acidic sites are formed only after halogenation proceeds to the subsurface region of the catalyst.

.

3.3.2 Dismutation of CCl_2F_2 at 390 $°C$ "in-situ" conditions

In order to prevent the air contamination, the dismutation reaction of CCl_2F_2 at 390 $°C$ was also performed under simulated reaction conditions (cf. Fig. 51 and 52 on page 98 and 99).

After the reaction the activated chromia samples could be transferred into the XP spectrometer without exposure to air. Here, the reaction times were longer when compared with the ones in the tubular flow reactor due to the large reactor volume. The catalytic activity was followed by the product ratios which were determined by the GC analysis.

Table 4: "In-situ" XPS surface composition (atom%) of Cr_2O_3 catalysts activated with CCl_2F_2 dismutation reaction at 390 $°C$

time (h)	F	Cr	O	Cl	F+Cl	F/Cr	O/Cr	Cl/Cr	F/Cl
1	**1.5**	41.5	54.6	**2.4**	3.8	0.0	1.3	0.1	0.6
3	**4.5**	40.6	48.8	**6.1**	10.6	0.1	1.2	0.1	0.8
5	**5.2**	41.0	47.6	**6.2**	11.4	0.1	1.2	0.2	0.8
9	**6.1**	39.5	48.1	**6.4**	12.5	0.2	1.2	0.2	1.0

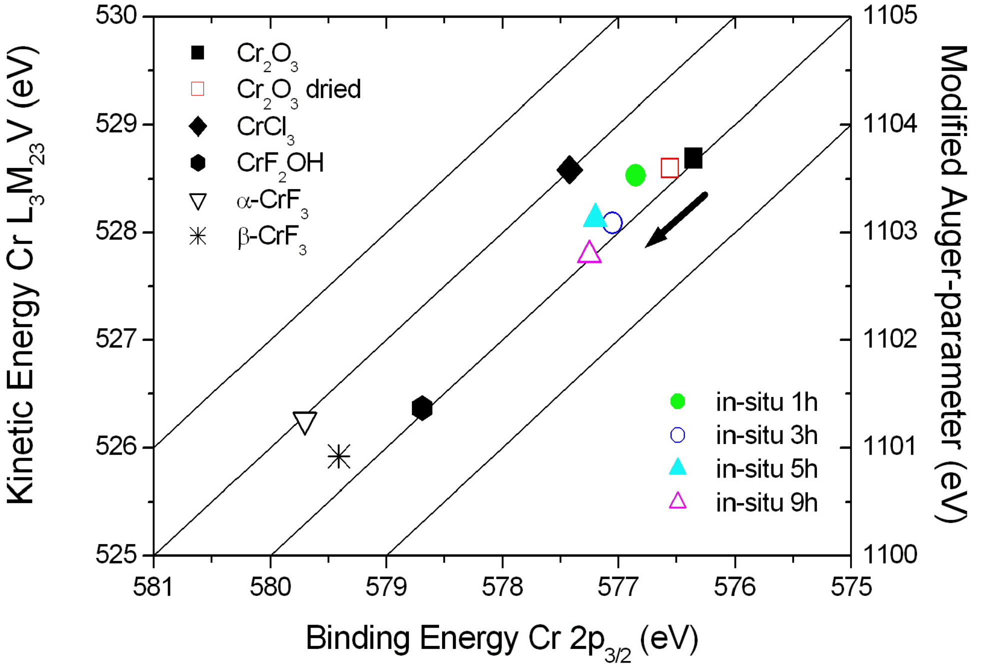

Figure 23: Chemical state plot for Cr $2p_{3/2}$ of Cr_2O_3 samples activated at 390 $°C$ ("in-situ")

Similar results are also obtained from so called "in-situ" analysis. The relative surface concentrations of F, Cr, O and Cl are given in Table 4. By drying the chromia and partial dehydroxylation the BE of Cr 2p$_{3/2}$ increases from 576.35 eV to 576.55 eV (cf. Fig. 23). After 1 h dismutation of CCl_2F_2 the catalyst is still inactive with surface composition of 1.5 atom% fluoride and 2.4 atom% chloride and the Cr 2p$_{3/2}$ BE shifts further by 0.30 eV. When the surface composition reaches to 4.5 atom% fluoride and 6.1 atom% chloride the maximum activity has achieved. Performing the reactions up to 9 h of reaction time raises the fluorine and chlorine content slightly to 6.1 and 6.4 atom%, respectively. The Cr 2p$_{3/2}$ BE increases to 577.25 eV. For all of these samples the change in the modified Auger parameter α' may be considered as insignificant so that there is no change of extra atomic relaxation energy. Considering the samples in their initial states indicates that the electron density in the metal atom is reduced by the integration of halides.

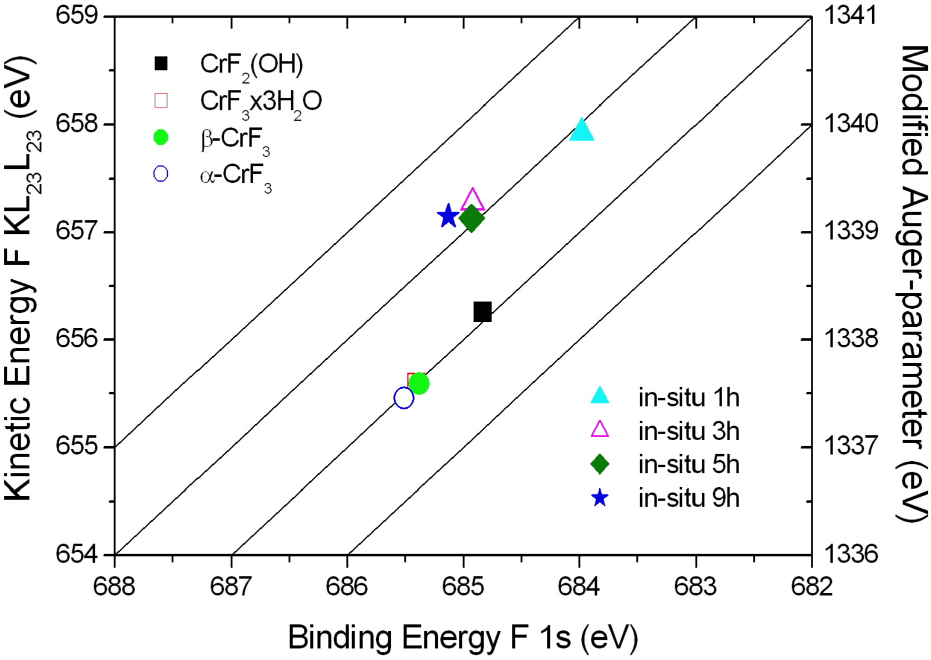

Figure 24: Chemical state plot for F 1s of Cr_2O_3 samples activated at 390 °C ("in-situ")

The chemical state plot for F 1s clearly shows the difference between the inactive and active catalysts (cf. Fig. 24). The inactive catalyst presented at the low binding energy side on the plot possesses highly negative fluoride ions that are strongly bound to the surface. Since these fluoride ions are strongly bound to the surface, they do not attend to the dismutation reaction. The activation starts then, when further fluoride ions are integrated to the subsurface region. The increase in F 1s BE indicates that the electron density is reduced at the fluoride ion by two times

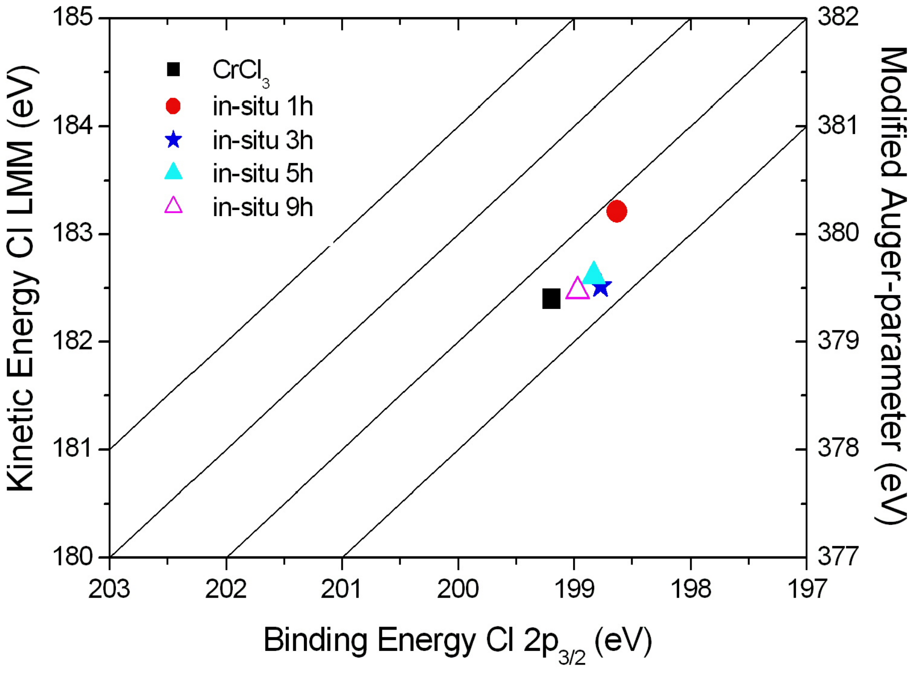

Figure 25: Chemical state plot for Cl $2p_{3/2}$ of Cr_2O_3 samples activated at 390 °C ("in-situ")

coordination (Cr-F-Cr) with the metal atoms. It is also clearly seen that the activated catalysts are very different than the reference samples.

The results presented in the chemical state plot for Cl $2p_{3/2}$ can be interpreted in the similar way as was done for F 1s (cf. Fig. 25). The inactive catalyst also possesses terminally bound highly negative chloride ions. These chloride ions are strongly bound on the surface. The Cl $2p_{3/2}$ BE increases after chlorination proceeds to the subsurface region. Figure 25 shows that the surface species are not totally converted to $CrCl_3$.

As a result, the same conclusion as was done for ex-situ XPS analysis for the activated chromia can be repeated here. The surface bound fluorine and chlorine suppresses the catalytic activity at the surface by masking otherwise accessible, intrinsic Lewis acid sites. The catalytically active, strongly Lewis acidic sites are formed only after halogenation proceeds to the subsurface region of the catalyst.

The similar results obtained by ex-situ and "in-situ" XPS analysis for activated chromia suggest that a careful sample preparation by avoiding extend exposure to air as described in Section 3.3.1 on page 41, provides reliable ESCA results.

In order to check whether a coke formation is taking place at the catalyst surface during the dismutation reaction of CCl_2F_2 the C 1s core level spectra of the "in-situ" analyzed samples are studied in detail. The total carbon concentration in the

Table 5: C 1s BE data for halogenated carbons

time (min)	C 1s BE (eV)	reference
C*-CCl	285.5	[89]
C-Cl	286.5 - 287.5	[89]
C*-CF	286.8	[90]
CF	289.0 - 289.1	[91], [90]
CF_2	290.4 - 291.3	[60], [90]
CF_3	292.5 - 293.4	[60], [90]

fresh chromia is found as 21.6 atom%. This concentration is reduced to 15.5 atom% in dried chromia. The total carbon concentration at the catalyst surface is further reduced to 11.1, 4.0, 3.0 and 5.8 atom% with activation of CCl_2F_2 for 1, 3, 5 and 9 h, respectively.

The curve fitted spectra of C 1s indicate two components at the BEs of 284.8 and $\sim$ 288.3 eV. The first one is attributed to the aliphatic carbon, C-H and the second could be due to C=O group. The relative peak areas of the C=O group according to the total C 1s signal increase from ca. 8 atom% for fresh chromia to ca. 19 atom% for 9 h activated chromia. The green color of the chromia was not changed during the activation. There is no indication for halogenated carbons in the C 1s spectra. For such carbons the C 1s BE data are presented in Table 5. As a result, coke formation at the catalyst surface is not detected.

.

3.3.3 Dismutation of CCl_2F_2 at 300 $^\circ C$ in a tubular flow reactor

In order to observe the difference between the inactive and active catalysts at lower temperatures, the dismutation of CCl_2F_2 on chromia was performed at 300 $^\circ C$. When the similar reaction is performed at 300 $^\circ C$ after drying the chromia catalyst as previously described, the activation of the catalyst starts just after 20 min of introducing the CCl_2F_2 and it continues for 25 min. During that period about 20 % of the initial feed is decomposed (cf. Fig. 28) and the DR reaches unity (cf. Fig. 27). Again higher fluorinated products and HCl are released dominantly in that time interval, because the higher fluorinated dismutation products of CCl_2F_2 are more stable than the higher chlorinated (or lower fluorinated) ones [41]. When the maximum activity is reached the conversion is ca. 60 % (cf. Fig. 26) and only the dismutation products are observed.

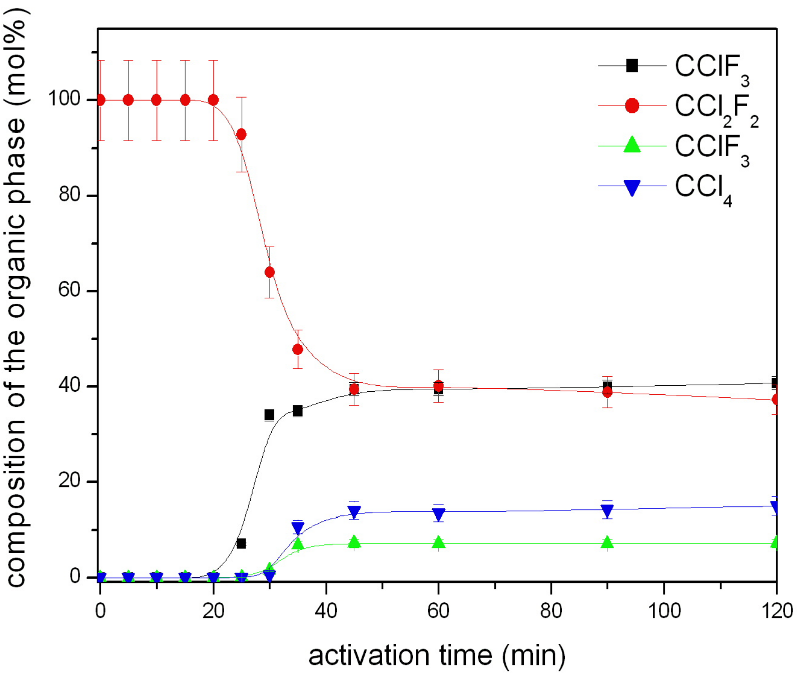

Figure 26: Cr_2O_3 catalyzed dismutation reaction of CCl_2F_2 at 300 $^\circ C$

At higher temperatures higher conversion of CCl_2F_2 to the dismutation products is obtained because the reaction equilibrium shifts to the right (cf. Eqn. 18 and 19). Therefore, at 300 $^\circ C$ lower conversion is possessed. The delay in starting the dismutation reaction can be accounted for the activation of the catalyst proceeds slower at low temperature conditions. Therefore, there is a higher time gap by reaching the catalytic activity at lower temperature conditions.

In order to better investigate the significant differences between the inactive and

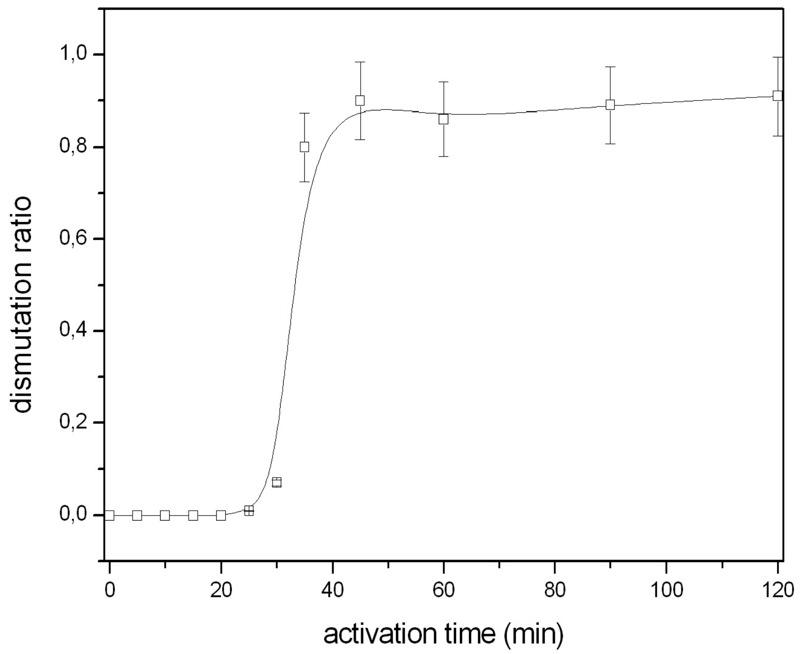

Figure 27: Dismutation Ratio (DR) for Cr_2O_3 catalyzed dismutation reaction of CCl_2F_2 at 300 °C

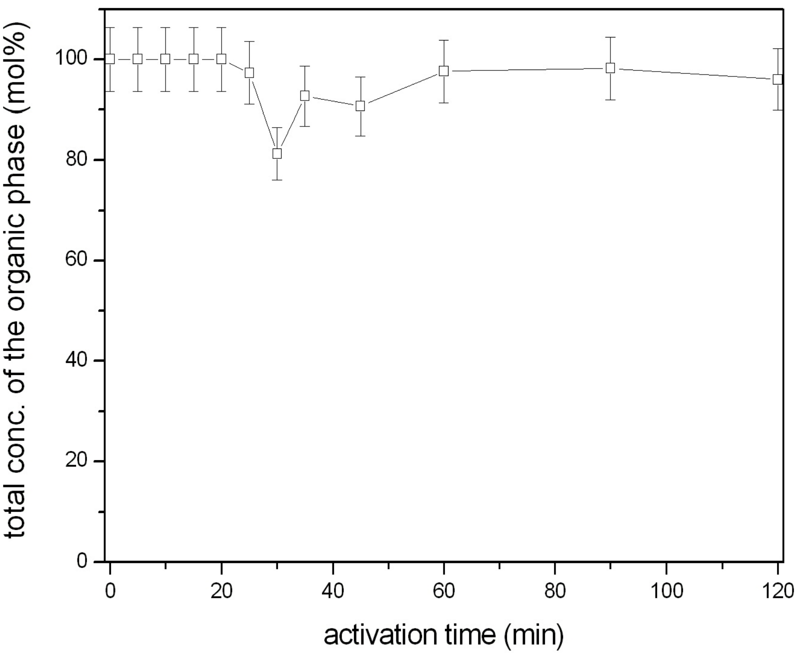

Figure 28: Total concentration of the organic phase ($CClF_3$, CCl_2F_2, CCl_3F, CCl_4) in Cr_2O_3 catalyzed dismutation reaction of CCl_2F_2 at 300 °C

active phases a number of catalyst samples are also activated with dismutation reaction of CCl_2F_2 at 300 °C for 15, 25, 30, 45 and 120 min.

Table 6: XPS surface composition (atom%) of Cr_2O_3 catalysts activated with CCl_2F_2 dismutation reaction at 300 °C

time (min)	F	Cr	O	Cl	F+Cl	F/Cr	O/Cr	Cl/Cr	F/Cl
15	**0.7**	40.4	57.6	**1.3**	2.0	0.0	1.4	0.0	0.5
25	**2.7**	36.3	58.7	**2.3**	5.0	0.1	1.6	0.1	1.1
30	**2.2**	39.2	53.9	**4.6**	6.9	0.1	1.4	0.1	0.5
45	**4.0**	38.5	52.3	**5.2**	9.2	0.1	1.4	0.1	0.8
120	**4.9**	37.4	52.1	**5.6**	10.5	0.1	1.4	0.2	0.9

The 15 min activated catalyst represents the inactive phase and the catalyst samples after 45 min of activation time are catalytically active ones. The catalysts which are activated between these two activation times are obtained during the formation process. Table 6 shows the XPS surface compositions of these catalyst samples. The inactive catalyst possesses 0.7 atom% fluorine and 1.3 atom% chlorine on the surface and the Cr 2p$_{3/2}$ BE shifts to the higher BE value by 0.38 eV when compared with the dried chromia (cf. Fig. 29). As just the maximum catalytic activity is reached at 45 min reaction time, the chromia surface is 4.0 atom% fluorinated and 5.2 atom% chlorinated. For the similar stage at the 390 °C reaction conditions the chlorination was found little more than here although the fluorine content seems to be the same. The Cr 2p$_{3/2}$ BE further increases by 0.40 eV. This was almost the same for the similar activated catalyst which just reached the maximum catalytic activity at 390 °C. So chromia requires to be halogenated in a similar way in order to reach the maximum catalytic activity for the dismutation reaction of CCl_2F_2 at 300 °C as well. After 2 h of reaction time, there is only 4.9 atom% fluorination and 5.6 atom% chlorination found on the solid surface and no significant change in the Cr 2p$_{3/2}$ BE. This means that the fluorination of the surface has increased by 22 % whereas the chlorination rises just by 8 %. Consequently, once the maximum catalytic activity is reached in the dismutation reaction of CCl_2F_2, further halogenation of the solid takes very slowly place and the fluorination proceeds relative faster than the chlorination. Since the oxygen/halogen exchange reactions are more difficult than the hydroxide/halogen exchange reactions. There is no significant change observed for the modified Auger parameter of Cr 2p$_{3/2}$ (cf. Fig. 29), therefore the increase in the Cr 2p$_{3/2}$ BE results from the initial state effects. Halogenation reduces the electron density at the metal sites.

Figure 30 and 31 show that the BEs of F 1s and Cl 2p$_{3/2}$ for the activated samples increase with reaction time. The halides at the surface of the inactive catalyst are

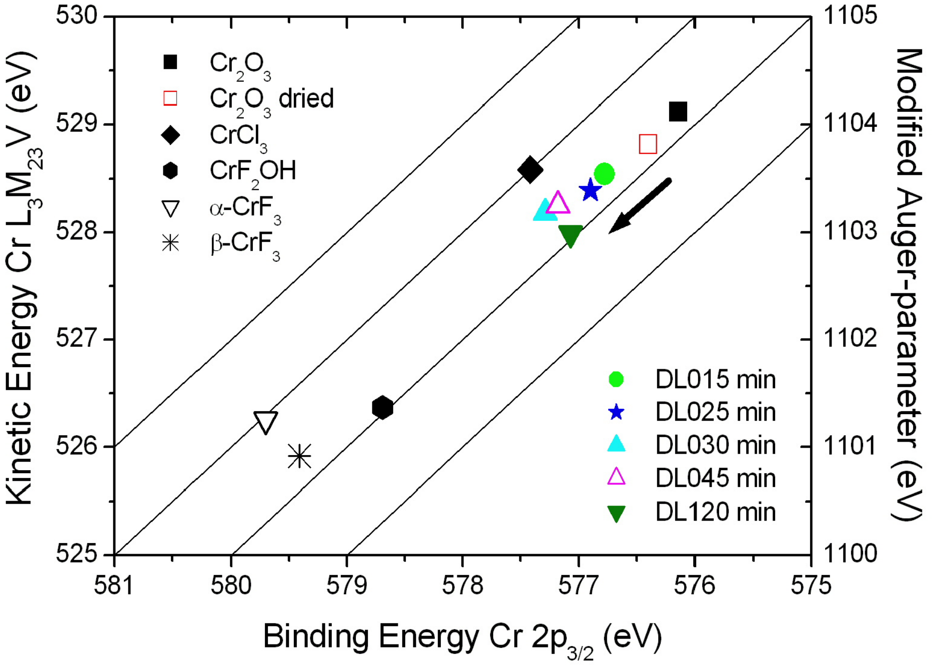

Figure 29: Chemical state plot for Cr $2p_{3/2}$ of Cr_2O_3 samples activated at 300 °C

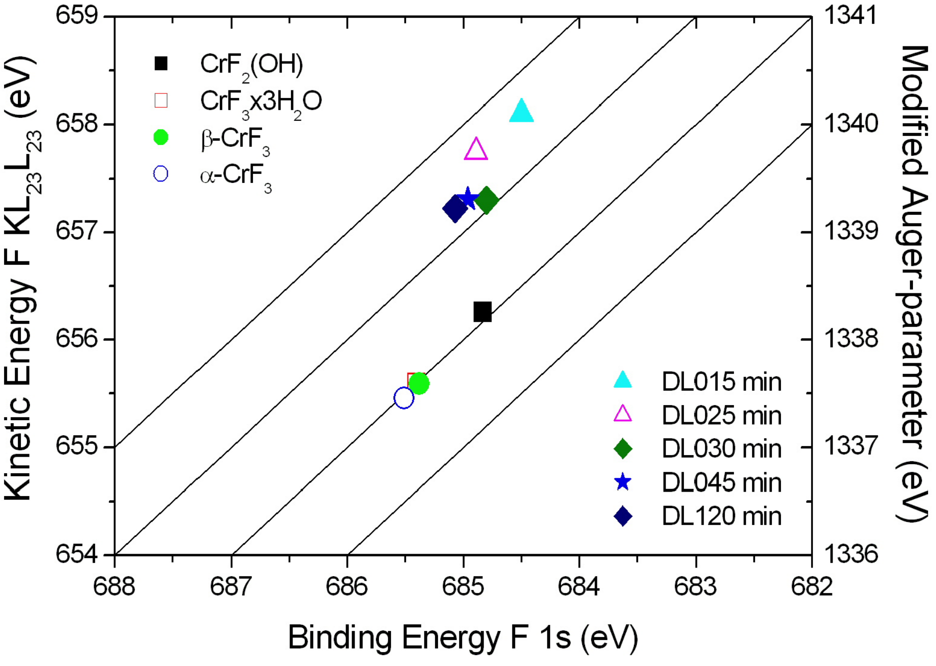

Figure 30: Chemical state plot for F 1s of Cr_2O_3 samples activated at 300 °C

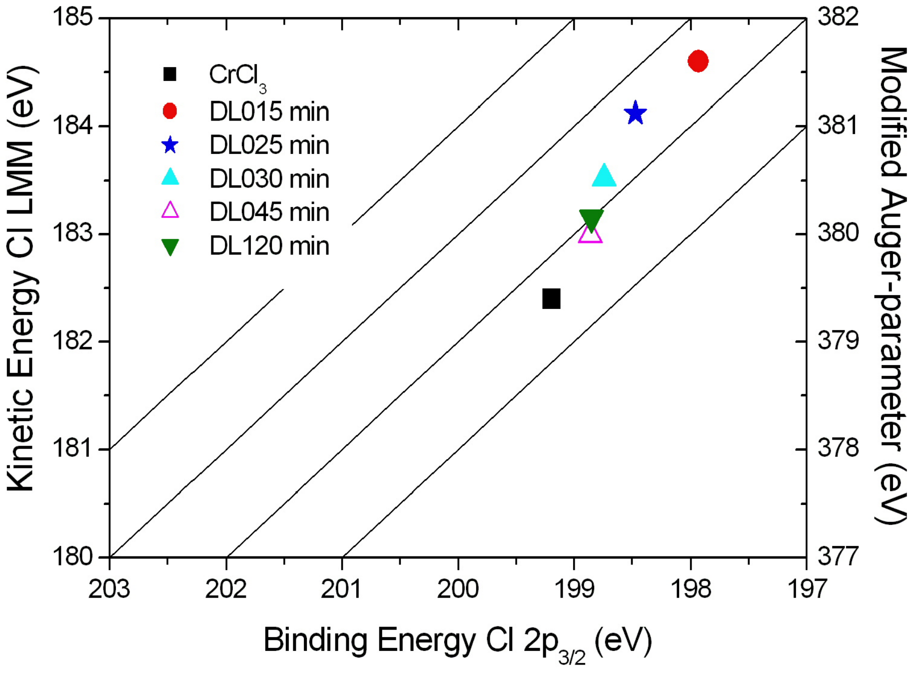

Figure 31: Chemical state plot for Cl 2p$_{3/2}$ of Cr_2O_3 samples activated at 300 °C

highly negative. In contrast, the electron charge of the halides at the surface of the active catalysts is reduced. So the terminally bound halides are differentiated from the halides which are integrated into the chromia lattice in the subsurface region. The active catalysts are different than the references $\alpha - CrF_3$, $\beta - CrF_3$, CrF_2OH, $CrF_3.H_2O$ and $CrCl_3$. Most probably the active species are chromium(III) oxide halides.

Finally, the chromia gains its catalytic activity only after halogenation has begun to proceed to the subsurface region of the sample. This process takes slower place at 300 °C when compared the one at 390 °C.

.

3.3.4 HF treatment at 390 $^\circ C$ in a tubular flow reactor

To observe the effect of HF treatment on chromia surface and whether Cr_2O_3 converts to CrF_3, the experiments tabulated in Table 7 are done.

After drying and dehydroxylation, treatment with HF causes chromia to be fluorinated as normally expected. Within 15 min 11.5 atom% fluorination takes place at the chromia surface. Further treatment with HF does not increase significantly the fluorine concentration. After 540 min HF treatment the fluorine content on the surface has reached to 13.7 atom% (cf. Tab. 7).

Table 7: XPS surface composition (atom%) of Cr_2O_3 catalysts treated with HF at 390 $^\circ C$

time (min)	F	Cr	O	F/Cr	O/Cr
15	**11.5**	41.5	47.0	0.3	1.1
60	**11.6**	41.4	47.0	0.3	1.1
180	**11.8**	42.5	45.8	0.3	1.1
540	**13.7**	40.9	45.4	0.3	1.1

It is clearly seen that the fluorination of the chromia surface takes place very fast at the beginning, the first 15 min which is also the time to reach the maximum activity in the dismutation reactions of CCl_2F_2 at 390 $^\circ C$. Then the surface reaches to a saturation point and further fluorination with HF proceeds very slowly. An explanation can be done by considering the dried and dehydroxylated chromia still possesses some residual hydroxide groups on the surface which are not easy to be removed totally from the surface at 400 $^\circ C$ and these groups undergo an exchange reaction with the fluoride ions. Moreover, some of the surface oxygen can also be substituted with the fluoride ions but this seems to a rather slow process when compared with the OH/F exchange reactions. It is interesting to note that the saturation concentration ca. 11 atom% at the chromia is equal to the total halogen concentration at the catalyst surface in the dismutation reaction of CCl_2F_2 at the same temperature. This means that the fluoride ions occupy the active centers at the chromia surface, which can be occupied by the chloride ions in a Cl/F exchange reaction, with HF treatment.

In the XPS analysis one single F 1s peak is found for all of the HF treated samples at around 685.0 eV BE (cf. Fig. 33). This means that one type of F bond is observed in the samples. In addition, the modified Auger parameter in the Cr $2p_{3/2}$ vs. Cr LMM chemical state plot (cf. Fig. 32) is not changing significantly meaning that the extra atomic relaxation energy is constant and so the shift in the binding energies can be considered in terms of initial state effects. The increasing BEs up

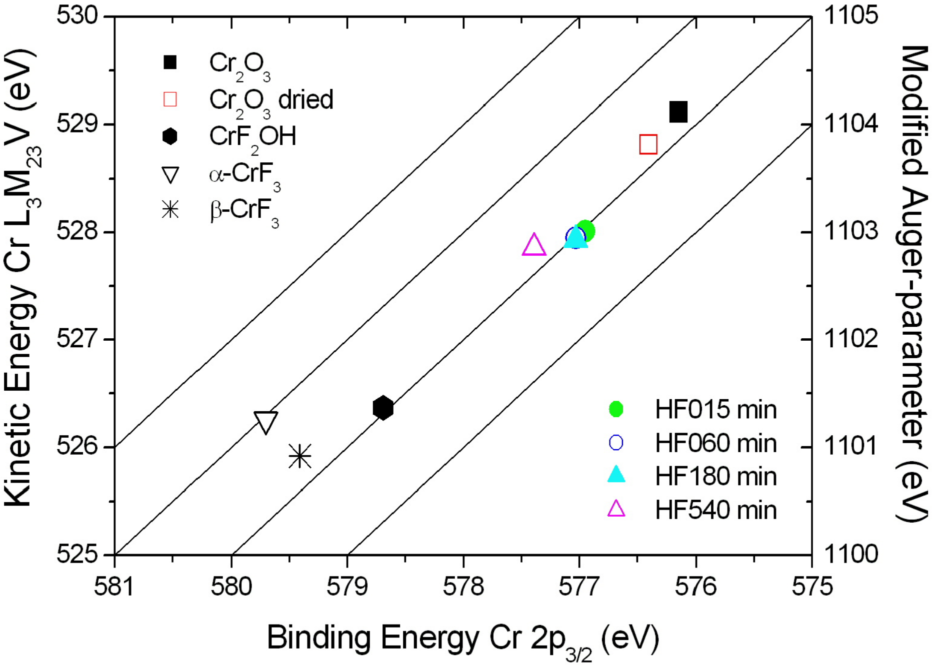

Figure 32: Chemical state plot for Cr $2p_{3/2}$ of Cr_2O_3 treated with HF at 390 $°C$

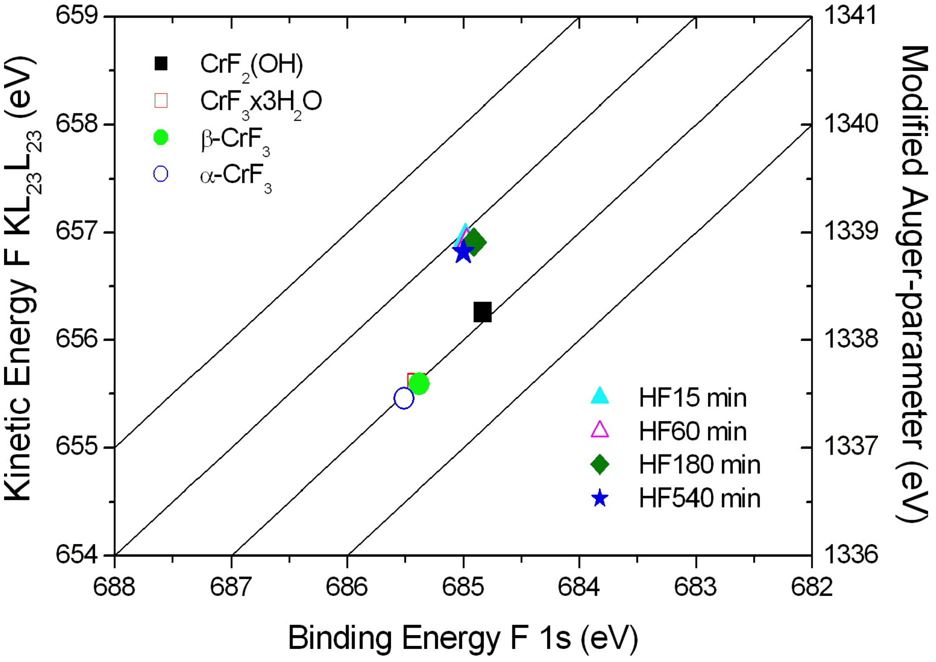

Figure 33: Chemical state plot for F 1s of Cr_2O_3 treated with HF at 390 $°C$

to 577.0 and 577.5 eV at the core level of Cr $2p_{3/2}$ reveal that the positive charge increases at the chromium site. Comparing these binding energies with the ones of the references indicates that chromium(III) oxide fluorides are formed at the surface since the Cr $2p_{3/2}$ BEs of $\alpha - CrF_3$, $\beta - CrF_3$ and CrF_2OH are far on the higher BE side and the Cr $2p_{3/2}$ BE of Cr_2O_3 is on the lower BE side.

The XPS surface composition of the 15 min HF treated sample is $CrO_{1.13}F_{0.28}$. Consequently, all of these results indicate that at the surface of chromia, after HF treatment at 390 $°C$ chromium(III) oxide fluorides are formed. HF treatment of chromia up to 540 min does not convert it to CrF_3.

3.3.5 HCl treatment at 390 °C in a tubular flow reactor

In order to find out how chromia is effected by HCl treatment and whether it will be converted to $CrCl_3$ or not, some experiments are performed.
After drying and dehydroxylation of chromia, treatment with HCl at 390 °C leads to some alterations on the chromia surface. After 15 min HCl treatment approximately 6 atom% is observed at the catalyst surface. Further chlorination also undergoes slowly and after 540 min HCl treatment ca. 8 atom% is found at the surface (cf. Tab. 8). The fluctuations in the chlorine concentrations can be accounted for the errors which result at least from the quantitative XPS analysis (cf. Sec. 2.1.6). The similar interpretation as it was done for the fluorination of chromia with HF, can be done for the chlorination of chromia with HCl. The surface OH and O is substituted by Cl ions, but this exchange process results lower halogenation at the surface when compared with the fluorination by HF. The chlorine concentration on the chromia surface by HCl treatment was found less than the fluorine concentration of HF treated chromia. However, it was almost equal to the chlorine concentration which was obtained at the chromia surface by the CCl_2F_2 activation reactions after reaching the maximum activity. This means that with HCl treatment the Cl ions do not occupy all the active centers at the chromia surface, which can be occupied by F ions in a Cl/F exchange reaction or HF treatment. This might be a reason of different ionic radii of F and Cl ions. Chloride has a larger ionic radius.

Table 8: XPS surface composition (atom%) of Cr_2O_3 catalysts treated with HCl at 390 °C

time (min)	Cr	O	Cl	O/Cr	Cl/Cr
15	42.0	51.9	**6.1**	1.2	0.1
60	42.9	51.8	**5.3**	1.2	0.1
180	42.6	53.1	**4.2**	1.2	0.1
540	40.7	51.2	**8.1**	1.3	0.2

The XPS Cl 2p spectrum could be fitted as one doublet with an intensity ratio of 2:1. This means that one type of Cl bond is observed in the samples and therefore, only a single species or phase is to be expected. For all of the Cl 2p$_{3/2}$ BEs the value of ca. 198.8 eV is found (cf. Fig. 35). Furthermore, the Cr 2p$_{3/2}$ BEs are found between 576.9 and 577.3 eV. These are higher than the BE of Cr 2p$_{3/2}$ for Cr_2O_3 but they are very close to the BE of Cr 2p$_{3/2}$ for $CrCl_3$.

The unchanged modified Auger parameter of Cr 2p$_{3/2}$ in the chemical state plot presented in Figure 34 reveals that the extra atomic relaxation energy is not changed

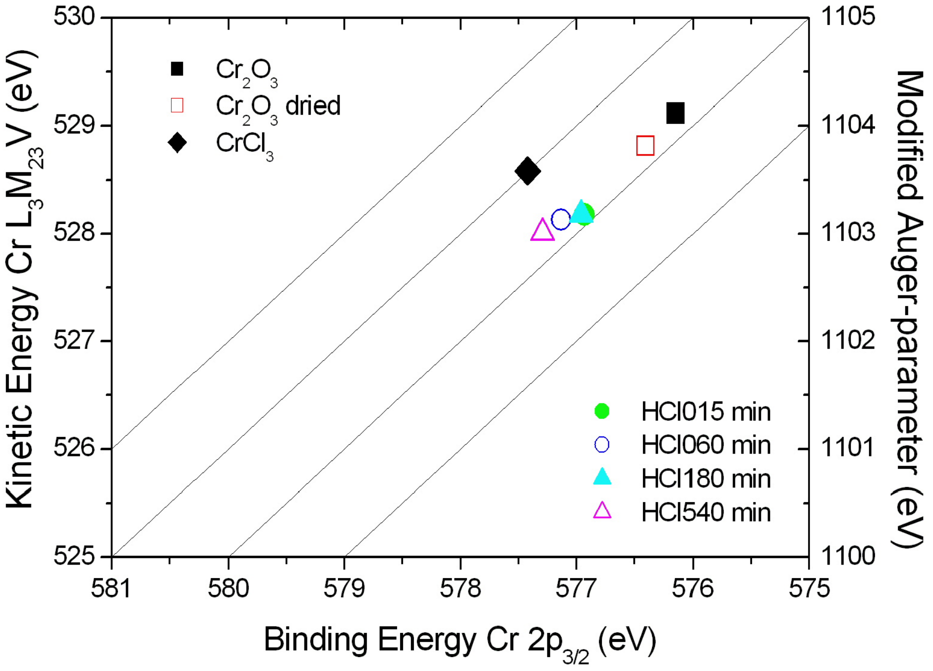

Figure 34: Chemical state plot for Cr $2p_{3/2}$ of Cr_2O_3 treated with HCl at 390 $°C$

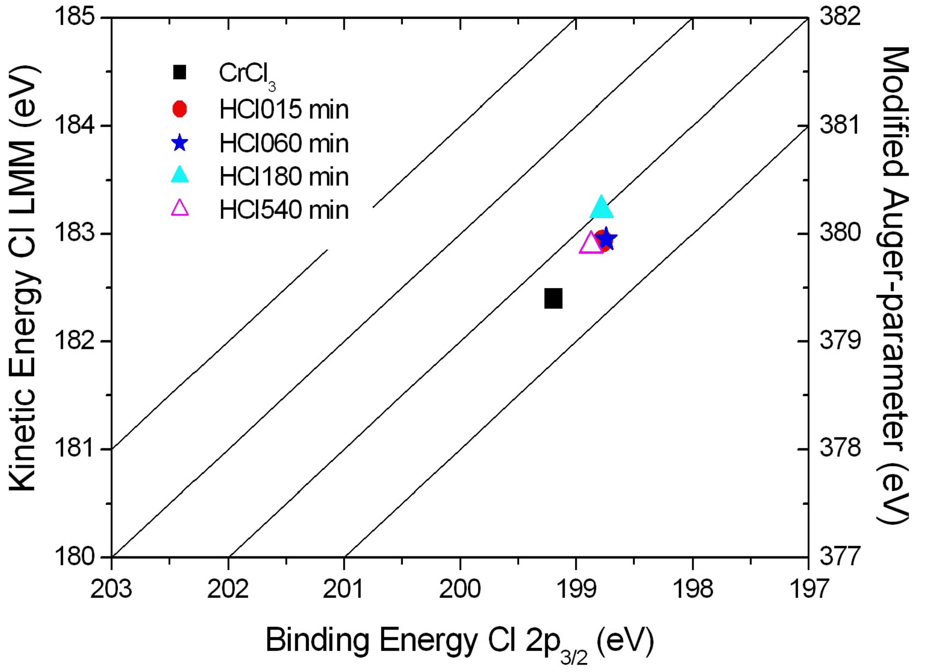

Figure 35: Chemical state plot for Cl $2p_{3/2}$ of Cr_2O_3 treated with HCl at 390 $°C$

with this treatment and the initial state effects can be considered. Although the electronegativity of Cl is slightly smaller than the electronegativity of O, due to Cl uptake the Cr 2p$_{3/2}$ BE increases. This indicates that chlorination like fluorination also decreases the electron density on the metal side and therefore the Cr 2p$_{3/2}$ BE shifts to higher BE values.

The Auger parameters of Cr 2p$_{3/2}$ for $CrCl_3$ and HCl treated samples show a gradual difference. This difference is an indication for that the treated samples are different than $CrCl_3$. The XPS surface composition of the 15 min HCl treated sample is $CrO_{1.24}Cl_{0.14}$ (cf. Sec. 10). Most probably oxide chlorides are formed with HCl treatment at 390 $^{\circ}C$ on the chromia surface.

3.3.6 Pre-halogenation before halogen treatment or dismutation of CCl_2F_2 at 390 $°C$ in a tubular flow reactor

Pre-fluorinated or pre-chlorinated chromia samples (cf. Sec. 3.3.4 and 3.3.5) are treated with HCl or HF or activated with CCl_2F_2 in order to understand the effect of pre-halogenation on chromia surfaces (cf. Tab. 9). It is important to understand if the pre-fluorination (or pre-chlorination) of the surface hinders the following chlorination (or fluorination).

Table 9: XPS surface composition (atom%) of Cr_2O_3 catalysts pre-halogenated before halogen treatment or dismutation of CCl_2F_2 at 390 $°C$

time (min)	F	Cr	O	Cl	F+Cl	F/Cr	O/Cr	Cl/Cr
15 min HF/15 min HCl	**2.3**	40.8	50.3	**6.7**	8.9	0.1	1.2	0.2
15 min HCl/15 min HF	**8.9**	41.1	48.9	**1.1**	10.0	0.2	1.2	0.0
15 min HF/60 min CCl_2F_2	**5.7**	40.1	48.8	**5.4**	11.1	0.1	1.2	0.1
15 min HCl/60 min CCl_2F_2	**4.1**	39.4	50.0	**6.5**	10.6	0.1	1.3	0.2

After pre-fluorination, the 15 min HCl treated chromia surface contains interestingly more chloride than fluoride. First with 15 min HF treatment at 390 $°C$ ca. 11 atom% fluoride is expected at the surface (cf. Sec. 3.3.4). However, the following HCl treatment replaces the fluoride on the surface and reduces the fluorine content on the chromia surface to 2.3 atom%. Besides this 6.7 atom% chlorine is found at the surface.

On the other hand, after pre-chlorination, 15 min HF treatment results with higher fluoride content on the surface. Actually with 15 min HCl treatment of chromia ca. 6 atom% Cl is expected at the surface (cf. Sec. 3.3.5). But 1.1 atom% chloride is observed with the following 15 min HF treatment at 390 $°C$ and 8.9 atom% fluoride. Obviously the HF treatment replaces the chloride ion by substitution.

These results have shown that the last halogenation replaces the first one. Both fluorination and chlorination reactions with HF and HCl on chromia surfaces are competitive with each other. This is consistent with the available thermodynamic data (cf. Eqn. 20 and 21). The Gibbs free energies are almost equal and negative for both halogenation of chromia reactions. Hence, both reactions are thermodynamically favoured and competitive with each other.

In addition, after pre-halogenation of the chromia surface with HF or HCl for 15 min at 390 $°C$, following the dismutation reaction of CCl_2F_2 at the same temperature for 60 min results with balanced fluoride and chloride surface concentrations. In other words, here similar surface concentrations are obtained such as it was obtained at the chromia surface when the maximum activity was reached with the dismutation

reaction of CCl_2F_2 (cf. Sec. 3.3.1). Such a molecule which contains equal number of fluorine and chlorine atoms is at the same time a fluorination and chlorination medium for Cr_2O_3 in Cl/F exchange reactions.
It is shown that pre-fluorination does not obstruct the following chlorination on chromia surfaces and in the similar way pre-chlorination does not hinder the following fluorination of the surface. The fluorination and chlorination reactions of chromia are competitive with each other.

3.4 XANES Analysis

The effect of the dismutation reaction of CCl_2F_2 or the HF or HCl treatment on chromia catalysts are investigated by XANES analysis. The difference between the inactive and active catalysts and the reference samples was the main interest.

In order to complement the ESCA results the XANES measurements of the references and the following samples:

(1) Cr_2O_3 activated with CCl_2F_2 at 390 $°C$ for 1 min (D1)
(2) Cr_2O_3 activated with CCl_2F_2 at 390 $°C$ for 15 min (D15)
(3) Cr_2O_3 activated with CCl_2F_2 at 390 $°C$ for 120 min (D120)
(4) Cr_2O_3 activated with CCl_2F_2 at 390 $°C$ for 1440 min (D1440)
(5) Cr_2O_3 treated with HF at 390 $°C$ for 15 min (HF15)
(6) Cr_2O_3 treated with HCl at 390 $°C$ for 15 min (HCl15)

were undertaken at Cr K-edge, Cr $L_{2,3}$-edge and F K-edge. The excitation processes involve multi-electron and multiple scattering interactions, simulation and modeling of XANES spectra is complicated (cf. Sec. 2.2). Therefore, a finger print approach is used by the interpretation of spectra.

3.4.1 Cr K-edge XANES

The XANES measurements at Cr K-edge spectra were performed in transmission mode using photons. The XANES spectra of the reference samples presented in Figure 36 differ from each other in their pre-edge and near-edge features. As the peaks in the pre-edge region represent the resonant dipole-forbidden Cr $1s \rightarrow 3d$ transition, the first peak which appears after the edge jump in the near-edge region represents the dipole-allowed Cr $1s \rightarrow 4p$ transition (cf. Fig. 6 on page 28). The peaks following this one in the near-edge region appear due to multiple scattering processes [92]. The detailed description of the features in the XANES spectra and the relation to the chemical structure of some of the references is explained by Böse et al. [93] in a previous work.

When the XANES spectra of the treated and activated samples are compared with the spectra of the references, it is seen that they look very similar to the spectra of Cr_2O_3 and very different than the spectra of other references (cf. Fig. 36, 37 and 38). This ensures that all the activated and treated samples are in Cr_2O_3 structure, because the transmission mode experiments provide information from bulk and surface, mainly from the bulk. Therefore, the chemical alterations due to the formation of new species with treatment or activation should be restricted to the very surface region of the samples. The chemical composition of the HF treated sample, which possesses the highest fluorine content undertaken in XANES analysis, is $CrO_{1.47}F_{0.06}$ (cf. Sec. 3.9). Either, Adamczyk et al. [94] could not observe any clear differences

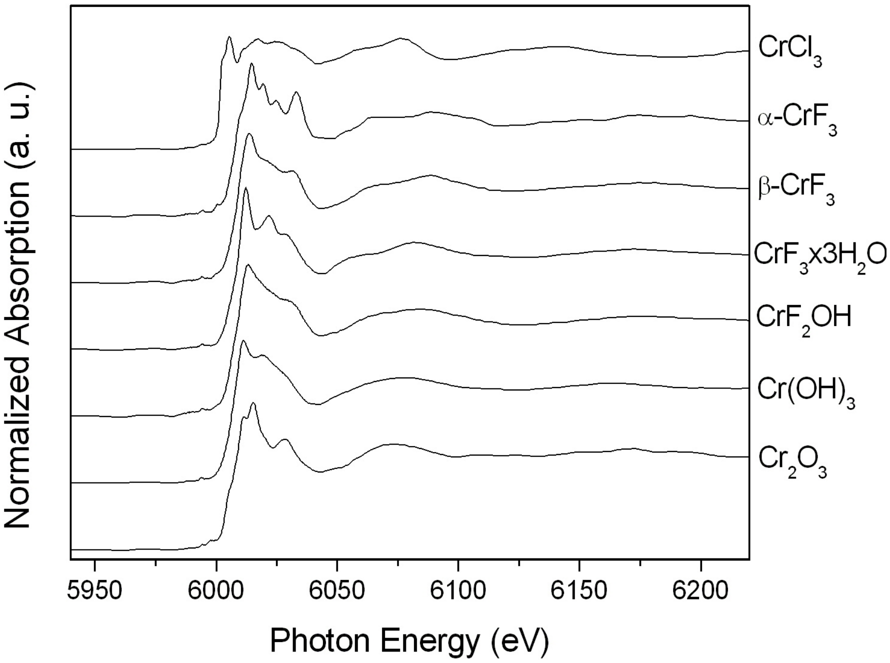

Figure 36: Cr K-edge XANES in transmission mode for reference samples

in the XANES spectra for such low fluorine containing oxide fluoride samples which were prepared by thermal decomposition of a mixture of $(NH_4)_3CrF_6/Cr_2O_3$.

In order to probe the effect of treatment or activation, the difference of spectra of these samples with the spectrum of Cr_2O_3 was evaluated. Figure 39 represents subtle differences between the spectra of the treated or activated samples and the spectrum of Cr_2O_3 at approximately 6000 to 6020 eV photon energy. These differences must originate from the surface region of the samples. All samples show differences in this photon energy range but the HCl treated sample has the smallest difference. All other samples indicate relatively stronger differences most probably due to fluorination because none of them contain more chlorine than the HCl treated one. Although these spectra of samples differ from untreated Cr_2O_3, they do not indicate any difference between the active and inactive samples and all have similar type structures.

Cr K-edge XANES analysis showed that the halogenated chromia species are distinct from the CrF_3, $CrCl_3$ and CrF_2OH phases and they are formed at the very surface of the catalyst.

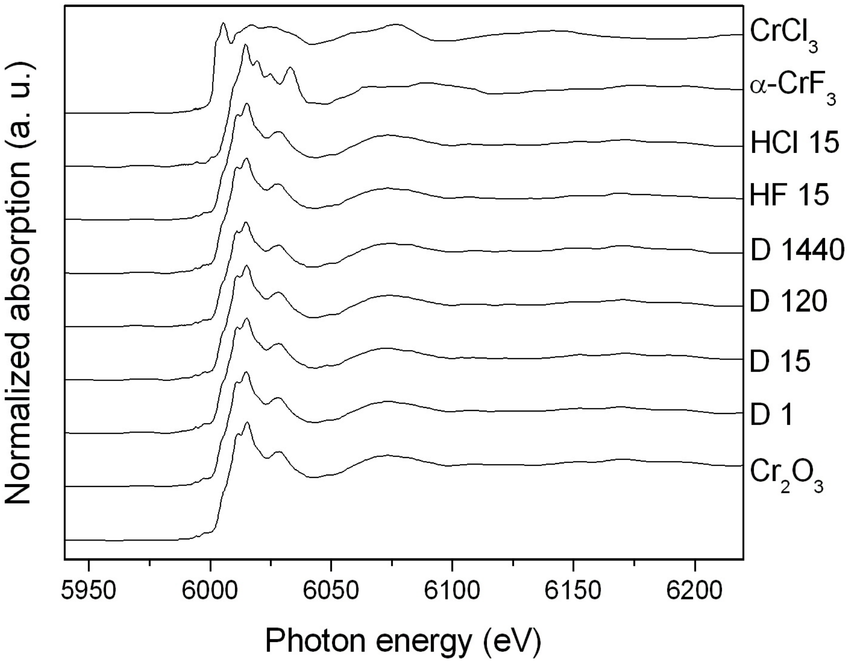

Figure 37: Cr K-edge XANES spectra of activated Cr_2O_3 samples compared to the spectra of Cr_2O_3, CrF_3 and $CrCl_3$

3.4.2 Cr $L_{2,3}$-edge XANES

The XANES measurements at Cr $L_{2,3}$-edge spectra were performed in total electron yield (TEY) mode. The spectra of the references and treated or activated samples are presented in Figure 40. The Cr $L_{2,3}$-edges in CrF_3's are shifted to higher energies when compared with the Cr $L_{2,3}$-edges in Cr_2O_3. This is a result of higher electronegativity of fluorine, which attracts the electrons more than the oxygen. This causes the chromium atom to be more polarized so that the core level electrons are shifted to higher binding energies.

Since the electronegativity of chlorine is less than the electronegativity of oxygen, the Cr $L_{2,3}$-edges in $CrCl_3$ are shifted to lower energies. However, the activated or treated samples do not show any energy shift due to the substitution of oxygen with halogen. On the other hand, the intensities of the resonants at L_2 and L_3-edges slightly increase with increasing activation time or fluorine concentration. The higher electronegativity of F reduces the electron density at the Cr atom, and therefore, the transition of the 2p electrons to the unfilled 3d orbitals will be relatively favoured resulting in an increase in the intensities at these resonants. These results are in good agreement with the ones reported by Adamczyk [95].

The Cr $L_{2,3}$-edge TEY-XANES analysis support the idea that the species formed

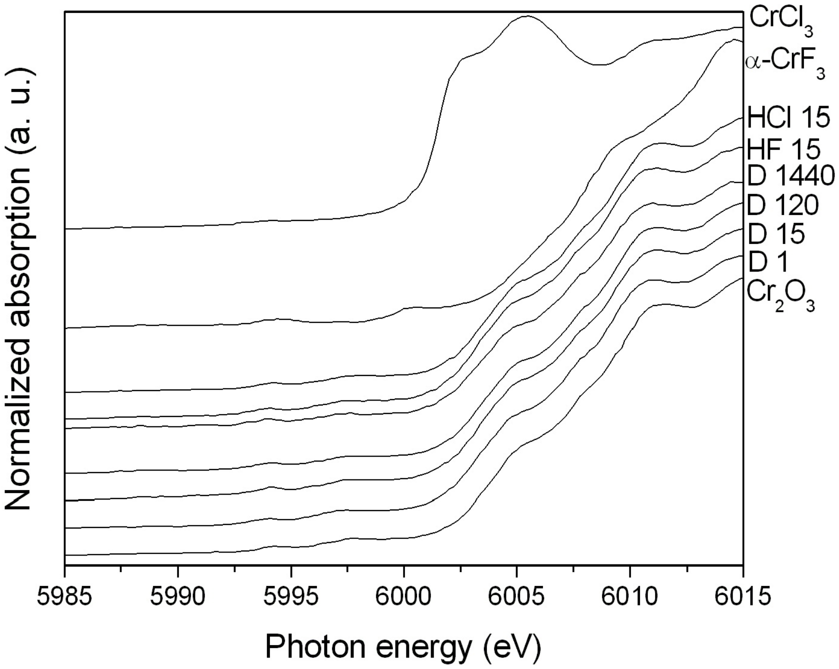

Figure 38: Pre-edge structure of Cr K-edge XANES spectra of activated Cr_2O_3 samples compared to the spectra of Cr_2O_3, CrF_3 and $CrCl_3$

at the chromia surface due to activation by CCl_2F_2 or HF treatment, are different than the reference samples. Consequently, chromium oxide halides are formed at the very surface.

3.4.3 F K-edge XANES

The TEY-XANES F K-edge spectra of the treated and activated samples, except the one with low degree of fluorination, slightly resemble the main features of the spectra of the reference samples $\alpha - CrF_3$, $\beta - CrF_3$, CrF_2OH and $CrF_3.H_2O$ (cf. Fig. 41). It is seen that the broad resonance located at about 695 eV appears somewhat narrower and less structured and the noise to signal ratio is higher when compared with the F K-edge spectra of the references. This is a result of lower fluorine content in the samples. Since in the TEY-XANES experiment the information is gained from a depth of approximately 40 Å [96], the near surface region contains less fluorine than the references. This means that oxide fluorides or oxide halides are formed in the surface region of the samples.

Interestingly, however, a very different F K-edge spectrum was observed for the sample with a very low degree of fluorination. A similar spectrum was also obtained by Adamczyk et al. [94] for low fluorine content chromium oxide fluorides. They

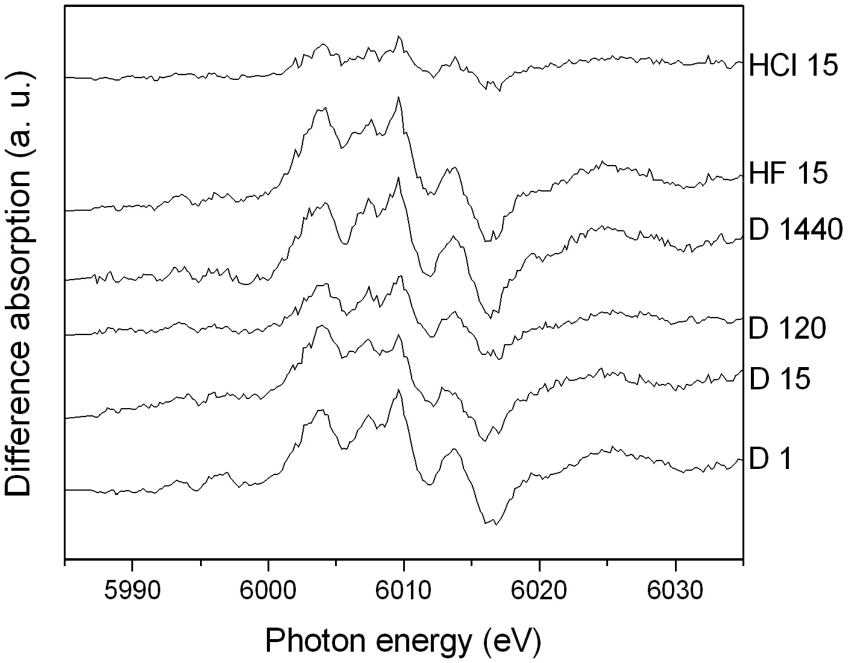

Figure 39: Cr K-edge XANES difference spectra of treated or activated Cr_2O_3 samples. The spectrum of Cr_2O_3 is subtracted from the spectra of the samples

concluded that the chromium oxide lattice is able to tolerate fluorine incorporation at low percentages without strong consequences for its own structure. Incorporation might occur at surface sites, at defects, in grain boundaries or interstitial subsurface and lattice sites. Moreover, Davis et al. [97] reported that a dopant level of 1 wt% fluorine can be incorporated in the γ-Al_2O_3 without strongly disturbing the lattice from F K-edge EXAFS analysis.

The 1 min activated chromia, which is the inactive catalyst, possesses 0.2 wt% fluorine determined by the wet chemical analysis. The quantitative XPS analysis reveals 1.6 atom% fluorine for this inactive catalyst (cf. Sec. 3.9). The fluoride ions in this catalyst are terminally bound to the chromium atoms, which are presented at the surface, without disturbing the lattice. Therefore, a very different F K-edge spectrum was observed. With further activation time the catalyst became active and the XANES spectra with main features indicating CrF_3 was obtained. Hence, when the fluorination integrates to the subsurface region the catalyst becomes active.

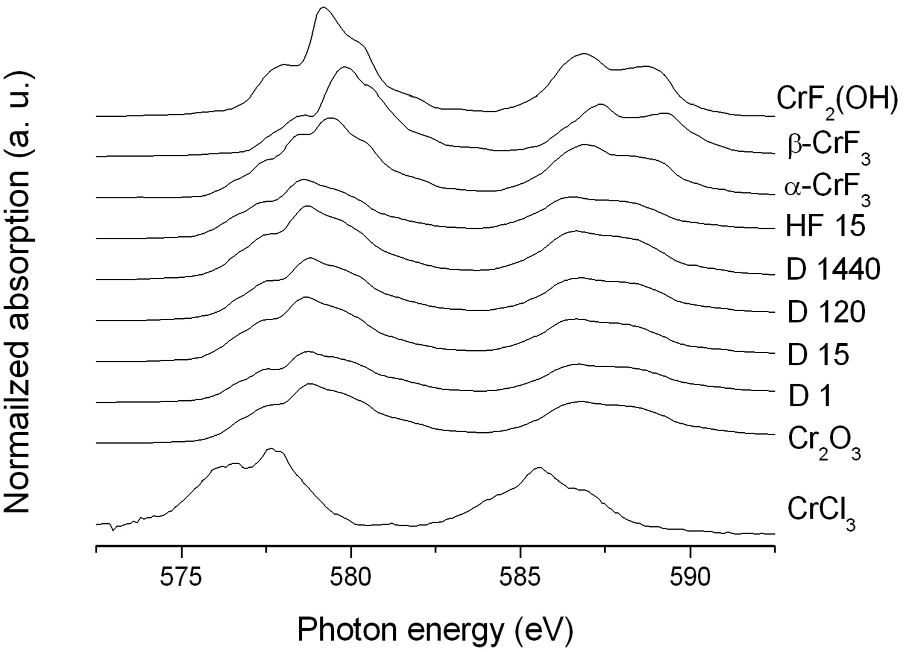

Figure 40: Cr L$_{2,3}$-edge XANES spectra of activated Cr_2O_3 samples compared to the spectra of references

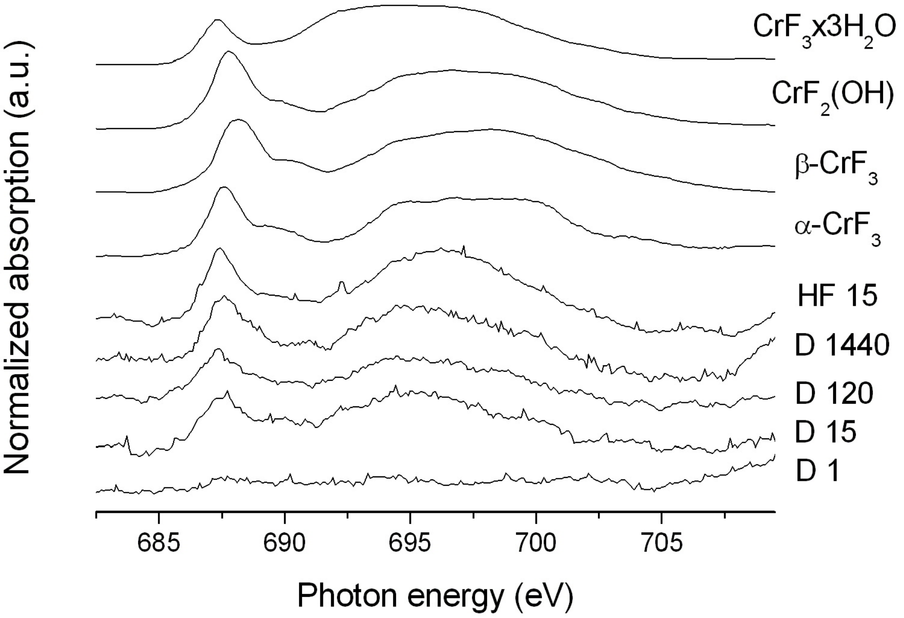

Figure 41: F K-edge XANES spectra of activated Cr_2O_3 samples compared to the spectra of $\alpha - CrF_3$, $\beta - CrF_3$, CrF_2OH and $CrF_3.H_2O$

3.5 ToF-SIMS Analysis

ToF-SIMS is a very surface sensitive technique. The upper most monolayers can be investigated by ToF-SIMS analysis. The solid surface is bombarded with primary ions, which preferably Ar^+, Xe^+, Cs^+, Ga^+ or In^+ are used for. The primary ions loose their energy and impulse due to elastic and inelastic collisions with the surface atoms and molecules. Further collisions cause a cascade process. The static SIMS is a technique of a potential importance in surface science. When a high energy beam of ions or neutrals bombards a surface, the particle energy is transferred to the atoms of the solid by billiard-ball type collisional process. A cascade of collisions occurs between the atoms in the solid; some collisions return to the surface and result in the emission of atoms and atom clusters, some of which are ionized in the course of leaving the surface. Consequently, the bombarded surface atoms or molecules can leave the surface when their energies are higher than their surface binding energies. The emitted "secondary" particles will be electrons, neutrals species atoms or molecules, atomic and cluster ions. The vast majority of species emitted are neutral but the secondary ions are detected and analyzed by the mass spectrometer. The secondary ion yield is strongly affected from a matrix effect.

ToF-SIMS analysis can be performed in dynamic or static mode. In dynamic SIMS with high current of primary ions elemental depth profile analysis is achieved. By static SIMS the primary ion currents and conditions are so adjusted that the secondary ions are only collected from undamaged parts of the surface. While the SIMS technique is apparently destructive, the essence of the static mode is to use an extremely low dose of primary ions, never more than 10^{13} ions cm^{-2}, such that within the time scale of the experiment very much less than 1 % of the top surface layer of atoms or molecules receives an ion impact. Under these conditions on a random impact basis no spot on the surface should receive more than one primary ion strike. The species generated arise from an area no greater than 10 nm^2 and are remote from the next point of analytical impact. The vast majority of the surface will be unaware of the removal of these species or any local effects as a consequence of the sputtering event. Thus the spectral information arises from a surface which is, for all practical purpose, undamaged [98].

The final collision resulting in secondary particle emission is of low energy ($\sim$ 20 eV); over 95 % of the secondary particles originate from the top two layers of the solid. Thus the possibility of a soft ionization mass spectrometry of the surface layer emerges. Therefore, a relationship between SSIMS spectra and surface chemistry is found, when static analysis conditions are used.

Because of its high transmission capability, the time-of-flight-mass-analyzer is able to detect even small concentrations of constituents with a good signal to noise ratio. Mass resolution is about $10^3 - 10^4$ up to mass number of 100 amu. In the analyzer all particles are accelerated with a potential difference. The time required to take a certain path is related to the mass number.

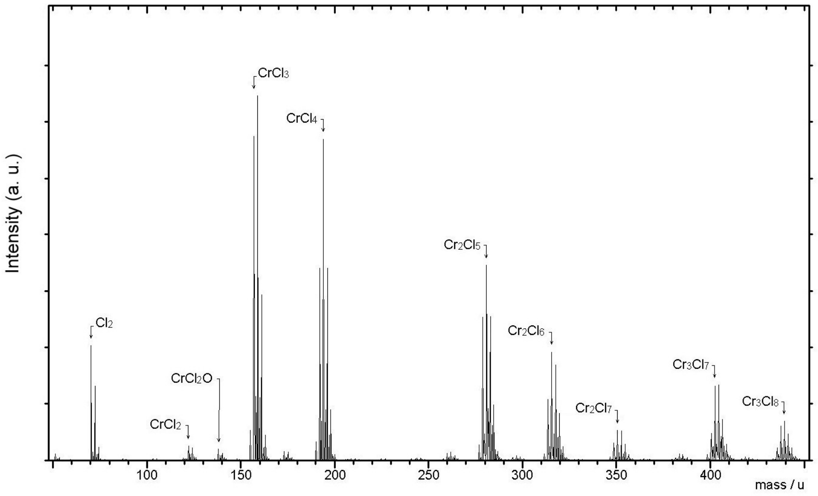

Figure 42: Negative ToF-SIM Spectrum of $CrCl_3$

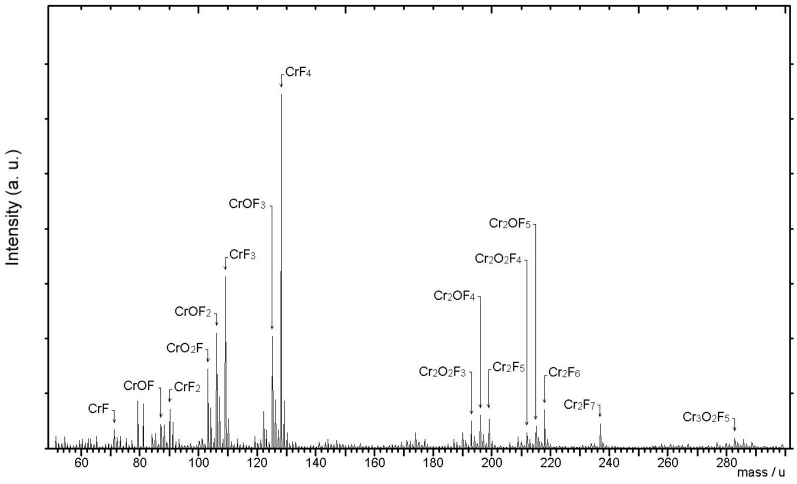

Figure 43: Negative ToF-SIM Spectrum of CrF_3

The static SIMS spectra of Cr_2O_3, $\alpha - CrF_3$, $CrCl_3$ and Cr_2O_3 samples activated with CCl_2F_2 at 390 $°C$ for 1 and 120 min are investigated ex-situ by a time-of-flight secondary-ion mass spectrometer.

The XRD, ESCA, and XANES analyses for the activated Cr_2O_3 samples do not show any indication for separate phases. Most probably oxide-halides are formed at the surface. If this is really the case, one expects to detect chromium oxide-halide fragments. However, this alone might not be enough to support the hypothesis

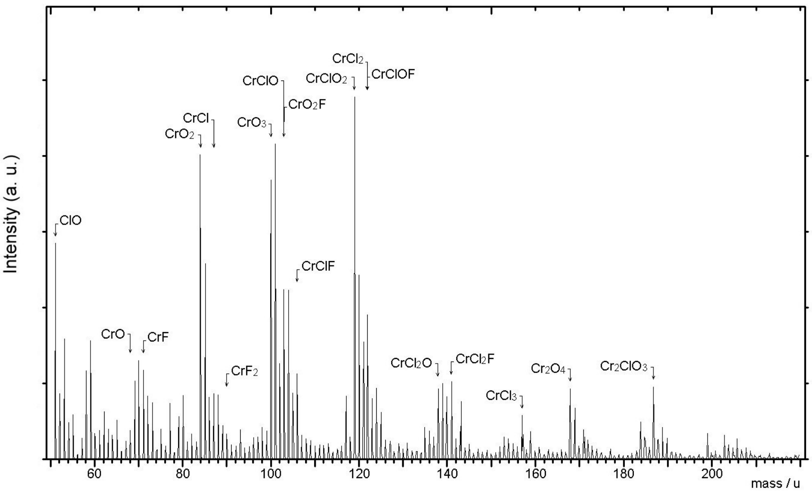

Figure 44: Negative ToF-SIM Spectrum of Cr_2O_3 activated with CCl_2F_2 at 390 °C for 1 min

that there are no separate phases. The strong evidence will be produced when the ToF-SIM spectra of the activated samples do not contain such fragments which are observed just in the spectra of the reference samples $\alpha - CrF_3$ and $CrCl_3$.

Cr_2O_3, CrF_3 and $CrCl_3$ have octahedral structures, where the centered chromium atom is six times coordinated with the surrounding ligands. Therefore, CrX_6^- (X = O, F or Cl) fragments should be characteristic for the reference samples, if they are detectable in ToF-SIMS at all. Neither CrX_5^- nor CrX_6^- fragments were detected for the reference samples. Moreover, CrO_4^- was not detected either. This can be explained by thinking such fragments can be emitted from the surface neutral or ionized but do not exist for a long period and they decompose or rearrange before they are detected. In other words, the existing probability of such ionized fragments is small. CrO_4^-, CrO_5^- and CrO_6^- fragments from clean Cr_2O_3 surfaces are not observed also in literature work [99], [100]. The CrO_3^- fragment is reported to be the most intense peak in the negative ToF-SIM spectrum of Cr_2O_3.

The comparison of the ToF-SIM spectra of the activated and reference samples show significant differences. First of all the reference $\alpha - CrF_3$ and $CrCl_3$ samples show in their negative ion spectra CrX^-, CrX_2^-, CrX_3^- and CrX_4^- (X = F or Cl) fragments (cf. Fig. 42 and 43). However the both activated samples do not show any CrX_4^- fragments, although the other fragments are seen (cf. Fig. 44 and 45). This can be an indication for that some of the oxygen atoms on the upper most layer are exchanged with F and Cl atoms during the activation process leading to oxide-halide structures. In other words, the oxygen atoms in the first monolayer are not totally

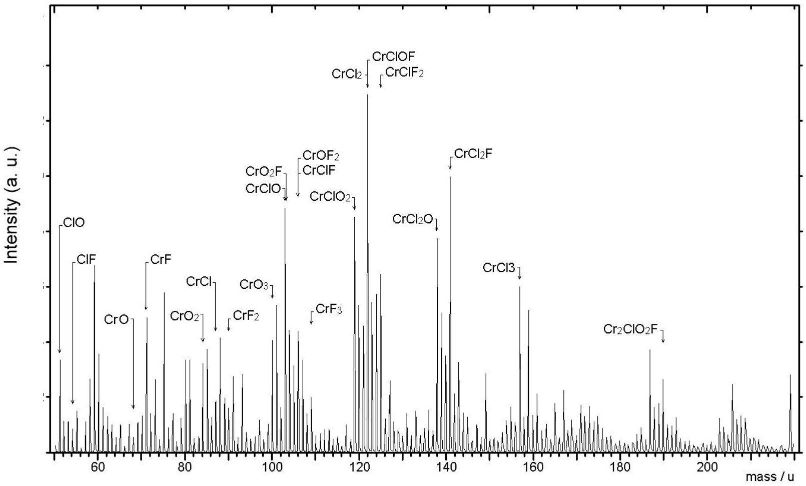

Figure 45: Negative ToF-SIM Spectrum of Cr_2O_3 activated with CCl_2F_2 at 390 °C for 120 min

substituted by the halogens and no separate CrF_3 and $CrCl_3$ phases are formed and therefore CrF_4^- and CrCl_4^- fragments are not observed. In addition, clusters like $Cr_2Cl_5^-$, $Cr_2Cl_6^-$, $Cr_2Cl_7^-$, $Cr_3Cl_7^-$ and $Cr_3Cl_8^-$ are detected in the negative ToF-SIM spectrum of $CrCl_3$ but not in the spectra of the activated samples. In the same way, $Cr_2F_5^-$, $Cr_2F_6^-$ and $Cr_2F_7^-$ clusters are detected in the negative ToF-SIM spectrum of CrF_3 but not in the spectra of the activated samples. On the other hand, fragments like $CrClOF^-$, $CrClF_2^-$, $CrCl_2F^-$ and $Cr_2ClO_2F^-$ are only observed in the spectra of the activated samples. These fragments indicate that at the solid surface chloride and fluoride ions are directly connected to the chromium atom and chromium oxide-halides are formed.

The existence of the CrO_3^- fragment in the spectra of activated samples and reference Cr_2O_3 can be interpreted that the activated samples on the upper most surface layer might be still possessing regions or parts characteristic to Cr_2O_3. Consequently, the intensity of the CrO_3^- fragment decreases with increasing reaction time (cf. Fig. 44 and 45).

3.6 SEM Analysis

The SEM analysis are performed in order to find out how the morphology of the starting material, Cr_2O_3, changes with activation or halogen treatment.

Scanning electron microscopy (SEM) is carried out by rastering a narrow electron beam over the surface and detecting the yield of either secondary or backscattered electrons as a function of the position of the primary beam. Contrast is caused by the orientation, parts of the surface facing the detector appearing brighter than parts of the surface with their normal pointing away from the detector. The secondary electrons have mostly low energies in the approximate range 5 - 50 eV and originate from the surface region of the sample. Backscattered electrons come from deeper regions and carry information on the composition of the sample. SEM sees contrast due to the topology and composition of the sample. Therefore, the interaction of the primary beam with the sample provides a wealth of information on morphology, crystallography and chemical composition [101].

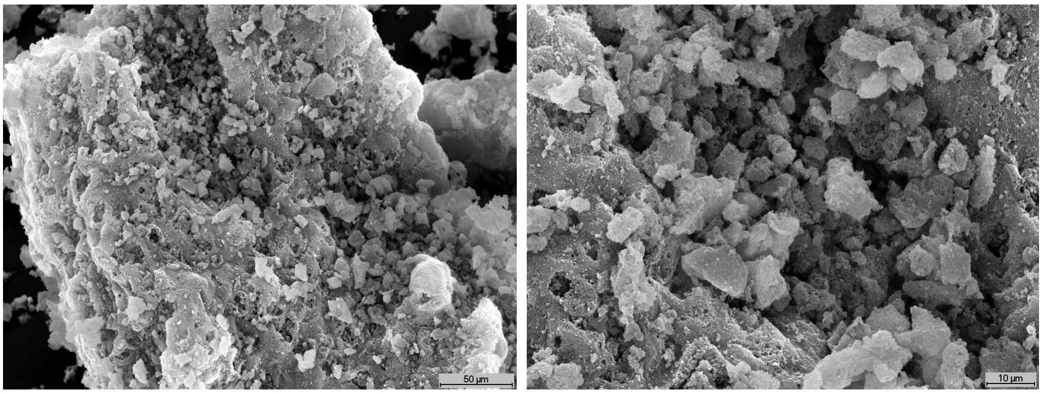

Figure 46: SEM images of Cr_2O_3 that is the starting material for activation or HF treatment

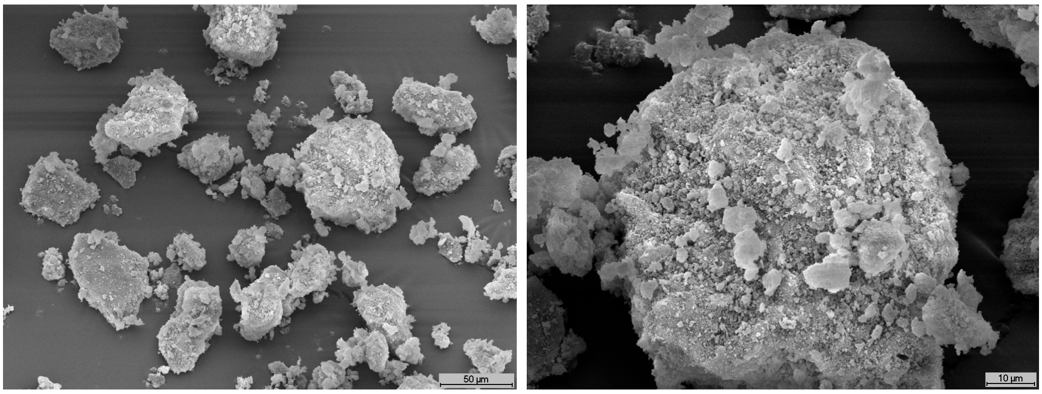

Figure 47: SEM images of Cr_2O_3 activated with CCl_2F_2 for 24 h at 390 °C

The reference Cr_2O_3 and the Cr_2O_3 activated with CCl_2F_2 for 24 h at 390 °C and

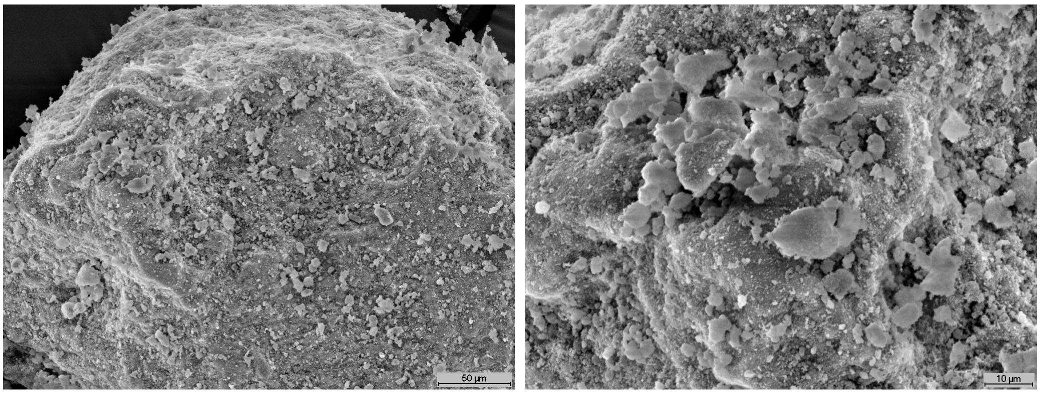

Figure 48: SEM images of Cr_2O_3 treated with HF for 15 min at 390 °C

Cr_2O_3 treated with HF for 15 min at 390 °C are investigated by SEM to find out a difference in their morphology. Although halogenation takes place on the Cr_2O_3 surface with activation or HF treatment, no clear difference is observed in their SEM images (cf. Fig. 47 and 48) when compared with the SEM images (cf. Fig. 46) of the reference Cr_2O_3. Most probably activation or treatment processes cause halogenation at the very surface.

3.7 Fluorine Solid State NMR Analysis

The fluorine solid state NMR analysis is done to observe the chemical shifts for fluoride ions with different properties. The idea is that $\alpha - CrF_3$, Cr_2O_3 treated with HF and Cr_2O_3 activated with CCl_2F_2 have fluoride ions with different properties. The chromium atom is coordinated only by fluoride ions in $\alpha - CrF_3$, it is coordinated by oxygen and fluoride ions in HF treated Cr_2O_3 and it is coordinated by oxygen, chloride and fluoride ions in Cr_2O_3 activated by CCl_2F_2. The fluoride ion bound to chromium which is differently surrounded, should be differently polarized and this effect could be observable by NMR. In addition, already known from ESCA results that the inactive and active chromia catalysts, which are halogenated in the dismutation reaction of rab, possess fluoride and chloride ions with different effective charges. At the beginning of the activation of chromia the halides at the surface are highly negative, whereas after the catalyst became active by the integration of the halides into the subsurface region relatively less negative halides are found. It is also expected to observe this difference by the NMR analysis.

$\alpha - CrF_3$, Cr_2O_3 treated with HF at 390 $°C$ for 15 min and samples of Cr_2O_3 activated with CCl_2F_2 at 390 $°C$ for 2 min and 15 h, are investigated by solid state NMR Analysis.

Chromium fluorides were not subject of fluorine NMR investigations in the past. Only few papers reporting ^{19}F-NMR investigations of Cr-F compounds can be found in the literature [102]. Because of the influence of the three unpaired electrons in chromium(III), rather broad, featureless F resonance signals are observed in solid state NMR and failed to yield useful information.

Generally, paramagnetic compounds are not suitable materials for NMR studies. The dipolar interaction of a single electron with a special nucleus, observed in the NMR experiment, is extremely strong and makes therefore extreme line broadening. It is a well known fact that line broadening in Magic Angle Spinning (MAS)-NMR experiments is reduced by fast spinning of the sample. Sophisticated techniques nowadays allow realizing spinning speeds up to 35 kHz with surprising results concerning line width [103].

Under these circumstances first acceptable MAS-NMR results were obtained in some cases. A chromium oxofluoride, CrOF, obtained by thermal decomposition of a mixture of $(NH_4)_3CrF_6/Cr_2O_3$ and well characterized by various techniques [94] was investigated by ^{19}F -MAS-NMR. The chemical shift of the relatively narrow peak is at -132 ppm. This is obviously the chemical shift range where chromium(III) fluorides resonate. The spectrum was monitored at 12 kHz rotational frequency with a half line width of 1044 Hz. Increasing the rotational rate to 32 kHz the line width decreased to 800 Hz.

For comparison reasons it was first measured the chemical shift of the $\alpha - CrF_3$, which is a polymorphic framework iso-type with $\alpha - AlF_3$, consisting of regular octahedral CrF_6 units. The chemical shift δ is -132 ppm, FWHH (full width at half height) is 18.8 kHz at 30 kHz rotational speed (cf. Fig. 49). All further samples have been monitored at that very fast rotation. All resonance signals are of Lorentzian

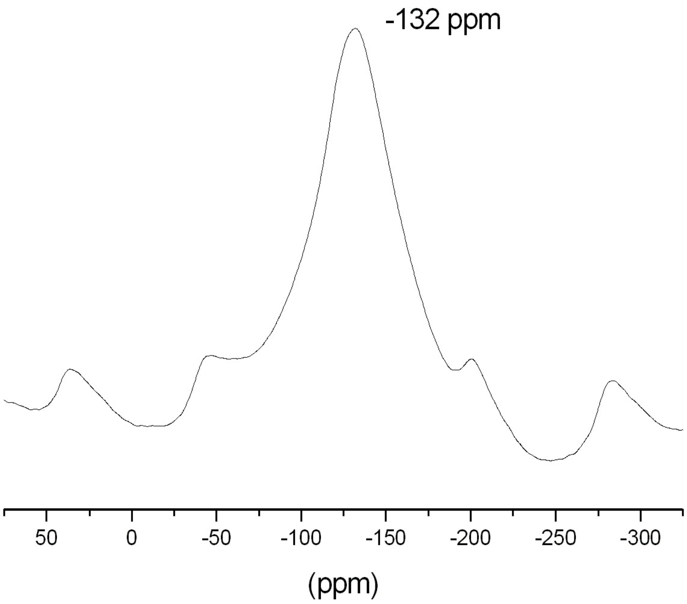

Figure 49: ^{19}F -MAS-NMR spectrum of $\alpha - CrF_3$ with rotation frequency of 30 kHz measured at 376.4 MHz

type and suitable to measure the exact chemical shifts.

For Cr_2O_3 treated with HF at 390 $°C$ for 15 min one signal is found at -134 ppm with line width 34 kHz. Cr_2O_3 samples activated with CCl_2F_2 at 390 $°C$ for 2 min and 15 h show also one signal each at -126 ppm with line width 18.8 kHz and at -138 ppm with line width 27,4 kHz, respectively.

In another study, MgF_2 doped with different concentrations of chromium oxide fluoride was activated by CCl_2F_2 at 350 $°C$. These samples also consist of oxide halides and are in agreement with the above mentioned ones. One of the $MgF_2/CrO_xF_yCl_z$ sample shows signals at -139 ppm and -198 ppm and another $MgF_2/CrO_xF_yCl_z$ sample shows signals at -141 ppm and -198 ppm. Signals at -139 ppm and -141 ppm are from F which bound to Cr and signals at -198 ppm are from F which bound to Mg [104].

Differences in chemical shifts, as it is observed in these cases, are generally attributed to changes in shielding behaviour by electrons near the measured nucleus. A shift to higher field could result from increasing shielding of the fluorine nucleus, i.e., from increased electron density.

It is quite clear that from the structural consideration, the octahedral surrounding of chromium is changing with the stepwise substitution of oxygen creating new compositions and, of course, new properties. The nearest neighbours of the considered fluorine are different as it is shown by the respective chemical shifts. As a result, the inactive and active catalysts show clearly different fluorine chemical shifts and they differ from the ones recorded for $\alpha - CrF_3$ and HF treated chromia.

3.8 FTIR-Photoacoustic Analysis

The use of pyridine to determine the nature of acidity on solid surfaces has been well established [105], [58].

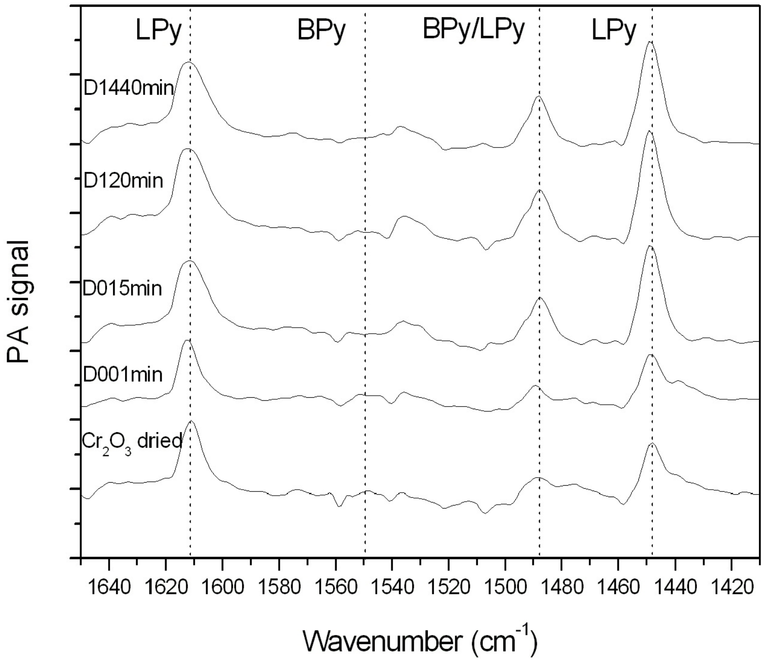

Figure 50: FTIR photoacoustic spectra of pyridine chemisorbed Cr_2O_3 samples activated at 390 $°C$

The lone-pair electron of the nitrogen atom of pyridine can either bind coordinatively to Lewis acid sites (LPy) or interact with acidic OH groups to form pyridinium cations or pyridine adsorbed via hydrogen bridge bonds, Brønsted sites (BPy). The 19b and 8a ring vibration modes of the pyridine molecules are very sensitive for distinguishing between adsorption on Lewis acid sites and that on Brønsted acid sites:

(1) Between the wavenumbers 1445 and 1455 cm $^{-1}$ 19b ring vibration mode of pyridine, which is coordinatively bonded to Lewis acid sites (LPy), are observed.

(2) At about 1493 cm $^{-1}$ 19a ring vibration mode of pyridine is observed. This pyridine is either coordinatively bonded to Lewis acid sites (LPy) or bonded to Brønsted acid sites (BPy).

(3) Between the wavenumbers 1540 and 1550 cm $^{-1}$ 19b ring vibration mode of pyridine corresponds to hydrogen bonded pyridine to quasi-Brønsted acid sites (BPy).

(4) At about 1615 cm $^{-1}$ 8a ring vibration mode of pyridine, which is coordinatively bonded to Lewis acid sites (LPy) of lower strength, is observed.

(5) At about 1620 cm $^{-1}$ 8a ring vibration mode of pyridine, which is coordinatively bonded to Lewis acid sites (LPy) of higher strength, is observed.

Figure 50 presents the bands which are characteristic for Lewis acid sites. The band at approximately 1490 cm $^{-1}$ appears due to Lewis acid sites only. Since there are no Brønsted acid sites are found at between the wavenumbers 1540 and 1550 cm $^{-1}$, the band at about 1493 cm $^{-1}$ appears due to Lewis acid sites. There are no Brønsted acid sites presented. Comparing the activated samples with the dried one reveals very slight increase in the number of the Lewis acid sites as well as very small shifts to the higher wavenumbers. The reason for this is the substitution of O with F. Since the electronegativity of F is higher than the one of O, the replacement of O with F polarizes the metal side more positively. Therefore, XPS results also show an increase in chromium(III) binding energy with further fluorination.

Pyridine chemisorbed on Brønsted acid sites is not presented. Therefore, it can be assumed that Brønsted acidity is not essential for the catalysis of the dismutation reaction.

3.9 Wet Chemical Analysis

Table 10: Comparison of wet chemical analysis (top) with ESCA (bottom)

Reaction	temp. ($^{\circ}C$)	time (min)	F (wt.-%)	Cl (wt.-%)	overall composition
Dismutation	300	15	0.1	1.3	$CrO_{1.48}F_{0.00}Cl_{0.03}$
Dismutation	300	120	0.6	2.0	$CrO_{1.47}F_{0.02}Cl_{0.04}$
Dismutation	390	1	0.2	0.9	$CrO_{1.49}F_{0.01}Cl_{0.02}$
Dismutation	390	15	0.5	1.8	$CrO_{1.47}F_{0.02}Cl_{0.04}$
Dismutation	390	120	0.7	1.9	$CrO_{1.47}F_{0.03}Cl_{0.04}$
Dismutation	390	1440	0.7	2.4	$CrO_{1.46}F_{0.03}Cl_{0.05}$
HF treatment	390	15	1.5	0.0	$CrO_{1.47}F_{0.06}$
HCl treatment	390	15	0.0	1.8	$CrO_{1.48}Cl_{0.04}$

Reaction	temp. ($^{\circ}C$)	time (min)	F (at.-%)	Cl (at.-%)	XPS surface composition
Dismutation	300	15	0.7	1.3	$CrO_{1.42}F_{0.02}Cl_{0.03}$
Dismutation	300	120	4.9	5.6	$CrO_{1.39}F_{0.13}Cl_{0.15}$
Dismutation	390	1	1.6	2.2	$CrO_{1.59}F_{0.04}Cl_{0.06}$
Dismutation	390	15	4.1	6.7	$CrO_{1.48}F_{0.11}Cl_{0.18}$
Dismutation	390	120	5.1	6.8	$CrO_{1.26}F_{0.13}Cl_{0.17}$
Dismutation	390	1440	5.1	6.2	$CrO_{1.31}F_{0.13}Cl_{0.16}$
HF treatment	390	15	11.5	0.0	$CrO_{1.13}F_{0.28}$
HCl treatment	390	15	0.0	6.1	$CrO_{1.24}Cl_{0.14}$

In the previous studies Kemnitz et al. [22] showed that the chemical analysis reveal 0.5 wt% fluoride and 0.4 wt% chloride in the conditioned chromia. In another investigation Hess et al. [58] reported slight chlorination (1-2 wt% chloride) and very small fluorination (about 0.3 wt% fluoride) in the activated samples. These results are consisting with the ones tabulated in Table 10.

The formation of chromia with CCl_2F_2 at 300 $^{\circ}C$ for 15 min and at 390 $^{\circ}C$ for 1 min was still incomplete. These two samples show that as soon as the chromia comes to contact with the CFC, the samples get halogenated. The rest of the activated samples in Table 10 were analyzed after the formation process was totally complete and the maximum activity was reached. These samples contain more fluoride and chloride than the ones obtained before the conditioning was complete, but further activation does not increase the halogenation of the samples. On the other hand, the chromia with HF treatment at 390 °C for 15 min contains more fluoride than the activated samples. The chromia with HCl treatment at 390 °C for 15 min exhibit chloride uptake as much as the activated samples. The fluorination is not as much competitive as the chlorination in the Cl/F exchange reaction on chromia and once the maximum activity is reached further halogenation is not taking place or the process is very slow.

The wet chemical analysis and ESCA show the same trend in halogenation of the samples, but the comparison of these two methods indicates clearly that the halogenation takes place merely on the surface.

3.10 Powder XRD Analysis

In order to check the crystalline bulk properties of the synthesized or commercially obtained samples and whether they are free from other crystalline phases, powder X-ray diffraction analyses were applied. The diffractograms of the samples are compared with the Powder Diffraction File (PDF) database [106]. The XRD pattern of the reference samples Cr_2O_3, $CrF_3.H_2O$, $\beta - CrF_3$, $\alpha - CrF_3$ and $CrCl_3$ were found in good agreement with the following PDF numbers 38-1479, 17-316, 80-555, 16-44 and 32-279, respectively. For identifying CrF_2OH and $Cr(OH)_3$ the references [40] and [107], which show the XRD pattern of chromium(III) hydroxide and the pyrochlore structure, are used. These results give confidence on the identity of the crystalline bulk of the samples under investigation.

On the other hand, in order to find out whether the crystalline bulk properties of the Cr_2O_3 is changing with activation or halogen treatment, the chromia samples activated with CCl_2F_2 or treated with HF or HCl at 390 $°C$ for 3 h are analyzed by XRD. The diffractograms of these samples are in agreement with the diffractogram of the reference Cr_2O_3 (PDF 38-1479, Eskolite) but the reflection intensities are slightly reduced and signal-to-noise ratios are decreased. The crystalline bulk properties are not significantly changing with activation or treatment.

3.11 Surface Area Analysis

The surface areas of the samples were determined by the Brunauer-Emmett-Teller (BET) method for sample characterization. Another purpose to determine the surface areas was to ensure that the ESCA indicates the surface properties of the samples and not the bulk properties. XPS analysis with high surface area samples can provide information from the bulk as well as from the surface. The BET surface areas for the reference samples Cr_2O_3, CrF_2OH, $\beta - CrF_3$, $\alpha - CrF_3$ and $CrCl_3$ were determined as 45.6, 1.5, 24.7, 0.4 and below the detection limit (< 0.1) m^2/g, respectively. Since $Cr(OH)_3$ and $CrF_3.H_2O$ decomposes above 100 $°C$, it is not possible to make surface area analysis with these samples.

All determined surface areas were significantly low and therefore, XPS results provides reliable information from the surface.

The BET surface areas for Cr_2O_3 samples activated with CCl_2F_2 or treated with HF or with HCl at 390 $°C$ for 3 h are found as 45.9, 43.6 and 44.9 m^2/g, respectively. They did not show any significant changes when compared with the surface area of the reference Cr_2O_3, which is the starting material. These results are consistent with the SEM results, which did not indicate any significant differences, either (cf. Sec. 3.6). As a result, the surface area of chromia does not alter with dismutation of CCl_2F_2 or with HF or HCl treatment.

4 Conclusion

From the spectroscopic point of view, it has been shown that problems of Cr(III) 2p XP spectra data reduction were solved.

Highly resolved XPS of Cr_2O_3 powder samples gave clear evidence for the existence of features related to multiplet splitting in the respective Cr 2p spectrum. The spectrum can be analyzed by peak fitting using BE initial values for the multiplet related features obtained from the respective Cr $L_{2,3}$ XANES.

From a theoretical point of view the same procedure should be also applied for an analysis of XP Cr 2p spectra of $\alpha - CrF_3$ and $CrCl_3$ and other chromium(III) compounds. The differences of the Cr_2O_3 and $\alpha - CrF_3$ and $CrCl_3$XP spectra observed in the experiments point to the fact that though in both cases the same multiplet splittings are theoretically to be expected for Cr^{3+} individual influences of symmetry and ligand fields define the final shape of the respective XP Cr 2p spectra.

Another consequence of this study is that the fingerprint approach relying on (i) Cr $2p_{3/2}$ and $2p_{1/2}$ doublet energy separations, (ii) Cr 2p main peak - satellite peak energy separations and (iii) satellite intensity/main peak intensity ratios used in the past to identify chemical states of Cr in solids must be given up. Due to the complexity of the manifolds of multiplet features in the 2p spectra the parameters (i) to (iii) either cannot be unequivocally determined by a peak fitting procedure or are physically meaningless. In that situation a pragmatic but reliable fingerprint approach for chemical state identification should use the BE of the first sharp multiplet feature at Cr $2p_{3/2}$ or the BE of the absolute maximum of Cr $2p_{3/2}$ as well as the BE and intensity of the $2p_{1/2}$ satellite around BE = 600 eV. In order to derive chemical state information any Cr 2p spectrum of chromium compounds must be definitely measured comprising the respective satellite features, i.e. using a sufficiently broad energy window up to $\approx$ 610 eV.

An analysis of Cr 3s spectra also may provide an approach for finger-printing chemical states of chromium(III) compounds.

From the chemical point of view, the present study provides information about the inactive and active stages of the chromia catalyst which is used for the Cl/F exchange reactions and a model of the catalyst's surface chemistry.

The pyridine FTIR-photoacoustic analysis shows that the catalytic Cl/F exchange reaction takes place on the Lewis acid sites which are coordinatively unsaturated chromium sites. The chromia catalyzed dismutation reaction of CCl_2F_2, which is a Cl/F exchange reaction causes the catalyst surface to be fluorinated and chlorinated simultaneously. The wet chemical analysis and the quantitative ESCA results reveal that the halogenation takes place merely on the surface. This is also supported by the SEM and surface area analysis because the surface morphology of the Cr_2O_3

and its BET surface area do not change significantly by the dismutation reaction of CCl_2F_2 or HF treatment. The Cr K-edge XANES analysis performed in transmission mode also indicates that the halogenation takes place at the very surface. The crystalline bulk properties of chromia are not significantly changing with the activation or halogen treatment.

The low binding energies of the F 1s and Cl 2p core levels in the pre-catalytic sample and the symmetric peaks in the XP spectra indicate single major components. These represent the formation of a coordinatively unsaturated surface species during the early stages of halogenation. These species are bound to the exposed Lewis acid sites and to the other surface defects initially present on the chromia surface. The fluoride ions terminally bound to the chromium atoms without disturbing the Cr_2O_3 lattice are detected as a F K-edge TEY-XANES spectrum very different from those of CrF_3 and CrF_2OH and from the longer activated chromia samples.

The active sites and intrinsic defects on the chromia are not able to provide catalytic activity for Cl/F exchange reaction but they initiate the halogenation of the catalyst. With further activation time the catalyst became active and F K-edge TEY-XANES spectra with main features indicating CrF_3 were obtained. Hence, when the fluorine is integrated into the subsurface region the catalyst becomes active.

According to the pyridine FTIR-photoacoustic analysis, increasing halogenation levels raise the Lewis acidity of the catalyst further as the catalytic reaction proceeds. The XPS Cr 2p BE also increases. The catalytically active, strongly Lewis acidic active sites are formed only after halogenation has begun to proceed to the subsurface region of the sample. Nucleation of a CrF_3 or $CrCl_3$ was not detected. The accumulation of the fluorine and chlorine by the surface reaction with the chlorofluorocarbon results in chromium oxide halide structure at the surface. This is also concluded from the ToF-SIMS results by observing $\mathrm{CrO}_x\mathrm{Cl}_y\mathrm{lF}_z$ and $\mathrm{CrCl}_x\mathrm{F}_y$ fragments for the activated samples. The chloride and fluoride ions are bound to the same chromium metal constructing the chromium oxide chloride fluoride species.

The fluorine solid state NMR analysis differentiate the inactive and active catalysts by observing different fluorine chemical shifts and they differ from the chemical shifts recorded for $\alpha - CrF_3$ and HF treated chromia. The fluorine ions in these four samples are different from each other because the chemical environment of each fluorine atom in these samples is different or they are bound to a chromium atom where each has a different chemical environment.

The quantitative XPS analysis show that the maximum catalytic activity is reached when the surface of chromia is approximately 4 atom% fluorinated and 6 atom% chlorinated as a result of dismutation reaction of CCl_2F_2 at 390 $°C$. Almost similar results are also obtained for the samples activated at 300 $°C$ and for "in-situ" XPS analysis. Also long times of exposure to CCl_2F_2 do not alter the surface composition significantly after the maximum activity was reached. Once the maximum activity was obtained the halogenation of chromia is a very slow process. The activation of the catalyst takes longer time at 300 $°C$.

HF treatment of chromia at 390 $°C$ for 9 h, forms chromium oxide fluoride species at the sample surface. No conversion to CrF_3 is found. HCl treatment of chromia at 390 $°C$ for 9 h, forms chromium oxide chloride species at the sample surface. No conversion to $CrCl_3$ is found.

Pre-fluorination does not obstruct the following chlorination on chromia surface and in the same way pre-chlorination does not hinder the following fluorination of the chromia surface. The fluorination and chlorination reactions of chromia are competitive with each other.

Reliable results can be obtained for activated chromia by ex-situ XPS analysis when careful sample preparation methods are performed for avoiding air contamination.

Excluding the necessity of $CrCl_3$ species for the catalytic activity since it is known as an inert substance, the formation of CrF_3 is not required for the achievement of catalytic activity. Instead of this, $\mathrm{CrO}_{(x-y-z)}\mathrm{Cl}_y\mathrm{F}_z$ species are sufficient to induce the onset of the catalytic activity.

Coke formation at the catalyst surface is not detected. The difference between the C 1s and Au $4f_{7/2}$ referenced static charging is constant. The C 1s BE can be used for static charge referencing.

5 Zusammenfassung

Es wurde gezeigt, dass die Probleme der Behandlung von Cr (III) 2p Photoelektronenspektren so gelöst werden können, dass ihnen relevante Daten für die chemische Charakterisierung von Oberflächen entnommen werden können.
Hochaufgelöste PES von Cr_2O_3 Pulverproben zeigte deutlich die Existenz von spektralen Strukturen, die mit Multiplet-Aufspaltungen im jeweiligen Cr 2p Spektrum verbunden sind. Das Spektrum kann durch eine Peakfit-Analyse vertieft interpretiert werden in dem die Anfangswerte für die Peakparameter der Multiplet-Strukturen den jeweiligen Cr $L_{2,3}$ XANES Spektren entnommen werden.
Vom theoretischen Gesichtspunkt sollte dasselbe Verfahren auch eine Analyse der Cr 2p Photoelektronenspektren von $\alpha - CrF_3$, $CrCl_3$ und anderen Chrom (III) Verbindungen ermöglichen. Die Unterschiede, die im Experiment für die Cr_2O_3, $\alpha - CrF_3$ und $CrCl_3$ Photoelektronenspektren beobachtet werden, deuten auf die Tatsache, dass, obwohl in all diesen Fällen dieselben Multiplet-Aufspaltungen für Cr^{3+} erwartet werden, individuelle Einflüsse der Symmetrie und Ligandenfelder die Endgestalt des jeweiligen Cr 2p Photoelektronenspektrums definieren.
Eine andere Folgerung dieser Studie ist, dass der in der Vergangenheit verwendete Finger-print Zugang, der auf (i) Cr $2p_{3/2}$ und $2p_{1/2}$-Dublett-Bindungsenergiedifferenzen, (ii) Cr 2p Hauptpeak - Satellitenpeak Bindungsenergiedifferenzen und (iii) Satelliten / Hauptpeakintensitätsverhältnissen basierte und der es ermöglichen sollte, chemische Zustände von Cr (III) in Festkörperoberflächen zu identifizieren, aufgegeben werden muss. Aufgrund der Kompliziertheit der Struktur der Multiplet-Aufspaltungen in den Chrom (III) 2p Spektren können die Ansätze (i) - (iii) entweder keine eindeutigen Ergebnisse erbringen oder sie sind sogar physikalisch sinnlos. In dieser Situation sollte ein pragmatischer aber zuverlässiger Finger-print Zugang für die Identifizierung chemischer Zustände benutzt werden. Die BE der ersten scharfen Multiplet-Struktur für Cr $2p_{3/2}$, oder die BE vom absoluten Maximum des Cr $2p_{3/2}$ Peaks sowie die spektroskopischen Parameter des $2p_{1/2}$-Satelliten (BE und Intensität) um = 600 eV BE können dazu dienen. Um chemische Zustandinformation abzuleiten, muss jedes Cr 2p Spektrum von Chromverbindungen so gemessen werden, dass die jeweiligen Satellitenstrukturen mit erfasst werden. Dazu muss ein genügend breites Energiefenster bis zu BE $\approx$ 610 eV vermessen werden.
Eine Analyse von Cr 3s Spektren kann zusätzlich wertvolle Finger-print Informationen zu chemischen Zuständen von Chrom in Cr (III) Verbindungen erbringen.

Die vorliegende Dissertation beinhaltet Informationen über die inaktiven und aktiven Phasen eines Chromoxyd-Katalysators, der für Cl/F-Austauschreaktionen verwendet wird. Ein Modell der Oberflächenchemie des Katalysators in seinen verschiedenen Zuständen wird aufgestellt.

Die photoakustische FTIR - Analyse nach Pyridin Adsorption zeigt, dass die katalytische Cl/F-Austauschreaktion an Lewis-Säurezentren stattfindet, die koordinativ ungesättigte Chromspezies sind. Die durch Chromoxyd katalysierte Dismutierungsreaktion von CCl_2F_2, die eine Cl/F-Austauschreaktion ist, verändert die Katalysatoroberfläche indem diese gleichzeitig fluoriert und chloriert wird. Die nasschemische Analyse und die quantitativen ESCA-Ergebnisse zeigen, dass die Halogenierung auf die Oberfläche beschränkt bleibt. Diese Feststellung wird durch die Ergebnisse der REM- und Oberflächen-Analysen unterstützt. Weder die Oberflächenmorphologie des Cr_2O_3 noch dessen BET-Oberfläche werden durch die Dismutierungsreaktion von CCl_2F_2 oder eine HF Behandlung signifikant verändert. Die XANES Analyse der Cr K-Kante, durchgeführt im Transmissionsmodus, zeigt ebenfalls, dass die Halogenierung nur an sehr oberflächennahen Oberflächemnbereichen stattfindet. Der kristalline Charakter des Volumens des aktivierten Chromoxyds ändert sich bei Aktivierung oder Halogenbehandlung nicht wesentlich.

Die niedrigen Bindungsenergien der F 1s und Cl 2p Rumpfniveaus in den XP Spektren, die für die katalytisch inaktiven Proben gemessen werden, und deren symmetrische Peakform zeigen, dass diese jeweils mit einer einzigen Hauptkomponente interpretiert werden können. Diese stehen in Verbindung mit der Bildung einer koordinativ ungesättigten Oberflächenspezies während der frühen Phase der Halogenierung. Diese Spezies sind an die verfügbaren Lewis-Säurezentren und an Oberflächendefekte, die anfänglich an der Chromoxyd-Oberfläche existieren, gebunden. Die Fluorid-Ionen finden sich in terminalen Positionen an Chrom-Atome gebunden und stören das Cr_2O_3 Gitter im Volumen nicht. Sie werden durch die Form der F K-Kante im TEY-XANES Spektrum identifiziert. Ihr Spektrum unterscheidet sich deutlich von denjenigen, die an CrF_3, CrF_2OH und von länger aktivierten Chromoxyd Proben gemessen wurden.

Die aktiven Plätze auf dem Chromoxyd sind nicht stark genug, um die Cl/F-Austauschreaktion zu katalysieren, aber sie sind Ausgangspunkt für die Halogenierung des Katalysators. Mit fortschreitender Aktivierungszeit wird der Katalysator aktiv und die TEY-XANES Spektren der F K-Kante zeigen Strukturen, wie sie auch in den Spektren von CrF_3 gefunden werden. Daraus lässt sich schließen, dass die Fluorierung auch Bereiche unterhalb der äußersten Monolage erreicht, wenn der Katalysator aktiv wird.

Die photoakustische FTIR - Analyse nach Pyridin Adsorption zeigt, dass mit zunehmender Halogenierung die Lewis-Acidität des Katalysators steigt. Der XPS Cr 2p BE nimmt parallel dazu zu. Das katalytisch aktiven, stark Lewis-sauren Oberflächenplätze bilden sich erst nach der Halogenierung der Bereiche unterhalb der äußersten Monolage der Probe. Die Nukleation von CrF_3 oder $CrCl_3$ Phasen wurde jedoch nicht beobachtet. Die Anreicherung von Fluor und Chlor im Verlauf der Oberflächenreaktion mit dem Fluorchlorkohlenstoff begründet sich mit der Ausbildung eines oberflächlich halogenierten Chromoxyds. Diese Schlussfolgerung lässt sich auch aus den Ergebnissen der Flugzeit-Sekundärionen-Massenspektrometrie (TOF-SIMS) ziehen. $CrO_xCl_ylF_z$ und $CrCl_xF_y$ Fragmentsekundärionen wurden für die aktivierten Proben beobachtet. Chlorid- und Fluorid-Ionen werden offensichtlich am selben Chrom-Atom gebunden und Chrom-Oxydchlorid-Fluorid-Spezies gebildet.

Die Fluor-Festkörper NMR Analyse unterscheidet die inaktiven und aktiven Katalysatoren durch verschiedene chemische Verschiebungen für Fluor. Diese wiederum unterscheiden sich von den chemischen Verschiebungen, die für $\alpha - CrF_3$ und HF behandeltes Chromoxyd gemessen werden. Die Fluor-Ionen in diesen vier Proben unterscheiden sich durch ihre jeweilige chemische Umgebung oder durch ihre Bindung an Chrom-Atome die sich ihrerseits in unterschiedlichen chemischen Umgebungen befinden.

Die quantitative XPS Analyse zeigt, dass die maximale katalytische Tätigkeit erreicht wird, wenn die Oberfläche von Chromoxyd infolge der Dismutierungsreaktion von CCl_2F_2 bei 390 $°C$ zu etwa 4 atom% fluoriert und 6 atom% chloriert ist. Sehr ähnliche Ergebnisse werden auch für die Proben erhalten, die bei 300 $°C$ aktiviert wurden. Die Aktivierung des Katalysators benötigt bei 300 $°C$ eine längere Zeit. "insitu" XPS Analysen führen zum gleichen Ergebnis. Auch lange Zeiten einer CCl_2F_2 Exposition verändern die Oberflächenkonzentrationsverhältnisse nicht mehr nachhaltig, wenn die maximale Aktivität bereits erreicht wurde. Sobald die maximale Aktivität erreicht ist, ist die weitere Halogenierung von Chrom ein sehr langsamer Prozess.

Eine 9 stündige HF-Behandlung von Chromoxyd bei 390 $°C$ bildet Chrom-Oxydfluorid-Spezies an der Probenoberfläche. Eine Konvertierung zu CrF_3 wird nicht gefunden. Eine 9 stündige HCl-Behandlung von Chromoxyd bei 390 $°C$ bildet Chrom-Oxydchlorid-Spezies an der Probenoberfläche. Eine Konvertierung zu $CrCl_3$ wird ebenfalls nichtgefunden.

Eine Pre-Fluorierung verhindert eine folgende Chlorierung der Chromoxyd-Oberfläche nicht, und genauso verhindert eine Pre-Chlorierung eine folgenden Fluorierung der Chromoxyd-Oberfläche nicht. Der Fluorierungs und Chlorierungsreaktionen des Chromoxyds sind miteinander konkurrenzfähig.

Zuverlässige Ergebnisse können für aktiviertes Chromoxyd auch in einer ex-situ XPS Analyse erhalten werden, wenn vorsichtige Probenvorbereitungsmethoden angewandt werden, die die Laborluftexposition minimieren.

Für die katalytische Aktivität ist die Existenz von $CrCl_3$ an der Oberfläche nicht erforderlich. $CrCl_3$ ist als katalytisch inaktiv bekannt. Die Bildung von CrF_3 ist für die katalytische Aktivität von Chromoxyde in der untersuchten Dismutierungsreak-

tion ebenfalls nicht erforderlich. Statt dessen ist die Bildung von $CrO_{(x-y-z)}Cl_yF_z$ Spezies ausreichend für die Einstellung der katalytischen Aktivität.
Hinweise auf eine Koks-Bildung an der Katalysator-Oberfläche wurden nicht erhalten. Es wurden keine Unterschiede bei der Nutzung einer C 1s oder Au $4f_{7/2}$ basierten Referenz für die Korrektur der statischen Aufladung in der XPS an unterschiedlichen Aktivierungszuständen der Katalysatoroberfläche gefunden. Die C 1s BE des aliphatischen Kohlenstoffs kann deshalb erfolgreich für die Korrektur der statische Aufladung verwendet werden.

6 Outlook

The proposed spectral peak-fit analysis for understanding the spectral features of Cr 2p XP spectrum can be applied to the other first period transition metal compounds of which are non-conductive and possess singly filled d orbitals resulting in complicated spectral features. In addition, theoretical atomic calculations can provide very good initial parameters and will be helpful for deeper understanding about the phenomena as well as a better theoretical base by linking the both XPS and XAS processes.

For a very surface sensitive catalyst characterization in-situ ToF-SIMS can be a very useful and an ultimate technique also for inorganic systems. With further careful investigations a proper analysis procedure can be developed and can be used as a routine in applications. Valuable information for surface mechanistic studies can be extracted from in-situ ToF-SIMS analysis.

For Cl/F exchange reactions catalysts with higher surface area chromium(III) oxide halide structures in different compositions can be tried to synthesize and activation studies can be performed. Proposed structural models can be studied with EXAFS method.

7 Experimental

7.1 Sample preparation

Cr_2O_3: was synthesized by volcano reaction of $(NH_4)_2Cr_2O_7$. To get rid of the impurities the primary reaction product was boiled with distilled water for 4 h, filtered, washed with distilled water and dried in air.

$Cr(OH)_3$: was prepared by the addition of 0.1 M chromium nitrate to 0.25 M ammonia until a pH of 10.5 was reached. The gel obtained was allowed to settle. It was separated by centrifugation and then washed twice with distilled water, three times with acetone, slurried with diethyl ether, and again separated by centrifugation. It was dried for 24 h at room temperature in air [107].

$CrF_3.H_2O$: Chromium(III) nitrate was dissolved in slightly heated ethanol. The mixture was added dropwise to a stirred 40 wt% hydrofluoric acid solution. After 1h the precipitate was separated, washed with water and ethanol and dried in air.

CrF_2OH: $CrF_3.H_2O$ was covered by aluminium foil to allow a self produced atmosphere, then heated to 390 $°C$ with a rate of 2 $°C$/min and kept at this temperature for 1 h under ∼ 20 ml/min Ar flow.

$\beta - CrF_3$: $(NH_4)_3CrF_6$ was covered by aluminium foil to allow a self produced atmosphere, then heated to 490 $°C$ with a rate of 3 $°C$/min and kept at this temperature for 2 h under ∼ 20 ml/min Ar flow.

$\alpha - CrF_3$: Commercial product (Aldrich) received under Ar in a closed ampule.

$CrCl_3$: Commercial product (Aldrich) received under Ar in a closed ampule.

7.2 Experimental Setup

7.2.1 Dismutation of CCl_2F_2 in real reaction conditions

Cr_2O_3 catalyst samples were prepared to corn size of 0.3 - 0.5 mm by pressing under 5t and sieving. Approximately 0.4 g catalyst was set into a vertical nickel reactor of length 400 mm and inner diameter 5 mm (cf. Fig. 51 (right)). The catalyst was hold in the middle of the reactor by a piece of silver wool. The reactor was heated in a cylindrical resistance oven which was equipped with a temperature controller. The flow of CCl_2F_2 and N_2 was adjusted with mass flow controllers (MKS instruments) to 2 and 10 ml/min, respectively so that the residence time was about 2 s. The lining to and from the reactor was made with PTFE tubes which were also heated with heating bands in order to prevent any condensation. The outlet was directly connected to a GC where the amount of dosing was controlled by a specific valve. Before conditioning the catalyst samples, they were dried in N_2 flow at 400 $°C$ for 3 h. The reactions are carried out at 390 $°C$. All the preparation for XPS analysis was done in a dry box and the samples are transferred in a desiccator in order to minimize the air exposure. Hence, the catalyst samples could be transferred into the XP spectrometer within few seconds of exposure to air.

7.2.2 Dismutation of CCl_2F_2 in simulated reaction conditions

The reactions were also performed in a reactor which is directly mounted to the extended preplock chamber of XP spectrometer (cf. Fig. 51 (left) and 52). The reactor was separated by a valve from the extended preplock chamber and that was separated from the measuring chamber by another valve. The reactions were taking place at 390 $°C$ in atmospheric pressure conditions after drying the samples in N_2 flow at 400 $°C$ for 3 h. The effluent gas was collected in glass containers for off-line GC analysis. After each reaction the reactor was pumped down to UHV so that the activated catalyst sample was transferred first to the extended preplock chamber and then to the spectrometer without any air contact. This mode of analysis is often but not correctly called "in-situ" analysis.

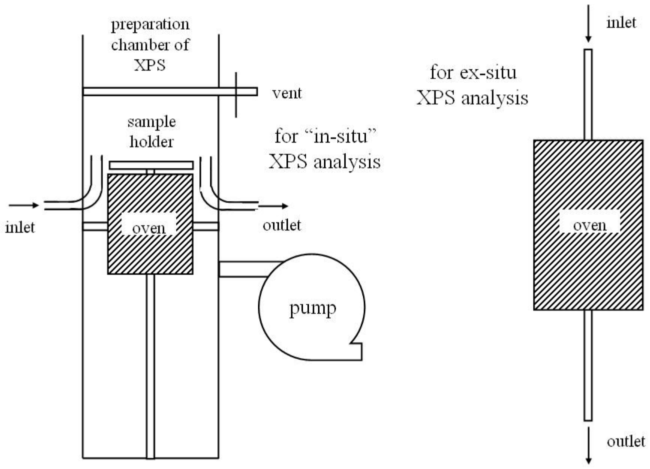

Figure 51: Sketch of reactor mounted to the preplock of ESCALAB 200X spectrometer for "in-situ" XPS analysis (left) and tubular flow reactor for ex-situ XPS analysis (right).

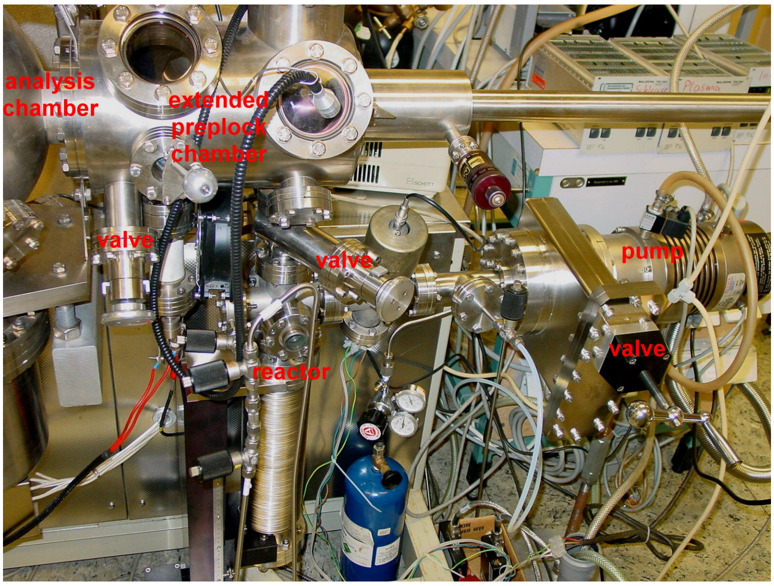

Figure 52: Reactor mounted to the preplock of ESCALAB 200X spectrometer

7.3 Analytical Methods

7.3.1 X-ray Photoelectron Spectroscopy (XPS)

XP spectra were acquired with a VG SCIENTIFIC ESCALAB 200X electron spectrometer (cf. Fig. 53). This equipment consists of a double anode X-ray tube, a hemispherical energy analyzer and an electron detector. It is possible to excite the samples either with AlKα or MgKα of which the photon energies are 1486.6 and 1253.6 eV, respectively. This provides the chance to separate the photoelectron and Auger peaks when there is an overlapping by shifting the Auger peak using a different excitation energy. The electron analyzer is an energy filter. It always allows passing electrons that possess a certain kinetic energy with a small half width. After passing through the analyzer the electrons reach the detector where they are detected by chaneltrons. Elemental surface composition and their chemical state can be extracted from the photoelectron spectrum. For the spectral analysis and chemical interpretation the softwares Unifit 2003 (University Leipzig, Germany) and Eclipse 2.0 (VG Scientific, UK) were used.

X-ray photoelectron and X-ray excited Auger electron wide and narrow scan spectra were acquired using non-monochromatized AlKα excitation operated at 15 kV and 20 mA. Wide and narrow scans were recorded in CRR 10 and CAE 10 modes, respectively. Cr LMM narrow scan XAES was acquired in CAE 20 mode. The vacuum in the spectrometer was in the range of 10^{-9} mbar during the measurements. The spot size was adjusted to a diameter of 3 mm. Binding or kinetic energy data were referenced to the aliphatic C 1s peak at 284.8 eV [85]. No flood gun was used for charge compensation. The spectrometer energy scale was calibrated following

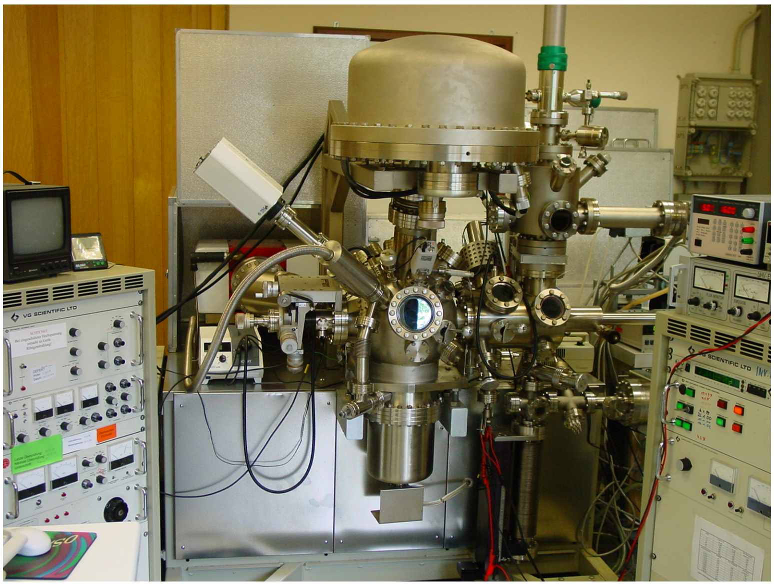

Figure 53: ESCALAB 200X

ISO 15472 [87].

In addition, spectra of the reference samples, which are Cr(III) compounds of O, F and Cl, were also acquired with a KRATOS AXIS ULTRA electron spectrometer, which is a new generation XPS. These spectra were acquired using monochromatized AlKα excitation operated at 15 kV and 20 mA with an advanced charge compensation system. The wide and narrow scans were recorded in CAE 160 and CAE 20 modes, respectively. The Cr 2p spectrum is also acquired in CAE 10 mode. Energy data referencing was done in a similar way as it was done for the ESCALAB 200X. The energy scale calibration is described in the handbook of the equipment [108].

7.3.2 X-ray Absorption Near Edge Structure (XANES)

The X-ray absorption near edge structure (XANES) spectra at the Cr $L_{2,3}$-edge of the reference samples were obtained in the total electron yield (TEY) mode with a high energy spherical grating monochromator (HE-SGM) using 50 μm slits in beamline station D-08-1B1 of the synchrotron radiation source BESSY II, Berlin, Germany. This station has a toroidal mirror. The 1500 l/mm spherical grating covering an energy range 200-900 eV with 0.8 eV resolution at the C K-edge is used in the experiments. All optical elements are Pt coated. The powder samples were prepared by pressing them into an In metal sheet.

The XANES spectra at the F K-edge and Cr $L_{2,3}$-edges of the reference and activated samples were acquired in total electron yield (TEY) mode at the undulator beamline station 5U.1 of the synchrotron radiation source Daresburey, Warrington, UK. This station consists of an entrance-slitless SX700 type plane grating monochromator with a spherical focusing mirror, a 6m-exit arm and an ellipsoidal post-focusing mirror. All optical elements are Pt coated. The monochromator has a single 1200 l/mm grating covering an energy range 60 to 1000 eV. The monochromator performance is periodically checked by measuring the photocurrent from a gold mesh and by measuring the Ar L_3-edge. The photocurrent from the Au mesh is about 3.2 nA /100 mA of ring current, measured at 460 eV with the undulator at its minimum gap of 42 mm and the exit slit set to 100 m. This is approximately equivalent to a flux of 2.8 x 10^{11} photons/s at 100 mA ring current into a 0.1 % bandwidth. The resolution can be deduced from the measured width of the Ar peak at 244 eV. A total resolution of 0.1 eV at 244 eV with a 50 μm exit slit can be typically achieved. Samples were prepared on double sided slightly conductive carbon band, which is mounted on a gold sample holder plate. In order to avoid charging effects in TEY measurements, the measurement cell was backfilled with He (99.99 %) until a pressure of approximately 0.65 mbar was obtained.

The XANES spectra at the Cr K-edge of the reference and activated samples were acquired in the transmission mode at the hard X-ray beamline, BAMline (cf. Fig. 54), at BESSY II. The main optical elements of the beamline are a double-multilayer-monochromator and a double-crystal-monochromator. The two devices can be used separately or in-line. In the experiments both are used in series in order to optimize the results. The double crystal monochromator consists of Si(111) or Si(311) crystals covering the energy range 6 to 60 keV. A monoenergetic photon flux with a maximum density of 1010 photons/$s.mm^2$ and an energy resolution of 0.1 to 0.2 eV can be obtained. The double multilayer monochromator consists of a stack of 150 W/Si layers (d = 2.8 nm) covering the photon energy range 4 to 40 keV. A monoenergetic photon flux with maximum density of 1012 photons/$s.mm^2$ and an energy resolution of 10 eV is obtained.

Figure 54: BAMline

For the analysis of the XANES spectra the WINXAS (Version 3.0) software was used. The background correction and the normalization of the F K-edge and Cr $L_{2,3}$-

edges TEY-XANES spectra was done by using a victoreen fit. For the background correction and the normalization of the Cr K-edge XANES spectra two polynomial fit each of order of one was used.

7.3.3 Time of Flight Secondary Ion Mass Spectroscopy (ToF-SIMS)

The static SIMS spectra were obtained by a time-of-flight secondary-ion mass spectrometer, TOF-SIMS IV, designed and manufactured by Ion-Tof GmbH, Muenster, Germany. Targets were bombarded by a 15 keV Ga^+ primary ion beam with a pulsed primary ion current of 0.80 pA. For each analysis, the ion beam was digitally scanned with a 128 times 128 array over an analysis area of 200 μ m times 200 μ m. Total acquisition times were fixed to 50 s. Thus the total ion dose was less than 6.0 x 10^{12} ions/cm^2, which was well below the so-called static limit of SIMS (1.0 x 10^{13} ions/cm^2). Secondary ions generated by a primary ion pulse on the target surface were extracted and accelerated to energy of 2 keV. An Einzel lens and reflection optics were used for focusing the secondary ion beam and for energy compensation, respectively, in the flight tube. The ions were post-accelerated to 10 keV just ahead of the detector, which was a channel plate-scintillator-photomultiplier combination. A time-to-digital converter was used for data collection. Because of charging low energy electrons were used to stabilize the surface potential of the samples during analysis.

7.3.4 Scanning Electron Microscopy (SEM)

The powder samples were prepared on double side adhesive carbon bands and covered with a 20 nm thick gold layer in an EMITECH K 500 sputtering equipment operated at 25 mA and under vacuum conditions better than 1x10^{-1} mbar. The SEM analyses were done with a Cambridge STEREOSCAN 180 equipped with a tungsten hairpin cathode and an Everhart-Thornley-Detector. The maximum acceleration voltage of the primary electrons is 30 kV and the maximum resolution is 70 Å. The SEM pictures were acquired from secondary electrons possessing 20 keV of energy.

7.3.5 Fluorine Solid State NMR Analysis

The fluorine solid state NMR experiments were carried out with a Bruker instrument using a 2.5 mm double-bearing magic angle spinning (MAS) probe with a decoupling channel optimized for ^{19}F observation. The samples were characterized at room temperature by measurements of ^{19}F ($I = \frac{1}{2}$, 376.4 MHz) nucleus. ^{19}F-MAS-NMR was performed at a spinning speed of 30 kHz. The chemical shifts are related to CCl_3F.

7.3.6 FTIR-Photoacoustic Analysis

The photoacoustic spectrum was recorded by FTIR-System 2000 from Perkin Elmer where the METC 300 photoacoustic unit was mounted. Approximately 80 mg sample was charged in it and treated with two times 30 μl pyridine at 150 $°C$ for 15 min in a vertical flow reactor where silver wool for holding the sample and 10 ml/min Ar as carrier gas were used. After cooling the treated sample to room temperature, it is transferred into the photoacoustic unit. The sample was flushed with He for 10 min. All spectra were normalized to 100 % transmission.

7.3.7 Wet Chemical Analysis

Fluorine Analysis Since the samples were not soluble, they were decomposed in concentric acids. Therefore, amounts of 20 to 60 mg of samples were melted with a mixture of 500 mg Na_2CO_3 and 500 mg K_2CO_3 in a Pt-pot for 20 min. After cooling down, the obtained mixtures were dissolved in concentric H_3PO_4 or H_2SO_4. The determination F concentration was carried out according to Seel [109] using a fluoride sensitive electrode.

Chlorine Analysis A solution of 4 ml H_2O and 5 drops H_2O_2 was prepared in a volumetric flask. The sample was added to this solution and after 30 min it was washed with 20 ml alcohol and 0.5 ml nitric acid (0.5 N). 2 drops of 1wt% diphenylcarbazone (DPC) was added and the titration was followed with mercury(II) chloride (0.01 N). Thus, the DPC acts as an indicator, changing from pink to blue when the first excess of mercury (II) appears.

7.3.8 Powder X-ray Diffraction (XRD)

XRD of the powder samples were performed with CuKα excitation using the XRD 7, Bragg-Brentano-Geometry with Ni filter, from Seiffert-FPM.

7.3.9 Surface Area Analysis (BET)

Surface area of the samples were analyzed according to the BET method using ASAP 2000 from Micromeritics. The samples were degassed at 250 $°C$ until high vacuum conditions were reached ($\sim 10^{-5}$ mbar). The adsorption isotherms were constructed point by point by the admission of the successive charge of N_2 (99.999 %) with the sufficient time allowed for equilibrium of each point.

7.3.10 Gas Chromatography (GC)

The organic reaction products were determined by GC Shimadzu 14a using 10 % SE 30 Chromosorb column and flame ionization detector (FID). For the separation of the organic products a heating program was applied. The initial temperature of the column was adjusted to 35 $°C$ and kept constant for 4 min, then it was heated with a rate of 10 $°C$/min until 100 $°C$ is reached and kept again constant at this temperature. The retention times for the organic products, $CClF_3$, CCl_2F_2, CCl_3F and CCl_4 were determined as 4.5, 5.0, 7.2 and 11.6 min, respectively.

8 Nomenclature

AES	Auger electron spectroscopy
AP	Auger parameter
BAM	Bundesanstalt fuer Materialforschung und -pruefung
BE	binding energy
BESSY	Berliner Elektronenspeicherring-Gesellschaft fuer Synchrotonstrahlung m.b.H.
BET	Brunauer-Emmett-Teller adsorption isotherm
CAE	constant analyser energy
CFC	chlorofluorocarbon
CRR	constant retard ratio
DPC	diphenylcarbazone
DR	dismutation ratio
ESCA	electron spectroscopy for chemical analysis
EXAFS	extended X-ray absorption fine structure
FID	flame ionization detector
FTIR	Fourier transform infrared spectroscopy
FWHH	full width at half height
FWHM	full width at half maximum
GC	gaschromotography
HCFC	hydrochlorofluorocarbon
HE-SGM	high energy spherical grating monochromator
HFC	hydrofluorocarbon
HTB	hexagonal tungsten bronze
ISO	the International Organization for Standardization
KE	kinetic energy
LEED	low energy electron diffraction
MAP	modified Auger parameter
MAS	magic angle spinning
NEXAFS	near edge X-ray absorption fine structure; also synonym for XANES
NMR	nuclear magnetic resonance
PA	photoacoustic
PCE	perchloroethylene, tetrachloroethylene
PDF	powder diffraction file
PTFE	polytetraphatalyte ethylene
SAA	surface area adsorption
SCF	self consistent field
SE	standard error
SEM	scanning electron microscopy
SIMS	secondary ion mass spectroscopy

SRS	synchrotron radiation source
SSIMS	static secondary ion mass spectroscopy
TCE	trichloroethylene
TEY	total electron yield
ToF-SIMS	Time of Flight Secondary Ion Mass Spectroscopy
TPD	temperature programmed desorption
UHV	ultra high vacuum; $p < 10^{-6}$ mbar
UV	ultra-violet radiation
WCA	wet chemical analysis
XAES	X-ray Auger electron spectroscopy
XAFS	X-ray absorption fine structure
XANES	X-ray absorption near edge structure
XAS	X-ray absorption spectroscopy
XFY	X-ray fluoresence yield
XPS	X-ray photoelectron spectroscopy
XRD	X-ray diffraction

A	area of sample
a	absorption coefficient
α	Auger parameter
α'	modified Auger parameter
β	half of FWHM
BE_{atom}	binding energy of a core electron in a free atom
BE_{PE}	binding energy of photoelectron
ΔBE	chemical shift
C_x	atom fraction
D	detection efficiency
$\Delta\varepsilon_e$	energy of electron shell in ground elemental state
ΔE_{corr}	correlation energy contribution
ΔE_H	Koopman's level shift
ΔE_{relax}	atomic relaxation energy
E_F	Fermi level
E_v	vacuum level
ΔG	Gibbs free energy
h	Planck's constant
I	intensity transmitted through sample
I_0	x-ray intensity incident on sample
J	x-ray flux
k	change in core potential

KE_{Auger}	kinetic energy of an Auger electron
KE_{PE}	kinetic energy of an photoelectron
L	angular asymmetry
λ	inelastic mean free path
M	mixing ratio
n	number of atoms
ν	frequency of light
ϕ_s	work function
p	momentum of photoelectron
q_j	charge of ions
R^a	atomic contribution
R^{ea}	extra-atomic contribution
R_j	distance from the central atom
σ	photoelectric ionization cross-section
S	atomic sensitivity factor
θ	angle of emission
t	sample thickness
T	analyzer transmission
V	Madelung potential
x_0	binding energy value at the peak centre

References

[1] M. P. Seah and W. A. Dench. *Surf. Interface Anal.*, (1):2, 1979.

[2] B. W. Veal and A. P. Paulikas. *Phys. Rev. B*, (31):5399, 1985.

[3] J. E. Lovelock. *Nature*, (230):379, 1971.

[4] M. J. Molina and F. S. Rowland. *Nature*, (249):810, 1974.

[5] F. S. Rowland and M. J. Molina. *Rev. Geophys. Space Phys.*, (13):1, 1975.

[6] (Ed.) J. R. Holton, J. A. Curry, and J. A. Pyle. *Encyclopedia of Atmospheric Sciences.* Number 4, pp. 1407-1824. Academic Press, UK, 2003.

[7] F. Swartz. *Mem. Cour. Acad. R. Belg.*, (51), 1895.

[8] T. Midgley and A. L. Henne. *Ind. Eng. Chem.*, (22):542, 1930.

[9] L. E. Manzer, V. N. M. Rao, (Eds.) D. D. Eley, H. Pines, and P. B. Weisz. *Advances in Catalysis : Volume 39, pp. 329-350.* Academic Press, Inc., USA, 1993.

[10] L. E. Manzer and V. M. N. Rao. *Adv. Catal.*, (39):329, 1992.

[11] S. Brunet, B. Requieme, E. Matouba, J. Barrult, and M. Blancard. *J. Catal.*, (152):70, 1995.

[12] A. Kohne and E. Kemnitz. *J. Fluorine Chem.*, (75):103, 1995.

[13] S. L. Bell. *U.S. Pat.*, (4,129,603), 1978.

[14] L. E. Manzer. *U.S. Pat.*, (5,036,036), 1991.

[15] M. Vecchio, G. Groppelli, and J. C. Tatlow. *J. Fluorine Chem.*, (4):117, 1974.

[16] J. L. Bitner and J. R. Lacher. *U.S. Dep. Commer. Off. Tech. Serv. Rep.*, (136732), 1958.

[17] I. J. Darragh. *U.K. Pat.*, (1,578,933), 1980.

[18] S. P. Von Halasz. *Ger. Pat.*, (3,009,760), 1981.

[19] L. E. Manzer and V. N. M. Rao. *U.S. Pat.*, (4,902,838), 1990.

[20] G. J. Moore and H. M. Massey. *U.S. Pat.*, (4,950,815), 1990.

[21] S. Morikawa, S. Samejimma, M. Yoshitake, S. Tatematsu, and T. Tanuma. *Jpn. Pat. Appl.*, (2-115135), 1990.

[22] E. Kemnitz, A. Kohne, I. Grohmann, A. Lippitz, and W. E. S. Unger. *J. Catal.*, (159):270, 1996.

[23] S. Yoneda and G. Yanase. *Jpn. Pat. Appl.*, (2-129131), 1990.

[24] L. E. Manzer and V. N. M. Rao. *U.S. Pat.*, (4,766,260), 1988.

[25] W. H. Gumprecht, L. E. Manzer, and V. N. M. Rao. *U.S. Pat.*, (4,843,181), 1989.

[26] J. J. Lerou. *U.S. Pat.*, (5,051,537), 1991.

[27] D. Carmello and G. Mirano. *U.S. Pat.*, (4,967,023), 1990.

[28] R. E. Burke, D. D. Coffman, and G. H. Kalb. *U.S. Pat.*, (2,425,991), 1947.

[29] Y. Kanakami and W. Hircynki. *Fr. Pat.*, (1,570,306), 1969.

[30] A. N. Golubev, A. L. Goldino, Y. A. Panshin, and V. I. Kolomenskov. *USSR Pat.*, (341,748), 1972.

[31] M. Ozawa, F. Inoue, N. Koketsu, and K. Matsuoka. *Jpn. Pat.Appl.*, (50-106905), 1975.

[32] J. P. Henry, C. E. Rectenwald, and J. W. Clark. *Can. Pat.*, (832,503), 1970.

[33] A. L. Henne. *J. Am. Chem. Soc.*, (59):144, 1937.

[34] H. J. Freund. *Angew. Chem.*, (109):444, 1997.

[35] C. Xu, M. Hassel, H. Kuhlenbeck, and H. J. Freund. *Surf. Sci.*, (258):23, 1991.

[36] F. Rohr, M. Baeumer, H. J. Freund, J. A. Mejias, V. Staemmler, S. Mueller, L. Hammer, and K. Heinz. *Surf. Sci.*, (372):L291, 1997.

[37] E. Kemnitz and A. Hess. *J. prakt. Chem.*, (334):591, 1992.

[38] L. Kolditz, G. Kauschka, and W. Schmidt. *Z. Anorg. Allg. Chem.*, (434):41, 1977.

[39] L. Kolditz, U. Calov, G. Kauschka, and W. Schmidt. *Z. Anorg. Allg. Chem.*, (434):55, 1977.

[40] E. Kemnitz, A. Hess, G. Rother, and S. Troyanov. *J. Catal.*, (159):332, 1996.

[41] E. Kemnitz, D. Hass, and B. Grimm. *Z. Anorg. Allg. Chem.*, (589):228, 1990.

[42] D. R. Coulson, P. W. J. G. Wijnen, J. J. Lerou, and L. E. Manzer. *J. Catal.*, (140):103, 1993.

[43] E. Kemnitz, A. Kohne, and E. Lieske. *J. Fluorine Chem.*, (81):197, 1997.

[44] D. M. C. Kavanagh, T. A. Ryan, and B. Mile. *J. Fluorine Chem.*, (64):167, 1993.

[45] E. Kemnitz and K. U. Niedersen. *J. Catal.*, (155):283, 1995.

[46] E. Kemnitz and K. U. Niedersen. *J. Fluorine Chem.*, (79):111, 1996.

[47] J. Kijowski, G. Webb, and J. M. Winfield. *Appl. Catal.*, (27):181, 1986.

[48] D. Bechadergue, M. Blanchard, and P. Canesson. *Appl. Catal.*, (27):179, 1986.

[49] E. Kemnitz, J. M. Winfield, Nakajima (Eds.) T, B. Zemva, and A. Tressaud. *In Advenced Inorganic Fluorides, Ch. 12, pp. 367-401.* Elsevier, Lausanne, 2000.

[50] R. Hoppe and D. Kissel. *J. Fluorine Chem.*, (24):327, 1984.

[51] U. Bentrup. *Eur. J. Solid State Chem.*, (29):51, 1992.

[52] N. Herron, D. L. Thorn, R. L. Harlow, and F. Davidson. *J. Am. Chem. Soc.*, (115):3028, 1993.

[53] N. Herron, R. L. Harlow, and D. L. Thorn. *Inorg. Chem.*, (32):2985, 1993.

[54] N. Herron and W. E. Farneth. *Adv. Mater.*, (8):959, 1996.

[55] N. Herron, D. L. Thorn, R. L. Harlow, G. A. Jones, J. B. Parise, J. A. Fernandez-Baca, and T. Vogt. *Chem. Mater.*, (7):75, 1995.

[56] J. M. Cowle. *J. Am. Chem. Soc.*, (70):105, 1948.

[57] (Eds.) D. Babel, A. Tressaud, and P. Hagenmuller. *Inorganic Solid Fluorides, pp. 77-203.* Academic Press Inc., New York, 1985.

[58] A. Hess and E. Kemnitz. *J. Catal.*, (149):449, 1994.

[59] A. Le Bail, C. Jacoboni, M. Leblanc, R. De Pape, H. Duroy, and J. L. Fourquet. *J. Solid State Chem.*, (77):96, 1988.

[60] (Eds.) H. Sigbahn, L. Karlson, and W. Melhorn. *Handbuch der Physik.* Number 31, pp. 215. Springer Verlag, Berlin, 1982.

[61] D. Briggs and M. P. Seah. *Practical Surface Analysis.* John Wiley and Sons Ltd., Chichester, 1983.

[62] N. Martenson and A. Nilsson. *J. Electron Spectrosc. Relat. Phenom.*, (75):209, 1995.

[63] G. Moretti. *J. Electron Spectrosc. Relat. Phenom.*, (76):365, 1995.

[64] C. D. Wagner and A. Joshi. *J. Electron Spectrosc. Relat. Phenom.*, (47):283, 1988.

[65] S. W. Gaarenstroom and N. Winograd. *J. Chem. Phys.*, (67):3500, 1977.

[66] C. D. Wagner. *Farady Discuss.*, (60):291, 1975.

[67] C. D. Wagner, L. H. Gale, and R. H. Raymond. *Anal. Chem.*, (51):466, 1979.

[68] R. Hesse. *Spectrum Processing and Analysis Software for Core Level Photoelectron Spectra.* Universitaet Leipzig, Wilhelm-Ostwald-Institut, 2003.

[69] D. A. Shirley. *Phys. Rev. B*, (5):4709, 1972.

[70] M. P. Seah. *Surf. Interface Anal.*, (2):222, 1980.

[71] J. C. Carver and G. K. Schweitzer. *The J. Chem. Phys.*, (57):973, 1972.

[72] T. Droubay and S. A. Chambers. *Phys. Rev. B*, (64):205414, 2001.

[73] R. P. Gupta and S. K. Sen. *Phys. Rev. B*, (12):15, 1975.

[74] I. Grohmann, E. Kemnitz, A. Lippitz, and W. E. S. Unger. *Surf. Interface Anal.*, (23):887, 1995.

[75] S. Music, M. Maljkovic, S. Popovic, and R. Trojko. *Croatica Chemica Acta*, (72):789, 1999.

[76] L. Gmelin. *Gmelins Handbuch der Anorganischen Chemie.* Number 52/B. Chemie Verlag, Weinheim, 8 edition, 1962.

[77] P. Ascarelli and G. Moretti. *Surf. Interface Anal.*, (7):8, 1985.

[78] S. A. Chambers and T. Droubay. *Phys. Rev. B*, (64):075410, 2001.

[79] F. M. F. de Groot. *Physica B*, (208/209):15, 1995.

[80] T. A. Carlson. *Photoelectron and Auger Spectroscopy.* Plenum Press, New York, 1976.

[81] E. Unveren, E. Kemnitz, S. Hutton, A. Lippitz, and W. E. S. Unger. *Surf. Interface Anal.*, (36):92, 2004.

[82] E. Unveren, E. Kemnitz, S. Hutton, A. Lippitz, and W. E. S. Unger. *10th European Conference on Applications of Surface and Intterface Analysis*, page CAT 013, 2003.

[83] O. Boese, W. E. S. Unger, E. Kemnitz, and S. L. M. Schroeder. *Phys. Chem. Chem. Phys.*, (4):2824, 2002.

[84] E. Kemnitz and D. H. Menz. *Prog. Solid St. Chem.*, (26):97, 1998.

[85] C. D. Wagner. *NIST Standard Reference Database (NIST X-ray Photoelectron Spectroscopy Database).* Number 20. Springer Verlag, Gaithersburg, 1.0 edition, 1989.

[86] O. Boese, E. Kemnitz, A. Lippitz, and W. E. S. Unger. *Appl. Surf. Sci.*, (120):181, 1997.

[87] M. P. Seah. *Surf. Interface Anal.*, (31):721, 2001.

[88] B. W. Veal and A. P. Paulikas. *Phys. Rev. Lett.*, (51):1995, 1983.

[89] D. Balazs, D. Favez, Y. Chevolot, N. Xanthopoulos, C. Granges, P. Descouts B. O. Aronsson, F. Sidouni, and H. J. Mathieu. *European Cells and Materials*, (1):18, 2001.

[90] J. Meinhardt, D. Hirsch, and R. Mehnert. *EST 2004 presentation.* Leibniz-Institut fuer Oberflaechenmodifizierung Leipzig e. V., Germany, 2004.

[91] H. Lee, H. D. Jeong, Y. S. Chung, H. G. Lee, M. J. Chung, S. Kim, and H. S. Kim. *J. Catal.*, (169):307, 1997.

[92] L. A. Grunes. *Phys. Rev. B*, (27):2111, 1983.

[93] O. Boese, B. Adamczyk, K. Fiedler, and E. Kemnitz. *Catal. Lett.*, (54):211, 1998.

[94] B. Adamczyk, O. Boese, N. Weiher, S. L. M. Schroeder, and E. Kemnitz. *J. Fluorine Chem.*, (101):239, 2000.

[95] B. Adamczyk. *Ph.D. Thesis.* Humboldt University Berlin, Institute of Chemistry, Berlin, 2000.

[96] F. M. F. de Groot. *J. Electron Spectrosc. Relat. Phenom.*, (67):529, 1994.

[97] S. M. Davis, G. D. Meitzner, D. A. Fischer, and J. Gland. *J. Catal.*, (142):368, 1993.

[98] J. C. Vickerman. *ToF-SIMS: Surface Analysis by Mass Spectrometry.* IM Puplications and Surface Spectra Limited, Chichester, 2001.

[99] K. Poels, L. Van Vaeck, and R. Gijbels. *Anal. Chem.*, (70):504, 1998.

[100] E. Cuynen, L. Van Vaeck, and P. Van Espen. *Rapid Commun. Mass Spectrom.*, (13):2287, 1999.

[101] J. W. Niemantsverdriet. *Spectroscopy in Catalysis.* Wiley-VCH Verlag, Weinheim, 2nd edition, 2000.

[102] M. E. Omari, J. Senegas, and J-M Reau. *Solid State Ionics*, (116):229, 1999.

[103] U. Gross, S. Ruediger, A-R. Grimmer, and E. Kemnitz. *J. Fluorine Chem.*, (115):193, 2002.

[104] J. Krishna Murthy, U. Gross, S. Ruediger, E. Unveren, W. E. S. Unger, and E. Kemnitz. *prepared for puplication*, 2004.

[105] G. Cerrato N. Del Favero F. Filippi C. Morterra, G. Magnacca and C. V. Folonari. *J. Chem. Soc. Faraday Trans.*, (89):135, 1993.

[106] Powder Diffraction File. *PDF-2 Database.* Number Sets 1-45. Dataware Technologies, Inc., USA, icdd a6 edition, 1995.

[107] P. Ratnasamy and A. J. Leonard. *The J. Phys. Chem.*, (76):1838, 1972.

[108] *AXIS HSi 165 and Ultra Operators Mannual.* Number Ref:39-281. Kratos Analytical Ltd., Manchester, 2000.

[109] F. Seel. *Angew. Chem.*, (76):532, 1964.

A Appendix

After charge correction referring on C 1s BE 284.8 eV, the estimated binding energy (BE) values for the core levels and kinetic energy (KE) values for the Auger transitions and the modified Auger parameters (α') are given in this appendix for the following group of samples:

(1) reference samples,

(2) Cr_2O_3 samples activated with CCl_2F_2 dismutation reaction at 390 $°C$,

(3) Cr_2O_3 samples activated with CCl_2F_2 dismutation reaction at 390 $°C$ ("in-situ"),

(4) Cr_2O_3 samples activated with CCl_2F_2 dismutation reaction at 300 $°C$,

(5) Cr_2O_3 samples treated with HF at 390 $°C$,

(6) Cr_2O_3 samples treated with HCl at 390 $°C$.

Table 11: C 1s referred ESCA results for reference samples

time (min)	O 1s	F 1s	F KLL	$\alpha'(F1s)$	Cr 2p	Cr LMM	$\alpha'(Cr2p)$	Cr 3s	$\alpha'(Cr3s)$	Cl $2p_{3/2}$	Cl LMM	$\alpha'(Cl2p)$
Cr_2O_3	529.85				576.15	529.15	1105.25	74.75	603.85		529.15	
Cr_2O_3 dried	530.35				576.40	528.85	1105.25	75.05	603.85		528.85	
$Cr(OH)_3$	531.05				576.85	527.85	1104.65	75.25	603.05		527.85	
$CrCl_3$	532.50				577.15	528.55	1105.75	76.45	605.05	199.15	528.55	381.55
CrF_2OH	531.75	684.85	656.25	1341.05	578.65	526.35	1105.05	76.75	603.15		526.35	
$CrF_3.H_2O$	532.95	685.45	655.65	1341.05	579.45	525.65	1105.15	77.35	603.05		525.65	
$\beta - CrF_3$	532.25	685.35	655.55	1340.95	579.45	525.95	1105.35	77.50	603.45		525.95	
$\alpha - CrF_3$	532.25	685.55	655.45	1340.95	579.70	526.25	1105.95	77.65	603.95		526.25	

Table 12: C 1s referred ESCA results for Cr_2O_3 catalysts activated with CCl_2F_2 dismutation reaction at 390 °C

time (min)	O 1s	F 1s	F KLL	$\alpha'(F1s)$	Cr 2p	Cr LMM	$\alpha'(Cr2p)$	Cr 3s	$\alpha'(Cr3s)$	Cl $2p_{3/2}$	Cl LMM	$\alpha'(Cl2p)$
1	530.45	684.15	658.25	1342.45	576.75	528.55	1105.35	75.35	603.95	198.55	183.85	382.45
2	530.75	684.80	657.60	1342.40	577.25	528.35	1105.55	75.45	603.75	198.80	183.25	382.05
3	530.95	685.15	657.15	1342.25	577.25	528.05	1105.30	75.70	603.75	199.05	183.15	382.25
4	530.85	684.95	657.25	1342.25	577.05	528.15	1105.25	75.55	603.75	198.95	182.95	381.95
5	530.95	685.15	657.15	1342.25	577.15	528.05	1105.15	75.65	603.65	198.95	182.95	381.95
10	530.75	685.05	657.45	1342.45	577.25	528.15	1105.45	75.55	603.65	198.85	182.95	381.75
15	530.95	685.15	657.15	1342.35	577.45	527.95	1105.45	75.75	603.75	199.05	183.45	382.45
30	530.85	685.05	657.35	1342.35	577.05	528.05	1105.15	75.65	603.75	198.85	183.05	381.85
120	530.85	685.15	657.25	1342.45	577.35	528.00	1105.35	75.65	603.65	198.95	183.55	382.45
180	530.95	685.25	657.15	1342.35	577.25	527.95	1105.15	75.70	603.65	199.05	182.75	381.85
540	530.95	685.15	657.15	1342.35	577.55	527.95	1105.55	75.75	603.70	199.05	182.95	382.05
900	530.95	685.25	657.05	1342.35	577.55	527.95	1105.55	75.75	603.75	199.05	182.75	381.85
1440	530.85	685.05	657.15	1342.25	577.45	528.05	1105.55	75.55	603.65	199.05	183.00	382.05

Table 13: C 1s referred “in-situ” ESCA results for Cr_2O_3 catalysts activated with CCl_2F_2 dismutation reaction at 390 °C

time (min)	O 1s	F 1s	F KLL	$\alpha'(F1s)$	Cr 2p	Cr LMM	$\alpha'(Cr2p)$	Cr 3s	$\alpha'(Cr3s)$	Cl 2p$_{3/2}$	Cl LMM	$\alpha'(Cl2p)$
Cr_2O_3	530.05				576.35	528.65	1105.05	74.95	603.65		528.65	
Cr_2O_3 dried	530.25				576.55	528.65	1105.15	75.05	603.65		528.65	
1	530.45	683.95	657.95	1341.95	576.85	528.55	1105.35	75.25	603.75	198.65	528.55	381.85
3	530.65	684.95	657.25	1342.15	577.05	528.05	1105.15	75.55	603.65	198.75	528.05	381.25
5	530.75	684.95	657.15	1342.05	577.15	528.15	1105.35	75.45	603.55	198.85	528.15	381.45
9	530.85	685.15	657.15	1342.25	577.25	527.75	1105.05	75.85	603.65	198.95	527.75	381.45

Table 14: C 1s referred ESCA results for Cr_2O_3 catalysts activated with CCl_2F_2 dismutation reaction at 300 °C

time (min)	O 1s	F 1s	F KLL	$\alpha'(F1s)$	Cr 2p	Cr LMM	$\alpha'(Cr2p)$	Cr 3s	$\alpha'(Cr3s)$	Cl 2p$_{3/2}$	Cl LMM	$\alpha'(Cl2p)$
15	530.40	684.50	658.10	1342.60	576.75	528.55	1105.35	75.35	603.85	197.95	184.60	382.55
25	530.65	684.85	657.75	1342.65	576.90	528.35	1105.25	75.45	603.85	198.45	184.15	382.55
30	530.75	684.80	657.30	1342.10	577.25	528.15	1105.45	75.60	603.75	198.75	183.55	382.25
45	530.85	684.95	657.35	1342.25	577.15	528.25	1105.45	75.65	603.95	198.85	182.95	381.85
120	530.85	685.05	657.25	1342.25	577.05	527.95	1105.05	75.55	603.55	198.85	183.15	382.00

Table 15: C 1s referred ESCA results for Cr_2O_3 samples treated with HF at 390 $°C$

time (min)	O 1s	F 1s	F KLL	$\alpha'(F1s)$	Cr 2p	Cr LMM	$\alpha'(Cr2p)$	Cr 3s	$\alpha'(Cr3s)$
15	530.65	684.95	656.95	1341.95	576.95	528.05	1104.95	75.55	603.55
60	530.75	684.95	656.90	1341.85	577.05	527.95	1104.95	75.55	603.45
180	530.65	684.95	656.95	1341.85	577.05	527.95	1104.95	75.55	603.45
540	530.75	685.00	656.85	1341.85	577.35	527.85	1105.25	75.55	603.45

Table 16: C 1s referred ESCA results for Cr_2O_3 samples treated with HCl at 390 $°C$

time (min)	O 1s	Cr 2p	Cr LMM	$\alpha'(Cr2p)$	Cr 3s	$\alpha'(Cr3s)$	Cl $2p_{3/2}$	Cl LMM	$\alpha'(Cl2p)$
15	530.65	576.95	528.15	1105.15	75.45	603.65	198.75	182.95	381.70
60	530.60	577.15	528.15	1105.25	75.35	603.45	198.75	182.95	381.65
180	530.55	576.95	528.15	1105.15	75.35	603.50	198.75	183.25	381.95
540	530.75	577.25	528.05	1105.30	75.35	603.35	198.85	182.85	381.75

B Appendix

The peak areas in the chromatogram produced by the GC are used for the quantification of the dismutation products. For the normalization the peak area in the chromatogram which is obtained by passing CCl_2F_2 from the empty reactor is used. The results are tabulated in this appendix with the estimated standard errors for both dismutation reactions performed at 390 and 300 $^\circ C$.

Estimation of Standard Error .
The average value $(\overline{X})$ of measurements are determined by the following formula:

$$\overline{X} = \frac{1}{n}\sum_{i=1}^{n} X_i \tag{23}$$

where X_i is the value of measurements and n is the number of measurements.
The standard deviation (σ) is calculated by the following equation:

$$\sigma = \frac{1}{n-1}\sum_{i=1}^{n}(X_i - \overline{X})^2 \tag{24}$$

The standard error (SE) is estimated by the following equation:

$$SE = \frac{\sigma}{\sqrt{n}} \tag{25}$$

Table 17: Normalized concentrations (%) of the dismutation products for the Cr_2O_3 catalyzed reaction with CCl_2F_2 at 390 °C

time (min)	$CClF_3$	SE ±	CCl_2F_2	SE ±	CCl_3F	SE ±	CCl_4	SE ±
0	0.0	0.0	100.0	8.4	0.0	0.0	0.0	0.0
1	0.3	0.0	97.0	8.1	0.0	0.0	0.0	0.0
2	36.0	1.3	20.0	1.7	0.0	0.0	0.0	0.0
3	46.6	1.7	11.3	1.0	0.0	0.0	0.0	0.0
4	44.3	1.6	14.1	1.2	2.5	0.3	4.7	0.6
5	51.8	1.8	18.0	1.5	7.9	1.0	19.7	2.6
10	55.7	2.0	17.1	1.4	8.1	1.0	19.6	2.6
15	51.4	1.8	18.8	1.6	8.4	1.0	19.7	2.6
30	51.1	1.8	17.7	1.5	7.1	0.9	18.3	2.4
60	50.7	1.8	16.7	1.4	6.8	0.8	17.7	2.4
90	49.8	1.8	15.8	1.3	6.8	0.8	17.0	2.3
120	50.1	1.8	15.7	1.3	6.8	0.8	17.5	2.3
150	50.0	1.8	16.0	1.3	6.9	0.9	17.6	2.3
180	49.8	1.8	15.7	1.3	6.8	0.8	17.5	2.3
540	50.3	1.8	16.4	1.4	6.5	0.8	17.6	2.3
870	53.2	1.9	17.0	1.4	6.8	0.8	18.7	2.5
900	52.6	1.9	16.6	1.4	6.6	0.8	18.5	2.5
1350	54.0	1.9	16.0	1.3	7.5	0.9	18.9	2.5
1380	53.5	1.9	15.5	1.3	7.1	0.9	18.8	2.5
1410	53.7	1.9	15.8	1.3	7.2	0.9	19.1	2.5
1440	53.2	1.9	15.4	1.3	7.1	0.9	18.6	2.5

Table 18: Normalized concentrations (%) of the dismutation products for the Cr_2O_3 catalyzed reaction with CCl_2F_2 at 300 °C

time (min)	$CClF_3$	SE ±	CCl_2F_2	SE ±	CCl_3F	SE ±	CCl_4	SE ±
0	0.0	0.0	100.0	8.4	0.0	0.0	0.0	0.0
5	0.0	0.0	100.0	8.4	0.0	0.0	0.0	0.0
10	0.0	0.0	100.0	8.4	0.0	0.0	0.0	0.0
15	0.0	0.0	100.0	8.4	0.0	0.0	0.0	0.0
20	0.0	0.0	100.0	8.4	0.0	0.0	0.0	0.0
25	7.1	0.3	92.8	7.8	0.1	0.0	0.0	0.0
30	34.0	1.2	64.0	5.4	1.5	0.2	0.5	0.1
35	34.8	1.2	47.8	4.0	6.8	0.8	10.6	1.4
45	39.4	1.4	39.4	3.3	7.2	0.9	14.0	1.9
60	39.4	1.4	40.1	3.4	7.1	0.9	13.5	1.8
90	39.9	1.4	38.8	3.3	7.1	0.9	14.2	1.9
120	40.7	1.4	37.2	3.1	7.2	0.9	14.9	2.0

Acknowledgments

I would like to thank Prof. Dr. E. Kemnitz sincerely (Humboldt University Berlin, Institute of Inorganic Chemistry) for admitting me into his group and giving me the opportunity to work in this interesting subject and for his supervision and valuable discussions.

I would like to give my special thanks to Dr. W.E.S. Unger (Federal Institute of Material Research and Testing (BAM), Laboratory VIII.23) for providing me the chance to work also in his group, for his supervision and valuable discussions and encouragements.

I would like to thank individually all the members of the group of Prof. Dr. E. Kemnitz in Humboldt University Berlin, Institute of Inorganic Chemistry, for the technical and scientific discussions. Especially I thank Ms. E. Lieske for her technical supervision and encouragements, Ms. Bässler for the fluorine and FTIR-photoacoustic analysis and Dr. Gross for the NMR analysis.

In the same way I would like to express my gladness to everyone in the group of Dr. W.E.S. Unger in Federal Institute of Material Research and Testing (BAM), Laboratory VIII.23, for the kindly working atmosphere. Especially I would like to thank Mr. A. Lippitz for his technical supervision on ESCALAB 200X spectrometer and endless support and Ms. Benemann for the SEM analysis and her kindly encouragements. Many thanks to Mr. U. Oran for his valuable cooperation in ToF-SIMS analysis.

I would like to thank to Dr. Riesemeier (Federal Institute of Material Research and Testing (BAM), Laboratory I.4) for giving the opportunity to perform the XANES analysis in BAMline at BESSY and Dr. S.L.M. Schroeder (University of Manchester Institute of Science and Technology -UMIST, Molecular Materials Centre) for providing beam time at the station 5U.1 in Daresbury. In addition, I thank the gentlemen and Dr. L. Wilde (Institute for Applied Chemistry Berlin-Adlershof) for their valuable discussions and cooperation in XANES analysis.

I kindly acknowledge the financial support of Deutsche Forschungsgemeinschaft (KE489/16).

Finally, I would like to thank my wife for her generous support during this work.

Curriculum Vitae

PERSONAL DATA

Date of birth : October, 24 1973
Place of birth : Saarbrücken, Germany
Marital status : Married

EDUCATION

06 / 2001 - present	Humboldt University - Berlin Ph.D. in Chemistry, Inorganic Chemistry
02 / 1999 - 06 / 2001	Ege University - Izmir MSc in Chemical Engineering, Process and Reactor Design
09 / 1993 - 06 / 1998	Middle East Technical University - Ankara BSc in Chemical Engineering
06 / 1992 - 09 / 1993	Middle East Technical University - Ankara Department of Basic English
April, June 1992	Student Selection and Admission Centre (ÖSYM) - Izmir
06 - 10 / 1991	Air Force Academy - Istanbul Learned to use T-41D training plane
09 / 1985 - 06 / 1991	Suphi Koyuncuoglu High School - Izmir Mathematics and Natural Science Division

---

WORK EXPERIENCE

06 / 2001 - present	Scientific Co-worker Federal Institute for Materials Research and Testing (BAM) - Berlin Laboratory VIII.23 “Surface and Thin Film Analysis”

07 / 1999 - 06 / 2001	Process Research & Development Engineer Form Plastik Sanayi ve Ticaret Ltd. - Izmir Plastic injection moulding factory
02 / 1998 - 07 / 1999	Production Engineer Cetiner Seramik Sanayi Ic & Dis Ticaret Ltd. - Izmir Ceramic factory
Summer 1997	Summer training HENKEL - Izmir Department of oil and margarine production
Summers 1992 - 1996	Sales Representative Sector of tourism

CERTIFICATES AND SEMINARS

October 5-10, 2003	ECASIA‘03 - Berlin 10th European Conference on Applications of Surface and Interface
January 24, 2003	SOFA‘03 - Berlin Seminar Oberflächenanalytik (Surface Analysis)
November 8, 2001	SGE GmbH - Berlin Optimization of the GC and GC/MS techniques
July 14, 2000	Izmir Chamber of Mechanical Engineers Quality Cost Seminar
December 1-2, 1999	Izmir Chamber of Chemical Engineers Statistical Process Control Training
November 10-12, 1999	The Turkish Standards Institution - Izmir K - Q / TSE - ISO - EN / 9000 Intra - Organization Quality Investigator Program